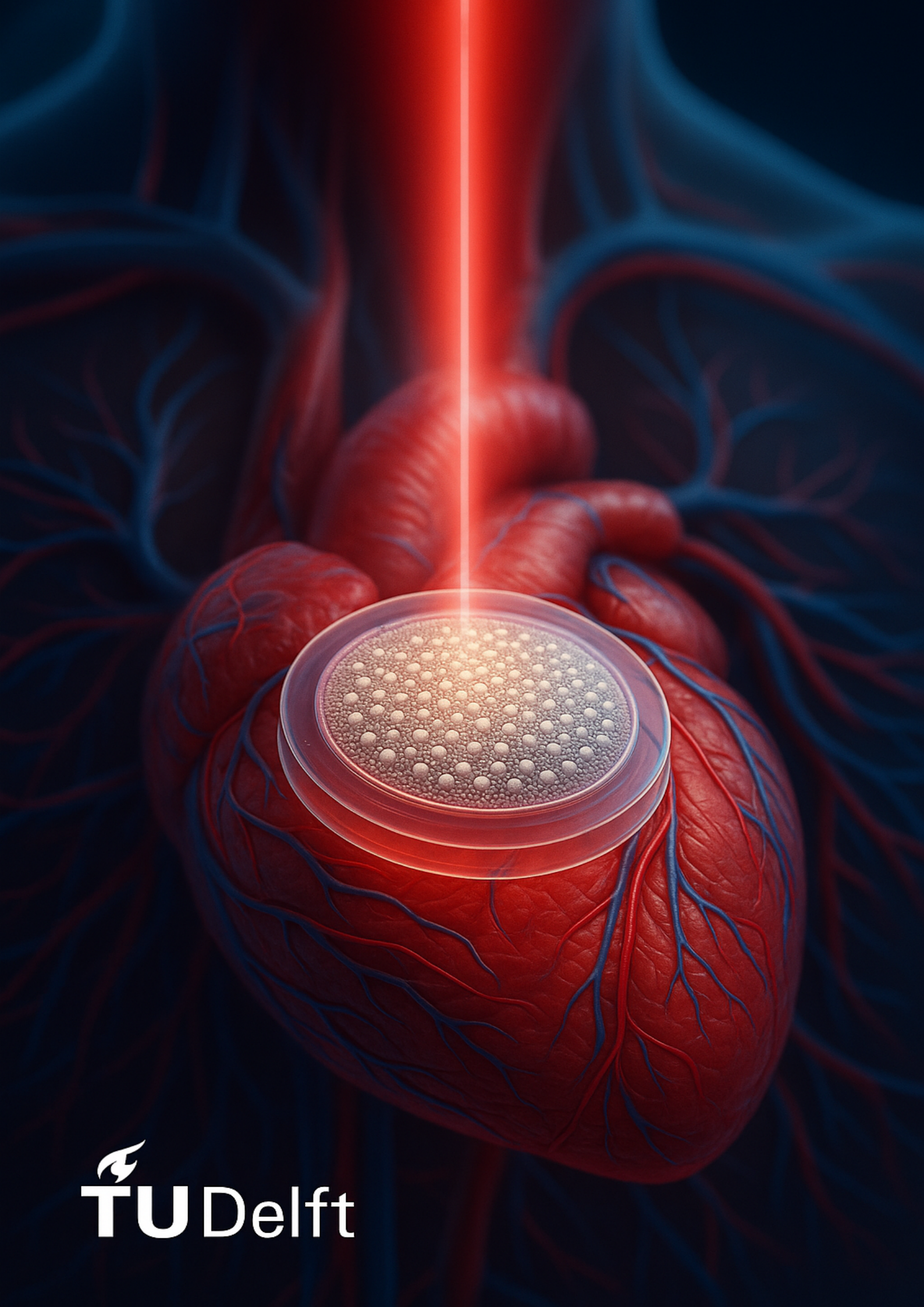
TU Delft

Design and Optimization of Implantable Light Emitter Through Upconverting Materials for Cardiac Muscle Concentration Monitoring

by

Haoxiang Jiang

To obtain the degree of Master of Engineering
at the Delft University of Technology,
To be defended publicly on Tuesday August, 26.

Thesis committee:	Dr. Arroyo Cardoso,	TU Delft, Thesis advisor
	Dr. Clementine Boutry,	TU Delft, Thesis advisor
	Dr.ir. M.H.F. Sluiter,	TU Delft, Thesis co-supervisor
	Dr. Matthias Alfeld,	TU Delft, External member
	MSc. Z. Liao,	TU Delft, Daily advisor

Cover: Generated by ChatGPT 4.0

Preface

This thesis presents the outcomes of my master's project, titled Design and Optimization of an Implantable Light Emitter Through Upconverting Materials for Cardiac Muscle Oxygenation Monitoring, which I began in November 2024.

At the beginning of the project, I was introduced to the background and objectives through the guidance of Zhengwei Liao. Coming from a materials science and engineering background, I was stepping into a completely new domain. I was genuinely excited to explore the field of implantable biomedical devices and micro/nanofabrication—an area that allowed me to apply my materials knowledge in a highly interdisciplinary and meaningful way. Throughout the project, I faced numerous technical challenges, many of which I overcame by drawing on core materials science principles. This process was both demanding and deeply rewarding, as it pushed me beyond my comfort zone and broadened my academic and technical horizons.

One of the most fulfilling aspects of the project was building an optical measurement platform from scratch. From theoretical design and component selection to assembly, testing, and troubleshooting, I had to learn and apply optical engineering skills entirely new to me. Despite the challenges, successfully capturing measurable data in the final stage was a moment of great satisfaction that made all the effort worthwhile. The entire journey—from understanding physiological needs, to sensor design, to experimental validation—was intellectually stimulating and personally enriching.

I would like to express my deepest gratitude to my supervisors. I sincerely thank Dr. Filipe Arroyo Cardoso and Dr. Clémentine Boutry for their continuous support and mentorship throughout this journey. Their guidance helped me navigate unfamiliar territory and develop new competencies with confidence. I am also grateful to Dr.ir. M.H.F. Sluiter for his insightful feedback during progress meetings and for consistently reminding me to approach problems from a materials perspective—advice that proved critical in solving many of the challenges I faced. I especially thank Zhengwei Liao, my daily supervisor, whose hands-on guidance and practical support were indispensable to my progress. Finally, I would like to thank the members of the ECTM group, EI group, and MSE department. Your support and encouragement over the past ten months—from the early stages of the project to its successful completion—have been invaluable. I am truly grateful for everything you've done to help me along the way.

Haoxiang Jiang
01/08/2025

Abstract

Heart failure remains a leading cause of morbidity and mortality worldwide, and patient health is closely tied to the functional status of cardiac tissue. Among various physiological indicators, myocardial oxygenation serves as one of the most direct and reliable metrics for assessing cardiac function. However, current clinical tools lack compact, power-free solutions that can directly and continuously monitor myocardial oxygen levels in an implantable format. Addressing this unmet need, this project presents the development of an implantable optical sensor designed for real-time cardiac oxygenation monitoring. The proposed system exploits the intrinsic luminescent properties of NADH, whose ultraviolet (UV)-excited fluorescence serves as an indicator of tissue oxygenation. Given the limited penetration depth of UV light in biological tissues, the design relies on externally delivered near-infrared (NIR) light, which can penetrate deep into tissue and reach the implanted device. Lanthanide-based upconverting nanoparticles (UCNPs) are employed to convert 808nm NIR photons into UV photons, thereby enabling localized NADH excitation without the need for implanted power sources. However, UCNPs simultaneously emit both UV and blue light, and the blue emission spectrally overlaps with that of NADH, potentially compromising measurement accuracy. To mitigate this interference, a Fabry–Perot optical filter was integrated into the system to selectively block the blue component while maintaining high transmittance in the UV range. COMSOL simulations were used to optimize the filter's multilayer thicknesses, and the influence of precursor gas ratios on film quality and optical performance was systematically investigated. The optimized UCNPs were then drop-cast onto the filter surface to maximize photon conversion, and material characterization confirmed dense nanoparticle coverage. Optical tests using a spectrometer and photodetector revealed distinct upconversion luminescence under 808nm excitation. The filter demonstrated a transmittance of 96.67% at 360nm and a blue-light suppression ratio of 77.46%, effectively addressing spectral interference. Collectively, these results validate the feasibility of this compact, externally powered light emitter for real-time, implantable cardiac oxygen monitoring. While current limitations include relatively low upconversion efficiency and lack of biodegradability, the platform provides a promising foundation for future development of self-contained, minimally invasive biosensors.

Contents

Chapter 1

Introduction

The heart is one of the most vital organs in the human body, responsible for distributing oxygen and nutrients to sustain life. As individuals age, the risk of developing heart failure (HF) increases. Heart failure is a progressive and irreversible condition that gradually compromises the heart's ability to pump sufficient blood. This decline in cardiac function can lead to symptoms such as fatigue and shortness of breath, which significantly impair patients' quality of life. Currently, more than 20 million people worldwide are affected by heart failure [1].
Although HF is typically considered incurable, recent clinical studies have shown that a subset of patients with advanced disease can achieve sustained functional recovery. Through carefully managed mechanical unloading and pharmacological therapy, some patients have undergone successful explantation of left ventricular assist devices (LVADs) while maintaining stable cardiac function without further mechanical support [2][3]. However, due to limitations such as donor shortages, procedural complexity, and high medical costs, these treatment options are not widely accessible. This situation underscores the importance of developing systems capable of real-time, continuous monitoring of cardiac function, which would enable timely clinical interventions and improved disease management.
Heart functionality is typically evaluated using several parameters, including contractile performance, heart rate, and tissue oxygenation [1]. Among the key physiological parameters, oxygen concentration within cardiac muscle is particularly critical, as it directly reflects the metabolic activity and viability of myocardial tissue. The heart contracts continuously and forcefully, and as a result, cardiomyocytes have extremely high metabolic demands and require a stable and sufficient oxygen supply to sustain their function [4]. To support this high level of energy consumption, cardiac myocytes are densely packed with mitochondria and produce large quantities of myoglobin and adenosine triphosphate (ATP), enabling efficient intracellular oxygen storage and energy generation [5]. These adaptations ensure that cardiomyocytes can meet the substantial energy requirements of continuous contraction. However, most conventional oxygen monitoring techniques focus on measuring blood or extracellular oxygen levels, which do not necessarily correlate with intracellular oxygen availability—a parameter that is more directly linked to cellular metabolism and cardiac performance [6].

Based on the challenges associated with directly measuring myocardial oxygen concentration, we propose a novel implantable sensor designed for real-time monitoring of tissue oxygenation. This design leverages the presence of a key cardiac enzyme, nicotinamide adenine dinucleotide (NADH), which reacts with oxygen to generate ATP, thereby sustaining cardiac vitality. By detecting NADH concentration, we can effectively infer the local oxygen level. Importantly, NADH exhibits luminescence properties—it absorbs ultraviolet (UV) light at 340nm and emits blue light at 475nm.
Instead of relying on traditional electroluminescent components, the system delivers UV light via an externally powered emitter. The emitted light excites NADH molecules, and the resulting fluores-

cence is collected by a detector to determine NADH concentration. Because UV light suffers from poor tissue penetration, it is unsuitable for external delivery. To overcome this, the design integrates a photonic upconversion strategy: lanthanide-based nanoparticles absorb multiple near-infrared (NIR) photons—which penetrate biological tissue more effectively—and emit UV light locally. These upconversion nanoparticles (UCNPs) act as embedded light converters within the body. However, since both NADH and UCNPs emit blue light, signal interference caused by spectral overlap becomes a key challenge. To resolve this issue, a Fabry–Perot optical filter was introduced on the UCNPs surface, effectively suppressing blue emissions from the UCNPs while allowing UV light to pass through. This design ensures better spectral separation and improves detection accuracy.

Following the fabrication of the light emitter, an optical testing platform was constructed to evaluate the upconversion efficiency under both xenon lamp and laser excitation, thereby validating the feasibility of the proposed sensor system. In summary, this work introduces a fully engineered implantable light-emitting system for NADH-based oxygen sensing in deep cardiac tissue, paving the way for advanced metabolic monitoring of heart function.

Chapter 2

State of the art

2.1 Clinical Background and Detection Principle

With advancements in medical technology, effective diagnostic and therapeutic strategies have been established for a wide range of common diseases. Modern hospitals are now equipped with sophisticated instruments capable of continuously monitoring diverse physiological parameters to assess patient health. Patients also have access to regular check-ups that facilitate comprehensive evaluation of their condition. However, challenges arise due to rapid population growth, an increasing proportion of elderly individuals in many countries, and the unequal distribution of medical resources across different regions. In some healthcare systems, hospitals are struggling to allocate diagnostic resources efficiently to meet the growing demand.
Although traditional medical equipment provides accurate assessments, its bulky form factor and time-intensive operation often lead to diagnostic delays, which can critically affect patient outcomes. To overcome these limitations, the development of portable and wearable diagnostic devices has emerged as a highly promising solution. These technologies are designed to miniaturize and simplify conventional diagnostic tools, enabling continuous, real-time monitoring of physiological signals in daily life. Such devices can operate without interfering with a patient's normal activities, while also reducing the burden on centralized healthcare facilities. Moreover, real-time data acquisition allows for earlier detection of physiological anomalies, potentially facilitating timely clinical intervention before the onset of severe symptoms.

2.1.1 Heart Failure

In recent years, the prevalence of heart failure (HF) has steadily increased. According to data from the National Health and Nutrition Examination Survey (NHANES), between 2017 and 2020, approximately 6.7 million U.S. adults aged 20 and older were diagnosed with HF, with the prevalence rising from 1.9% to 2.6% during that period [7]. HF predominantly affects the elderly, as age-related structural changes—such as valvular calcification and myocardial fibrosis—along with chronic conditions like hypertension and coronary artery disease, progressively impair cardiac function [8]. However, emerging statistics suggest a decreasing age of onset, largely due to lifestyle-related risk factors such as smoking, obesity, and the consumption of diets high in saturated fat and cholesterol, which substantially increase the risk of HF [9]. These factors are closely associated with chronic heart failure (CHF), a condition that is typically irreversible and managed through a combination of pharmacological therapy and surgical intervention aimed at maintaining stable cardiac function. Patients with CHF require continuous long-term monitoring to detect early signs of decompensation and prevent clinical

deterioration. Currently, cardiac assessment relies primarily on intermittent hospital-based evaluations or inpatient monitoring, which imposes a considerable burden on both healthcare infrastructure and patients' daily routines. This situation highlights the urgent need for implantable sensors capable of providing real-time cardiac monitoring. Such systems could deliver continuous feedback on heart function, enable earlier clinical intervention, and reduce reliance on resource-intensive hospital care.

In addition to CHF, acute heart failure (AHF) represents another critical clinical condition requiring intensive monitoring. AHF can be triggered by events such as severe arrhythmias or viral myocarditis. Unlike CHF, AHF has the potential for complete recovery if timely and appropriate medical or surgical treatment is administered. In these cases, real-time physiological monitoring is particularly important, as it allows clinicians to track the patient's recovery trajectory and evaluate treatment efficacy with high temporal resolution. [10]

2.1.2 NADH

Nicotinamide adenine dinucleotide (NAD^+/NADH) is a ubiquitous metabolic coenzyme that plays a central role in cellular energy metabolism and redox balance. These coenzymes are widely distributed throughout the body and are essential for maintaining bioenergetics processes. As shown in Figure2.1, cellular ATP demand is inversely related to the concentration of NAD^+, reflecting the tight coupling between energy production and redox state. In cardiac muscle, NAD^+ is primarily localized in mitochondria, where the majority of redox reactions occur. Within the mitochondrial matrix, NADH donates electrons to the electron transport chain. As electrons are transferred through the chain to molecular oxygen, protons (H^+) are actively pumped from the matrix into the intermembrane space. This process generates both a proton concentration gradient and an electrical potential across the inner mitochondrial membrane. The resulting electrochemical gradient stores potential energy, which is harnessed as protons flow back into the matrix through ATP syntheses. This proton-driven flux powers the phosphorylation of ADP to ATP, thereby completing the energy conversion process.

The overall reaction is summarized in Equation2.1, in which NADH is oxidized and molecular oxygen is reduced to form water:

$$4\text{NADH} + \text{O}_2 + 4\text{H}^+ \rightarrow 4\text{NAD}^+ + 2\text{H}_2\text{O} \tag{2.1}$$

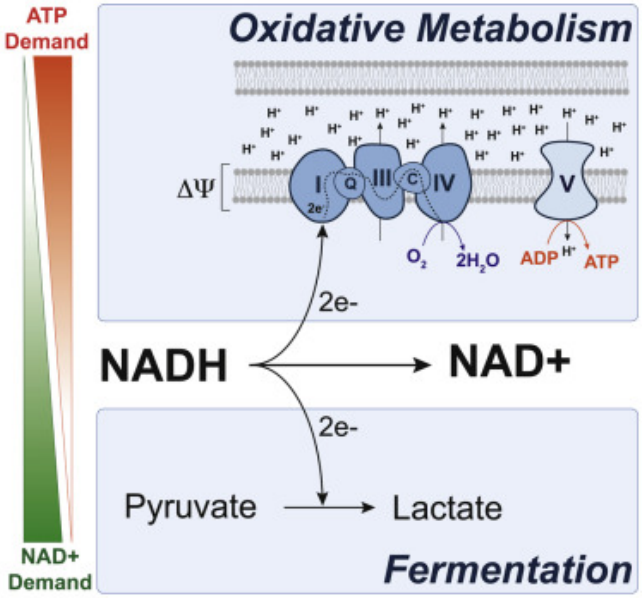

Figure 2.1: Metabolic reaction of NADH/NAD$^+$.
[11]

This reaction links oxygen consumption directly to NADH oxidation, indicating that NADH concentration can serve as an indicator of the oxygenation status within cardiac tissue. Under anaerobic conditions, NADH also participates in the reduction of pyruvate to lactate. However, unlike oxidative phosphorylation, this metabolic pathway yields only a limited amount of ATP, which is insufficient to support the high energy demands of cardiac muscle. Typically, this anaerobic mechanism is activated only under severe hypoxic conditions, such as those occurring during myocardial infarction. If hypoxia persists and anaerobic metabolism dominates for an extended duration, the resulting energy deficit can lead to progressive cardiac dysfunction and may ultimately result in heart failure [11].

Lee et al. demonstrated that heart failure is closely associated with an elevated NADH/NAD$^+$ ratio, which reflects mitochondrial dysfunction and redox imbalance. A reduced cardiac pumping rate compromises mitochondrial function and restricts oxidative metabolic pathways, ultimately leading to an increased NADH/NAD$^+$ ratio. As heart failure progresses, the translocation of cytosolic NADH into mitochondria becomes impaired, resulting in a pronounced redox imbalance in the cytolysis. In their study, the authors employed a mouse model with mitochondrial dysfunction in cardiac tissue to mimic the pathophysiological features of human heart failure. By administering nicotinamide mononucleotide (NMN), a biosynthetic precursor of NAD$^+$, they successfully restored redox equilibrium between the cytosol and mitochondria. These findings suggest that NADH concentration may serve as a sensitive indicator of cardiac metabolic activity and mitochondrial health [12].

2.1.3 Photoluminescence Based Sensing

Luminescence refers to the emission of visible or near-visible electromagnetic radiation upon excitation by various forms of energy, and it is typically classified based on the nature of the excitation source [13]. In the case of NADH molecules, their luminescent behavior corresponds specifically to fluorescence, which is a subset of luminescence. When NADH absorbs a high-energy photon, it undergoes an electronic transition to an excited state and then rapidly relaxes back to the ground state, emitting a lower-energy photon in the process. This fluorescence event occurs within a timescale

of a few nanoseconds. Since the concentration of NADH reflects the oxygenation level in cardiac tissue, its intrinsic fluorescence provides a feasible and non-invasive approach for optical detection [14]. Figure2.2 presents the absorption and emission spectra of NADH, revealing clear distinctions between the two curves. The absorption spectrum exhibits two prominent bands centered at 260nm and 340nm, respectively, indicating that NADH efficiently absorbs photons at 340nm. Upon photon absorption, NADH is excited to a higher electronic state and then immediately returns to the ground state, emitting fluorescence centered at approximately 469nm, which lies within the blue region of the visible spectrum. Based on these luminescence characteristics, the present project aims to design and fabricate an implantable sensor system for cardiac oxygenation monitoring. This system comprises two essential components. The first is a light emitter that generates 340nm excitation light to stimulate NADH fluorescence. The second is a light detector that captures the resulting 469nm emission from NADH. Because oxygen levels regulate the redox state of NADH, which in turn influences its fluorescence intensity, this optical system enables real-time monitoring of cardiac tissue oxygenation.

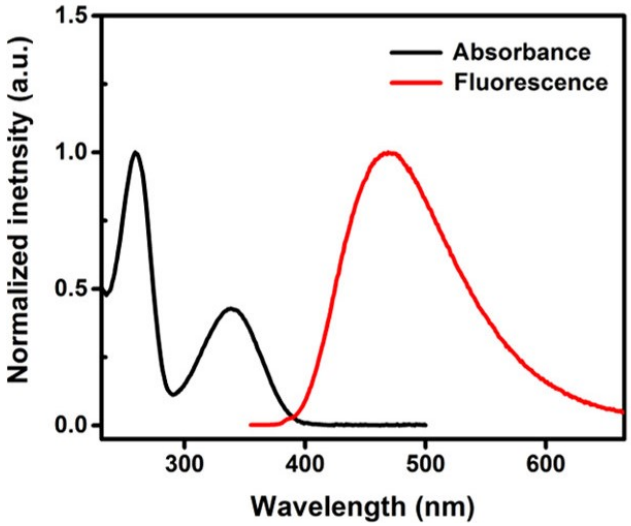

Figure 2.2: Steady-state absorption and fluorescence spectra of NADH [14]

Photoluminescence is a phenomenon commonly observed in a wide range of materials, including rare-earth elements and organic dyes. When these materials absorb photons at specific wavelengths, the photon energy excites electrons from their ground state to a higher-energy excited state. Since electrons cannot remain in the excited state for an extended period, they spontaneously return to the lower-energy ground state, releasing the excess energy in the form of emitted photons.

2.2 Optical Constraints in Biological Tissues

2.2.1 Light Penetration

When light propagates through biological tissues to reach the cardiac muscle, it undergoes a complex transmission process due to the multilayered and heterogeneous nature of the human body. As illustrated in Figure2.3, photons emitted from the light source must traverse multiple anatomical layers, including the skin, muscle, bone, and lung tissues [15].

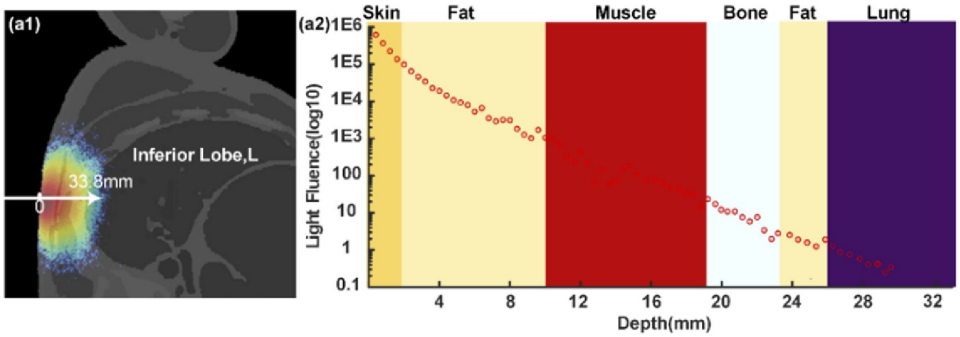

Figure 2.3: Changes of light influence intensity as tissue depth.
[15]

During transmission, several attenuation mechanisms contribute to photon loss: Firstly, different tissue types possess distinct optical absorption properties, which lead to a reduction in the intensity of incident light due to wavelength-dependent absorption.
Secondly, as photons travel through biological media, they undergo scattering, resulting in random angular deviations that diminish the effective photon flux reaching deeper tissue layers. As shown in Figure2.4, when the initial light intensity is I_0, the transmitted intensity after multiple scattering events can be described using a tissue-specific scattering coefficient.

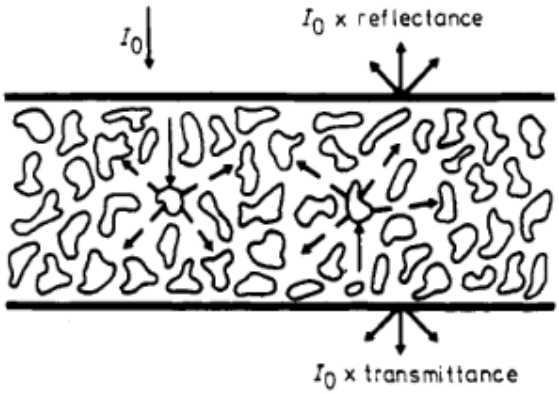

Figure 2.4: Model of diffuse reflection and transmission of light.
[16]

Moreover, not all scattered photons are irreversibly lost. A portion of them can still be collected within a defined angular acceptance by the detector or optical system. Assuming the incident beam propagates linearly through the tissue, scattering induces angular divergence, and the resulting spatial light distribution depends on the coherence and geometry of the light source. To investigate these transmission characteristics, two types of light sources were employed, as shown in Figure2.5. The first setup utilized a xenon lamp, which emits broadband and spatially diffuse light. In this case, scattering is approximately isotropic, meaning the scattered light intensity is nearly uniform in all directions. The second setup employed a laser diode, which produces a highly collimated and coherent beam. Under these conditions, scattering is anisotropic, leading to a directional angular distribution. The scattered intensity is greatest when the scattering angle is small, that is, when the scattered light is nearly aligned with the incident direction. To accurately model photon propagation in the laser-based setup, an anisotropy factor should be introduced to account for the forward-scattering nature of biological tissues.

Based on the analysis of the light–tissue interaction process, Equations 2.2 to 2.5 quantitatively describe photon propagation and attenuation in biological tissues. Equation2.2 represents the Beer–Lambert Law (BLL), which models the attenuation of a radiation beam's intensity as it travels through a medium by considering only tissue absorption [17]. Equation2.3 introduces the Modified Beer–Lambert Law (MBL) [18], which extends the original formulation to account for both absorption and scattering phenomena. This extended model incorporates the anisotropy factor g, a dimensionless parameter that characterizes the angular preference of light scattering. The value of g ranges from 1 to 1. When $g = 0$, scattering is isotropic, indicating that photons are scattered uniformly in all directions. When $g = 1$ or $g = -1$, scattering is entirely in the forward or backward direction, respectively, corresponding to the limiting case in which collimated light propagates through a transparent medium without angular dispersion. The anisotropy factor enables a more accurate estimation of the angular distribution of scattered light intensity, thereby enhancing the simulation of photon delivery to deep tissue layers such as the myocardium. The scattering coefficient μ_s, when combined with the mean cosine of the scattering angle $\langle \cos\theta \rangle$, yields the reduced scattering coefficient μ'_s. This parameter is used in Equation2.4 to calculate the tissue transmission coefficient, allowing for quantitative evaluation of photon penetration efficiency across different wavelengths [19].

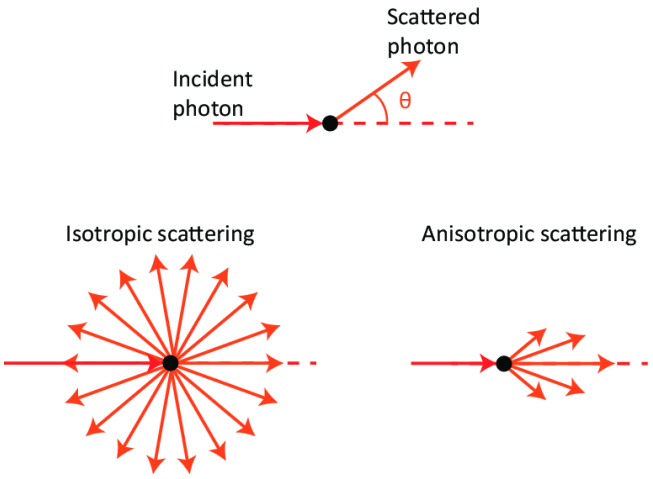

Figure 2.5: Isotropic scattering and anisotropic scattering..
[20]

$$\log \frac{I}{I_0} = -\mu_a L \tag{2.2}$$

$$\log \frac{I}{I_0} = -(\mu_a + \mu_s) L \tag{2.3}$$

$$\log \frac{I}{I_0} = -(\mu'_s + \mu_a) \times L \tag{2.4}$$

$$\mu'_s = (1 - g) \times \mu_s \tag{2.5}$$

I = transmitted intensity

I_0 = initial intensity of light

L = Total path length of light

μ_a = absorption coefficient

μ_s = scattering coefficient

μ_s' = reduced scattering coefficient

g = scattering anisotropic factor

2.2.2 Challenges of UV Excitation

The previous section has already discussed the attenuation of light in biological tissues. Depending on the wavelength of the photons, different tissues exhibit markedly different attenuation coefficients, which significantly influence light penetration performance. NADH specifically absorbs photons at 340nm; ideally, illuminating the body externally with 340nm UV light should enable NADH excitation and detection. However, figure2.6 illustrates the limited penetration depth of light in human tissues as a function of wavelength [21]; as the wavelength increases from shorter (UV) to longer (NIR), the penetration depth correspondingly increases.

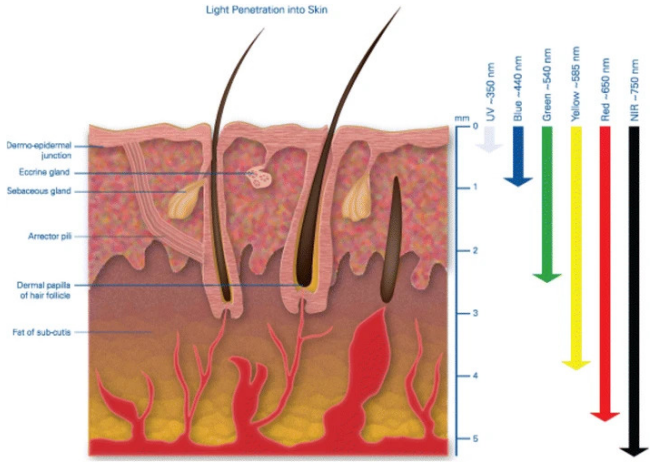

Figure 2.6: Light penetration into skin illustrating the depth to which wavelengths penetrate human skin.

[21]

Since 340nm light belongs to the UV spectrum, it exhibits poor penetration capabilities through tissue. When UV light is applied externally, it is severely attenuated and absorbed by the superficial tissue layers, preventing it from reaching the myocardium. According to Figure2.6, only NIR light shows sufficient tissue penetration.

In combination with the equations discussed in Section 2.2.1, and assuming an initial light intensity of 10^6 , the light is modeled to pass sequentially through the skin, fat, muscle, bone, additional fat, and lung tissues, as shown in Figure2.3. However, the lung exhibits an extremely high absorption coefficient for photons, creating a major bottleneck in photon transmission to the cardiac muscle. By slightly adjusting the incident angle and entry point of the light source, it is possible to bypass the lung and instead traverse an additional layer of fat, thereby reducing overall attenuation. Based on this adjustment and the absorption coefficients of the relevant tissues (summarized in the accompanying Chart 2.1), the simulation results indicate that only approximately 0.3% of incident 808nm photons can reach the myocardium.

	μ_a, cm^{-1}	μ_s', cm^{-1}	Reference
Skin	0.12	19	[22]
Fat	0.085	11.5	[22]
Muscle	0.3	7	[22]
Bone	0.1	19.5	[23]

Table 2.1: The absorption coefficient and the reduced scattering coefficient of the different tissues. The raw graph show in the appendix A

While NIR light such as 808nm demonstrates relatively better penetration, the final transmission rate is still extremely low, and more importantly, 808nm photons cannot excite NADH molecules directly due to the mismatch in excitation wavelength. This leads to a critical challenge: how to convert NIR photons into UV photons capable of exciting NADH via photoluminescence mechanisms?

2.3 Upconverting nanoparticles

2.3.1 Upconversion mechanism

In the previous section, under irradiation of a 10^6 anisotropic light source, only 0.3% of the NIR photons can finally reach the heart. To achieve the NIR to the UV conversion, a special case of photoluminescence called Stokes/Anti-Stokes luminescence can be done, as shown in Figure2.7. When a system absorbs a photon, it acquires energy and transitions to the excited state. The system returns to the ground state by emitting photons. The energy difference between the absorption and emission photons can be separated into two situations: when the system absorbs a short-wavelength photon and emits a long-wavelength photon, which means energy loss through vibrational relaxation. This phenomenon is called Stokes-type emission. However, if the emitted photons have a higher energy than the absorbed photons, this process is referred to as anti-Stokes emission. Anti-Stokes emission happens in a single system, and the excess energy is related to thermal effects and vibrations.[24].

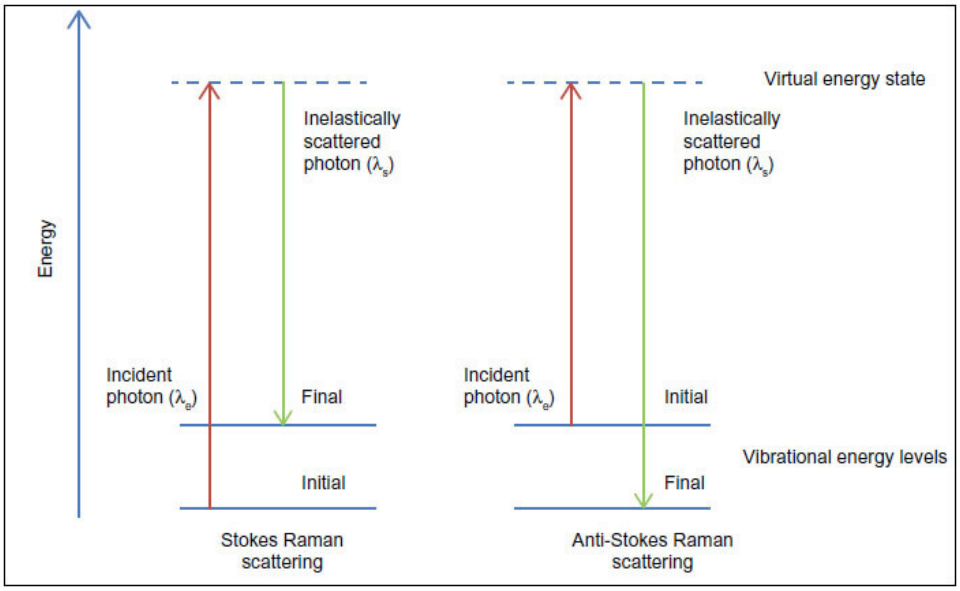

Figure 2.7: Schematic showing the difference between Stokes and anti-Stokes Raman scattering. [25]

Based on the definition of the energy difference, the anti-Stokes also represents the other complex mechanism called upconversion. It refers to the shorter-than-excitation-wavelength optical process, which is the sequential absorption of several long-wavelength photons to generate a short-wavelength photon.

Since the energy gap between the NIR and UV is large, at least absorbing 4 to 5 NIR photons can finally emit a UV photon. A single system cannot achieve a large conversion between them. Li et al. show the upconversion mechanism of the Pr-doped system. Excited by two 488nm photons, the system can emit a 314nm photon[26]. It shows that without the assistance of the other system. It can not acquire the energy transfer. Figure2.8 shows that Energy Transfer Upconversion is the most common upconversion model. The ion absorbs one photon to the excited state and then transfers its energy to neighbouring ions, resulting in the population of a highly excited state ion. Figure2.9 shows the two energy transfer processes. For the radiative energy transfer, when one system absorbs a photon and excites the ion to a high energy level, the ion relaxes and emits the photon, which the other system collects and goes through the same process. However, in multiple systems, upconversion occurs through nonradiative energy transfer. The most significant difference compared with the radiative transfer is that the energy is not transferred as photons but phonons. This mutual interaction can greatly improve the transfer efficiency.

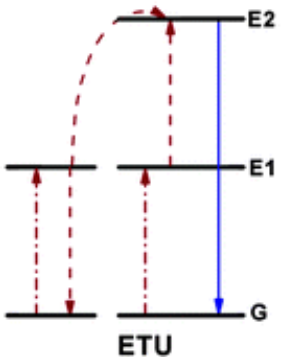

Figure 2.8: Principal upconvertion processes for lanthanide-doped crystals energy transfer upconversion (ETU). The dashed/dotted, dashed, and full arrows represent photon excitation, energy transfer, and emission processes.

[27]

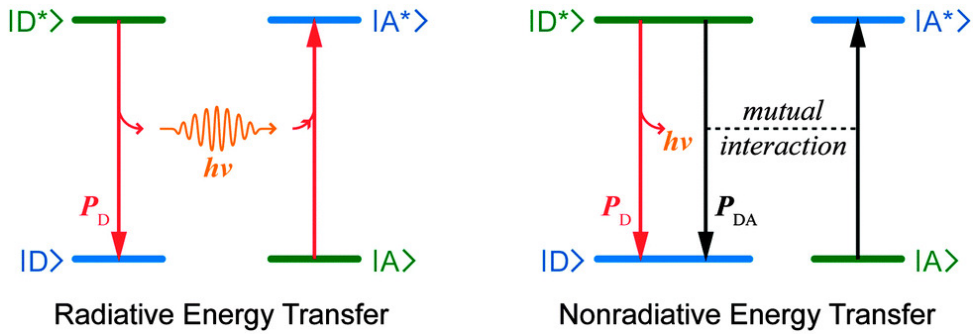

Figure 2.9: Principle energy transfer processes between a donor (D) and an acceptor (A)

[28]

For radiative energy transfer, they can operate over a very long distance. Achieving nonradiative energy transfer requires the two systems to be close to each other. Figure2.10(a) shows the mechanism of the nonradiative energy transfer. The interaction depends on the Dexter energy transfer, which is transferred through the electrons. The multipolar interaction is in charge of Forster energy transfer (FRET); the dipole-dipole interaction determines the energy transfer. The exchange interaction requires an interaction distance of less than 1nm, requiring the acceptor and donor to overlap in the wave function. The probability decreases exponentially and typically vanishes for separations beyond 0.5nm. Figure2.10(b) is the effect of transition strength in the acceptor on the critical distance of a multipolar transfer. Based on the spectral range, the efficiency of the sharp and discrete absorbers for the wavefunction is different. The line absorber is decaying, obviously, with a small distance function. The efficiency of the band absorber drops to 50% when the distance between the acceptor and the donor is 3nm.

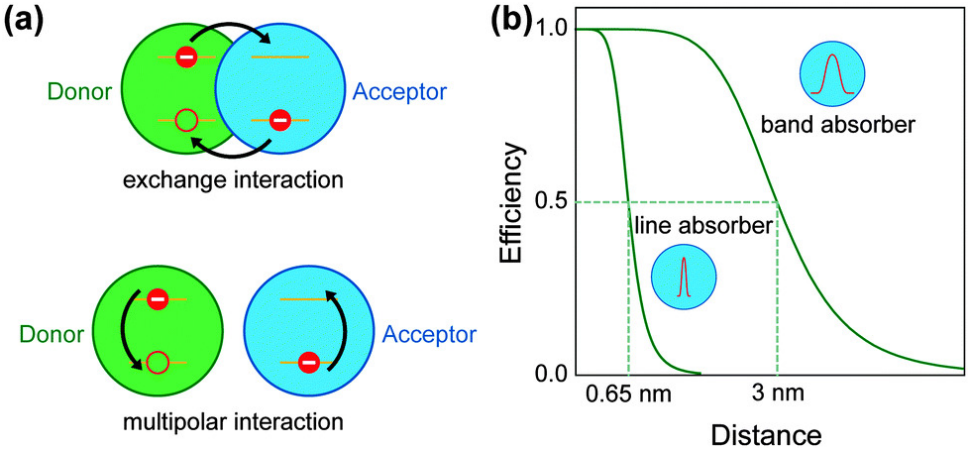

Figure 2.10: (a) Schematic illustration of energy transfer through exchange and multipolar interactions, respectively. (b) The effect of transition strength in acceptor on the critical distance of a multipolar transfer.

[28]

2.3.2 Structure of the nanoparticles

The structure of the Upconverting nanoparticles is designed to maintain high efficiency and stable viability. For multiple systems, nanoparticles can be classified into three components (Figure2.11). The first is the sensitizers(S), which aim to absorb NIR photons. These long-wavelength photons excited the ions from the ground state and then transferred the energy to their neighbor by nonradiative energy transfer. The second part is the activators(A/A'). They have several energy states that accept the energy from the sensitizer, which absorbs the long-wavelength photons and converts them to short-wavelength photons. In some situations, especially near-infrared II, a migrator(M) is required to transfer energy. The activator absorbs six or seven photons to reach the excited state[29].

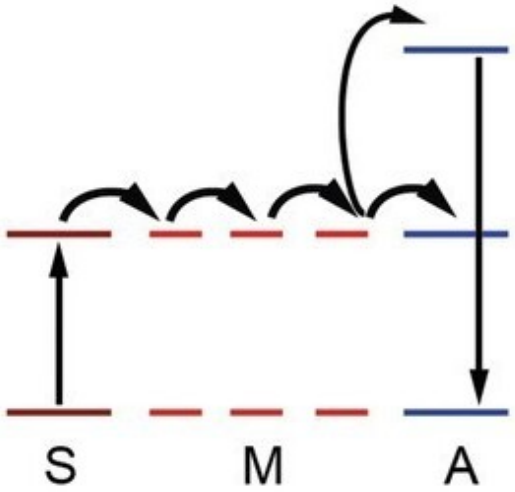

Figure 2.11: Schematic illustration of typical energy transfer pathways from the sensitizer to the activator. S, sensitizer; A, activator; M, migrator.

[29]

The efficiency of the upconverting nanoparticles is normally influenced by concentration and surface quenching. When the concentration of the sensitizers is increased, they can absorb more photons.

However, more photons generated cannot improve efficiency. Inversely, high doping levels of the sensitizers show an apparent quenching of luminescence. The average interparticle distance decreases. Figure2.10(b) shows that the proximity between the sensitizers and the activator can increase efficiency. However, high-level doping also results in closeness between the sensitizers; cross-relaxation causes the ions to return to the lower energy state instead of transferring energy.

The structure has lattice defects, which act as the nonradiative center to dissipate the energy for surface quenching. Figure2.12 illustrates the surface of the nanoparticles; the ligand and surface defects can interact with the particles, leading to energy loss. To prevent energy loss, forming an inert shell to cover the nanoparticles can avoid the communication of the outer environment, and the core-shell model ensures the high transmission of the photons.

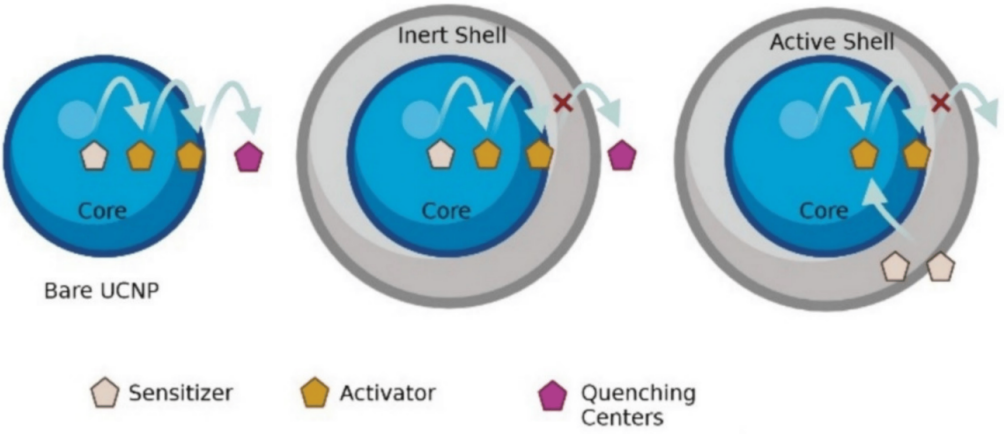

Figure 2.12: The surface quenching of the UCNPs.
[30]

2.4 Optical Filter Design

During the upconversion process, nanoparticles commonly emit light at multiple wavelengths. Upon absorbing near-infrared (NIR) photons, they can simultaneously emit both blue and ultraviolet (UV) light. Given that the sensor design relies on blue fluorescence emitted from NADH to quantify its concentration, interference from the blue emission of the upconverting nanoparticles (UCNPs) can compromise detection accuracy. Therefore, it is crucial to incorporate a spectral filter that blocks blue light while allowing UV photons to pass through.

An interference filter operates based on the principles of constructive and destructive interference. When two light waves have a phase difference of an integer multiple of ($2m\pi$, n = 1, 2, 3...), they interfere constructively, resulting in signal enhancement. In contrast, a phase difference of $(2m+1)\pi$ leads to destructive interference, causing attenuation of the signal. Based on the interference principle, the filter structure—referred to as a Fabry–Perot filter and illustrated in Figure2.13—consists of a mirror stack and a resonant cavity.

The accumulated phase during light propagation through a dielectric layer is related to the optical path length and the wavelength by

$$\Delta\phi = \frac{4\pi nd}{\lambda}, \tag{2.6}$$

where n is the refractive index and d is the physical thickness. Constructive interference occurs when $\Delta\phi = 2m\pi$, and destructive interference occurs when $\Delta\phi = (2m+1)\pi$. This leads to the general

condition $2nd = m\lambda$, which forms the foundation for optical thickness design in both the mirror and cavity regions.

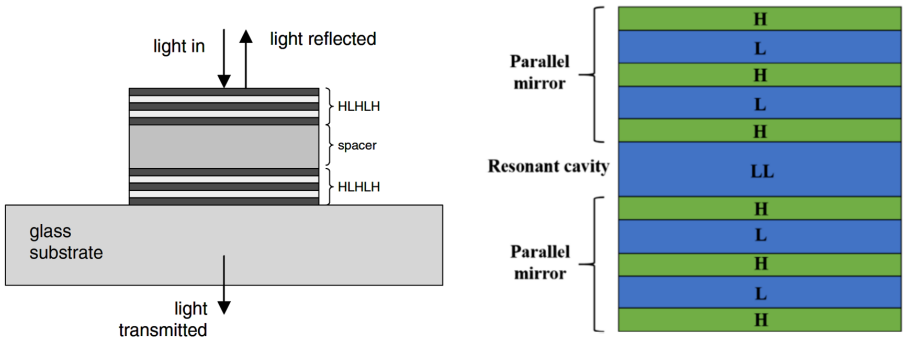

Figure 2.13: Structure of the Fabry-Perot filter. Left: Design by Koonen, T. (2006). Right: Pimenta et.al.

[31] [32]

The mirror stack consists of alternating high (H) and low (L) refractive index layers, forming repeating (HL) units. As the number of these repeating units increases, the reflectance at undesired wavelengths improves; however, the overall thickness of the filter also increases, which may reduce transmission efficiency at the desired wavelength. The detailed design strategy will be discussed in the Methods section. As shown in Figure2.13, light entering the mirror stack undergoes multiple reflections and partial transmissions at each interface. The optical path length of each round-trip within a single layer is $2nd$. To suppress an unwanted wavelength, the transmitted waves must interfere destructively, requiring a phase difference of π. Substituting into Equation2.6, we obtain

$$\frac{4\pi nd}{\lambda} = \pi \quad \Rightarrow \quad d = \frac{\lambda}{4n} \tag{2.7}$$

This condition defines a quarter-wave layer, which causes destructive interference among transmitted components and constructive interference among reflected components. As a result, reflectivity at the undesired wavelength is enhanced.

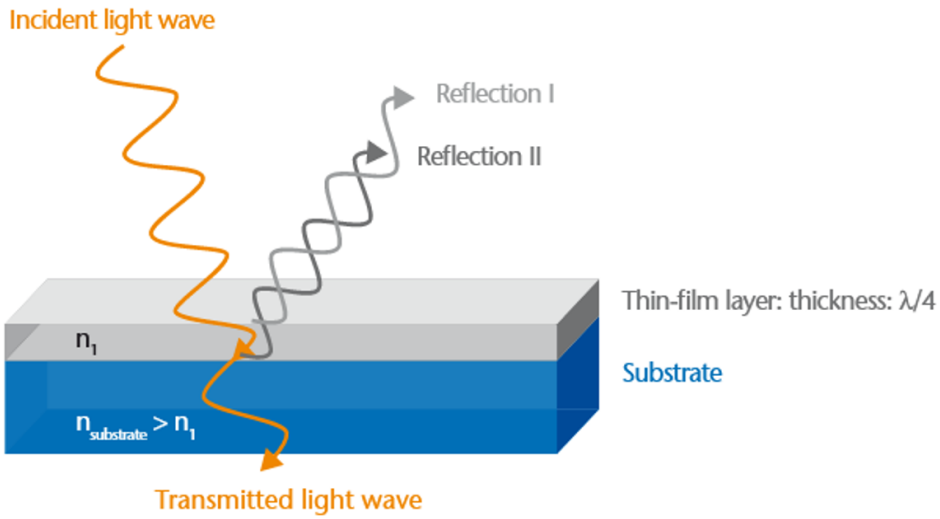

Figure 2.14: Mechanism of the Mirror Stack

In contrast, light passing through the cavity region undergoes multiple reflections between the top and bottom mirror stacks. When the round-trip optical path satisfies $2nd = \lambda$, corresponding to a total phase shift of 2π, the transmitted waves become in phase and interfere constructively. This defines the half-wave cavity condition:

$$\frac{4\pi nd}{\lambda} = 2\pi \quad \Rightarrow \quad d = \frac{\lambda}{2n} \tag{2.8}$$

allowing the desired wavelength to transmit through the cavity with high efficiency.

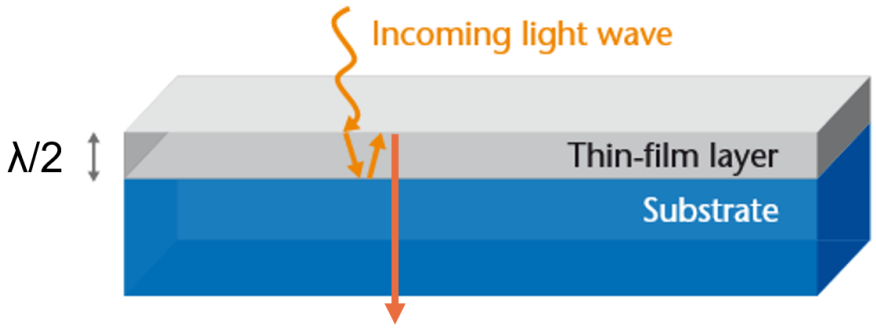

Figure 2.15: Mechanism of the Cavity

2.5 Material Selection

For the design of implantable sensors, all materials must be evaluated with respect to biocompatibility, which remains the foremost consideration to ensure safety within the human body. Compared to bulk materials, nanoscale sensors offer higher sensitivity and integration potential. However, due to their high surface-to-volume ratio, nanoparticles are more prone to interactions with the surrounding environment, which may lead to undesired surface quenching effects [33]. When implanted in vivo, foreign body responses—immunological reactions aimed at rejecting the implanted device—can be triggered[34]. In particular, contact between blood and the sensor can result in the adsorption of blood proteins on the sensor's surface, forming a fibrin matrix and triggering inflammation. The use of biocompatible materials in conjunction with immunomodulatory agents can reduce this immune response[35]. Moreover, nanoscale implants can potentially reduce the severity of these biological responses due to their minimal physical footprint.

In addition to biocompatibility, biodegradability is highly desirable. A biodegradable sensor can perform reliably for a designated period and naturally degrade within the body, thereby avoiding the need for surgical removal. Currently, most Upconverting nanoparticles (UCNPs) are not biodegradable. Recent studies have identified a promising host material, K_3ZrF_7, featuring a soft lattice structure that enables biodegradability, with in vivo degradation observed within 60 minutes [36]. When doped with Yb^{3+} and Er^{3+} and excited at 980 nm, K_3ZrF_7 can emit red light. However, compared to conventional host lattices, this soft lattice exhibits higher phonon energy, which facilitates non-radiative relaxation and significantly quenches short-wavelength emissions. As a result, performance at UV and blue wavelengths is compromised, rendering current biodegradable options insufficient for applications requiring low-wavelength emissions.

2.6 Objective of the research

Current technologies for monitoring cardiac oxygenation can be broadly divided into two categories. The first category includes hospital-based devices, which are often bulky and stationary. These systems can provide accurate measurements but cannot support continuous real-time monitoring in daily life. Their use is further limited by high demand and competition for clinical resources. The second category comprises implantable sensors, which, once surgically placed, can potentially offer continuous monitoring. However, existing implantable approaches typically rely on an internal battery, which increases device size, limits operational lifetime, and requires replacement surgeries that pose additional clinical risks.

To address these limitations, this research proposes a battery-free implantable sensor powered by externally delivered near-infrared (NIR) light. NIR photons, capable of penetrating deep into tissue, are converted into ultraviolet (UV) photons via upconverting nanoparticles (UCNPs) to excite the intrinsic luminescence of NADH for oxygenation assessment. Despite its promise, this approach faces significant challenges: the low UV upconversion efficiency of UCNPs, substantial tissue attenuation of NIR light, and spectral overlap between UV emission and undesired blue emission that can compromise measurement accuracy. Building upon the identified limitations and challenges, this study seeks to address the following key research questions:

- What UCNP compositions and nanostructures can achieve the highest UV upconversion efficiency for in vivo NADH excitation?
- How can excitation intensity be optimized to ensure effective UCNPs activation while avoiding tissue heating or phototoxicity?
- Which optical filter design can most effectively suppress blue emission while maintaining high UV transmission?

Chapter 3

Methods

The selection of upconverting nanoparticles and the design of the Fabry–Perot filter represent two key components in the development of the light emitter. These components are integrated into a unified emitter architecture based on their individual and combined optical properties. In addition, systematic evaluation of both elements is essential to ensure overall emitter functionality and efficiency. Material characterization techniques are employed to analyze the structural and luminescent properties of the nanoparticles, while optical testing setups are used to quantify the spectral behavior and transmission performance of the integrated emitter system. These aspects will be discussed in detail in the following sections.

3.1 Upconverting nanoparticles

3.1.1 Choice of Material

As discussed in Section 2.2, the upconversion mechanism is governed by three key components: sensitizers, activators, and migrators. Figure 3.1 illustrates the structure of the upconversion nanoparticles (UCNPs), in which these dopants are uniformly incorporated into the host lattice. To enhance optical efficiency, an inert shell is often coated around the core to suppress surface quenching and prolong the luminescence lifetime.

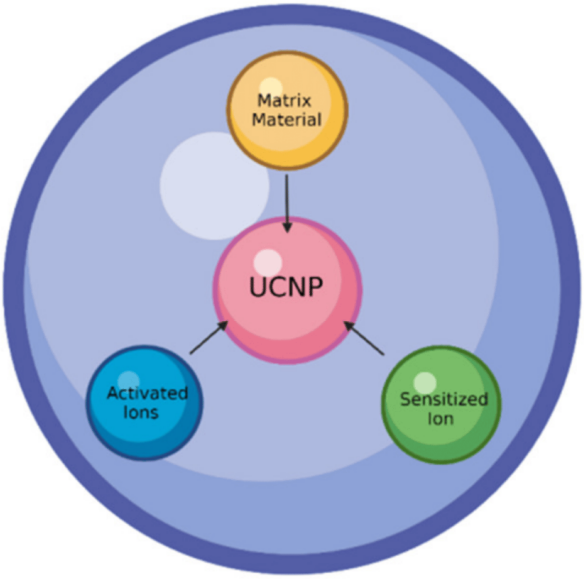

Figure 3.1: The structure of the upconverting nanoparticles.
[30]

To achieve NIR-to-UV conversion, lanthanide ions are employed due to their broad upconversion capabilities, which arise from 4f–4f electronic transitions. These transitions involve the 4f orbitals, which exhibit multiple sharp energy levels resulting from spin–orbit coupling and crystal field interactions [28]. The outer 5d orbital acts as a shield, protecting the 4f electrons from environmental perturbations. This shielding effect enhances the photostability and reduces non-radiative energy losses, thereby improving upconversion efficiency across a wide spectral range. However, the same shielding effect also leads to narrow absorption cross-sections, resulting in inefficient absorption of excitation photons. In addition, non-radiative energy transfer between dopant ions requires extremely short donor–acceptor distances, as illustrated in Figure2.10. These constraints highlight the need for precise control of dopant distribution and interionic spacing during nanoparticle synthesis. Lanthanide-based UCNPs are also promising for implantable sensors due to their low toxicity, high chemical stability, and biocompatibility. In a study by Jing Zhou et al., B16-F0 cells were incubated with 0.5 mg/mL lanthanide-based nanoparticles for 48 hours and then exposed to 980nm laser irradiation at various power levels. As shown in Figure3.2, no significant cytotoxic or phototoxic effects were observed. Both nanoparticle-treated and untreated cells maintained high viability, demonstrating the biosafety of lanthanide-based UCNPs and the potential applicability of upconverted UV light in biological environments.[37].

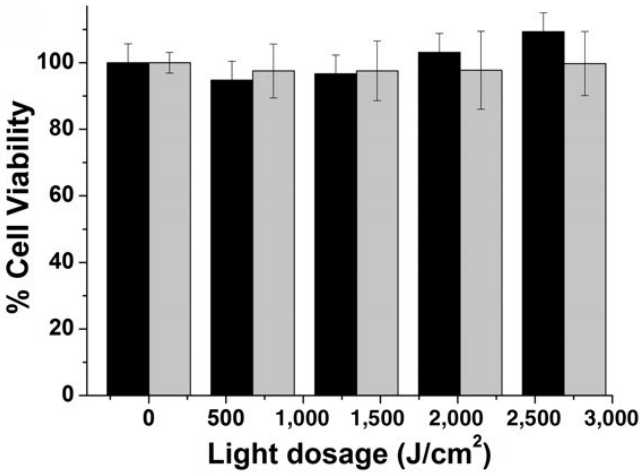

Figure 3.2: Viability of B16F0 cells without (black) and with (gray) NIR-to-UV lanthanide nanoparticles exposed to various doses of 980nm Continuous Wave NIR laser

[37]

Sensitizer

The sensitizer plays a crucial role in absorbing long-wavelength photons and transferring the harvested energy to activator ions. Depending on the excitation wavelength, three primary categories of sensitizers are considered in this project, as illustrated in Figure3.3.

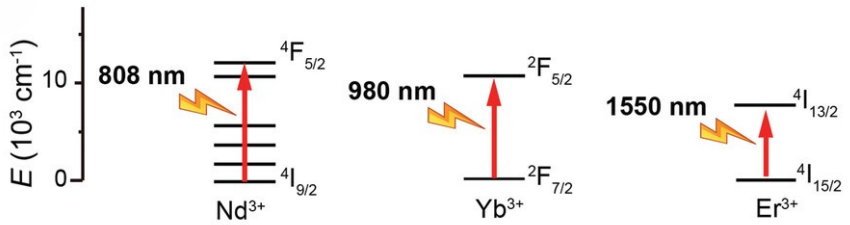

Figure 3.3: Energy level diagrams of typical upconversion sensitizers for 808, 980, and 1550nm excitations.

[29]

Among these, Er^{3+} is considered a safer option compared to other sensitizers, as it can be excited by 1550nm photons within the NIR-II window—a wavelength range that is regarded as eye-safe and exhibits minimal tissue absorption [38]. However, due to the low photon energy at 1550nm, achieving ultraviolet upconversion requires multiphoton absorption processes, which introduces significant nonradiative losses and poses a major efficiency challenge [39].

Excitation at 808nm offers a practical advantage over the more commonly used 980nm in biomedical applications, since biological tissues exhibit maximum optical transparency in the 700–900nm window [40, 29]. Nd^{3+} ions, which absorb efficiently at 808nm, are commonly employed as sensitizers. However, their excited states are susceptible to cross-relaxation with activator ions, which reduces upconversion efficiency. To address this, Yb^{3+} ions are introduced as energy migrators. Codoping with both Nd^{3+} and Yb^{3+} facilitates sequential energy transfer from Nd^{3+} to Yb^{3+}, thereby suppressing cross-relaxation pathways and enhancing overall upconversion performance.

Water Absorption

Another study compared the absorption spectra of water and Yb^{3+} based nanoparticles. As shown in Figure3.4, both exhibit a strong absorption peak near 980nm, indicating that when 980nm photons penetrate biological tissues, a substantial portion of the energy is absorbed by water rather than by the nanoparticles[41]. Given that the human body is composed of approximately 50% water, this absorption leads to considerable photothermal conversion, as water converts photon energy into heat, resulting in localized temperature elevation.

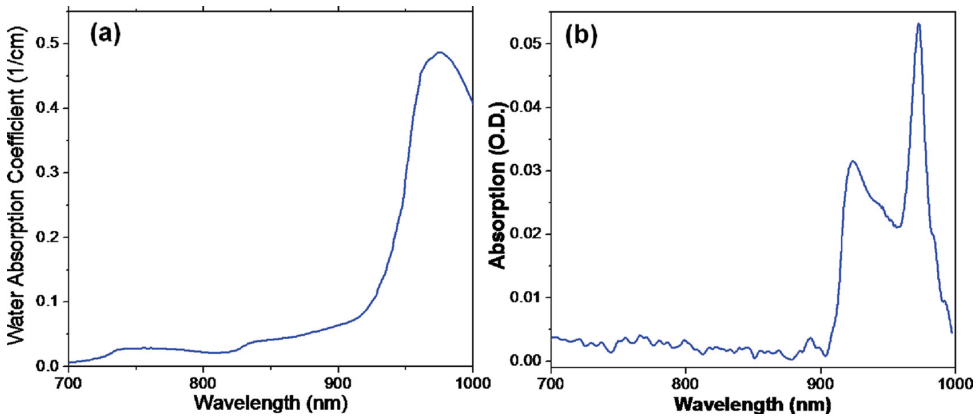

Figure 3.4: (a) Optical absorption spectrum of water in the NIR range (b) Absorption spectrum of UCNP colloid suspension.

[41]

To quantify this effect, the researchers conducted in vivo experiments on mice, comparing the photothermal response under 980nm and 808nm laser irradiation, as shown in Figure3.5. Under 980nm excitation, tissue temperature rapidly increased from room temperature to over 30°C within 50 seconds, posing potential risks to long-term implantable devices that rely on 980nm–excited sensitizers. In contrast, no significant temperature increase was observed within 300 seconds of 808nm laser exposure, highlighting the superior thermal safety and operational stability of 808nm excitation over 980nm.

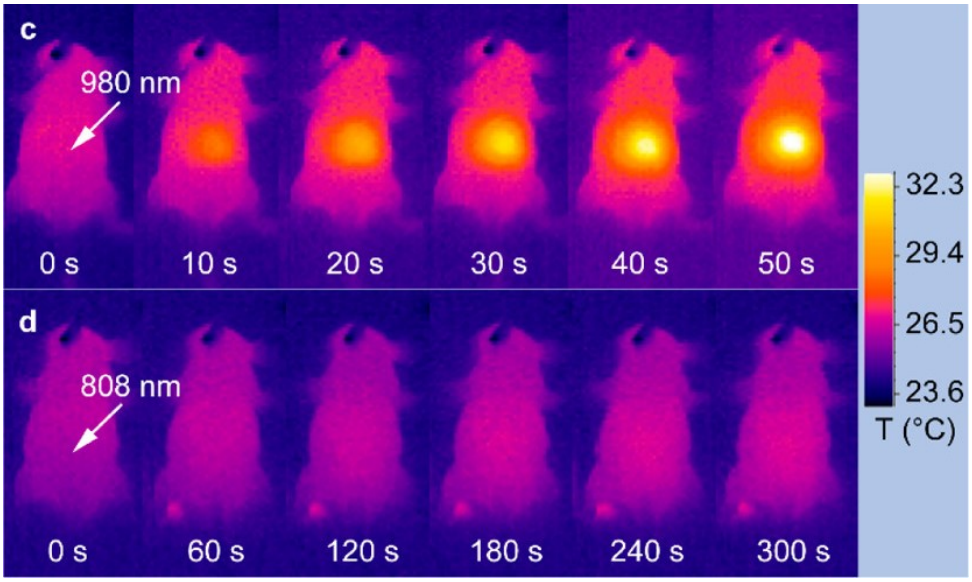

Figure 3.5: Infrared thermal image of a nude mouse during continuous 980nm laser irradiation for 50s and 808nm laser irradiation for 300s.

[42]

Host Material

As discussed in the structure of upconverting nanoparticles (UCNPs), sensitizer and activator ions are typically doped into a crystalline host matrix, which serves as the medium for energy absorption, transfer, and emission. Chart3.1 summarizes commonly used host materials for UCNPs, and the most critical parameter for evaluating these materials is their phonon energy, which reflects the intrinsic vibrational energy of the crystal lattice.

Material	**Highest Phonon Energy [cm^{-1}]**
Phosphate glass	1200
Silica glass	1100
Fluoride glass	550
Chalcogenide glass	400
$LaPO_4$	1050
Yttrium aluminum garnet	860
YVO_4	600
LaF_3	300
$LaCl_3$	240

Table 3.1: Highest phonon lattice energy of commonly used matrices for rare-earth ions.

[43]

As described in the previous section, the upconversion mechanism relies heavily on nonradiative energy transfer processes, which are facilitated by phonons. In this context, the phonon energy of

the host material can be viewed as a source of thermal noise; lower phonon energy minimizes multi-phonon relaxation losses, thereby improving upconversion efficiency.

Among the materials listed in Chart3.1, $LaCl_3$ and LaF_3—both members of the heavy halide family—exhibit relatively low phonon energies. However, their limited chemical stability makes them unsuitable for long-term biomedical applications. In contrast, metal oxides offer excellent chemical stability but possess high phonon energies, which significantly hinder upconversion efficiency due to enhanced nonradiative relaxation.

After evaluating various host candidates, fluoride-based materials have emerged as optimal choices, as they combine relatively low phonon energy with acceptable chemical and thermal stability. Fluoride hosts commonly incorporate ions such as Na^+, Ca^{2+}, and Y^{3+}, whose ionic radii are comparable to those of lanthanide dopants. This reduces lattice mismatch and suppresses defect formation, thereby lowering nonradiative energy losses. Among these, $NaYF_4$ is widely regarded as the most efficient and stable host material for UCNPs, due to its low phonon energy, high crystallinity, and excellent lattice compatibility [43].

In summary, Nd-based UCNPs offer a favorable balance between upconversion efficiency and biosafety, since excitation at 808 nm does not pose significant photothermal risks. When doped into a $NaYF_4$ host, the overall efficiency can be further enhanced due to the host's low phonon energy and structural compatibility with lanthanide dopants.

Based on these considerations, UCNPs from DiagNano™ were selected for this study. The chosen nanoparticle formulation is $NaYF_4$:Yb, Tm, Nd@$NaYF_4$, Yb, Nd. The emission spectrum is shown in Figure 3.6. In this structure, Nd^{3+} ions serve as sensitizers that absorb 808 nm photons, while Yb^{3+} ions function as energy migrators, facilitating transfer between Nd^{3+} and the activator Tm^{3+}. Tm^{3+} then converts the energy into emissions at 340nm and 475nm, corresponding to ultraviolet and blue light, respectively.

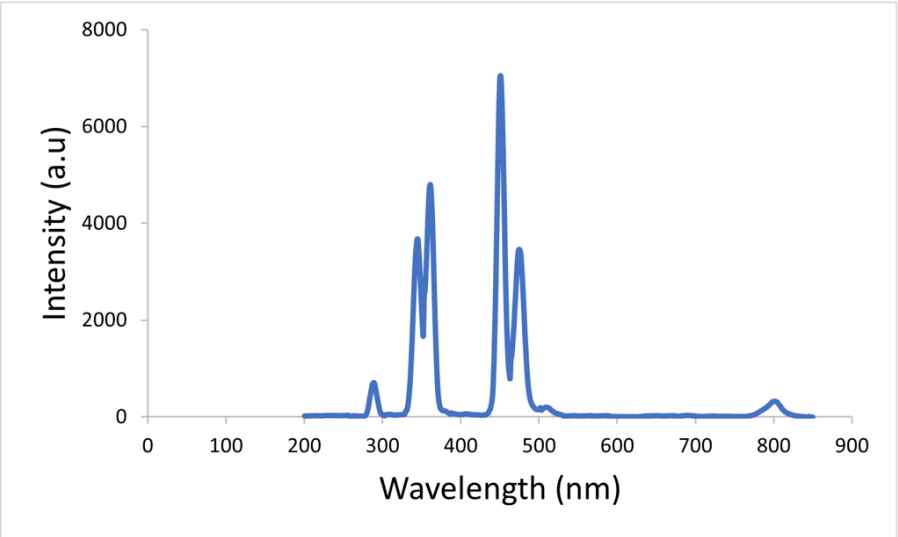

Figure 3.6: The emission spectrum of the UCNPs from the company. [44]

3.1.2 Nanoparticles Dispersion and Deposition

Since the upconversion efficiency of nanoparticles remains inherently low, the generation of UV photons becomes a critical limiting factor for practical applications. Given the challenges associated with structurally enhancing the intrinsic efficiency of UCNPs, maximizing the interaction between

the nanoparticles and the incident NIR light is a key design objective.
To achieve high photon capture, it is essential to deposit UCNPs onto the wafer substrate with maximum surface coverage and optical accessibility. Spin coating provides a convenient method for forming a uniform thin film of nanoparticles, thereby enhancing NIR photon absorption. However, adhesion between the UCNPs and the wafer substrate presents a challenge, as centrifugal forces during spin coating can cause partial detachment of the particles.
According to the manufacturer's fabrication protocol, the original UCNPs are hydrophobic due to the presence of oleic acid (OA) ligands on their surfaces [27]. Although the company removes the OA to render the particles water-dispersible, ligand removal alone does not ensure colloidal stability; the nanoparticles only temporarily disperse under ultrasonication and tend to reaggregate within a short time. Replacing the hydrophobic OA ligand with a hydrophilic functional group—such as a carboxyl group—can improve dispersion stability and enhance particle–substrate interaction [45, 46].
To further improve adhesion, oxygen plasma treatment is applied to the wafer surface, which increases surface hydrophilicity and enhances wettability, thereby improving nanoparticle retention.
As an alternative, drop casting is employed by directly applying the nanoparticle solution onto the wafer and drying it on a hot plate. Although this method does not yield a uniformly distributed or densely packed layer, it minimizes particle loss and ensures that the entire nanoparticle content is retained on the surface.
Both spin coating and drop casting were experimentally evaluated and compared. The deposition method that resulted in superior upconversion performance was selected for fabricating the light emitter. A detailed comparison and performance analysis of these methods are presented in the following chapter.

3.2 Fabry-Perot Filter

In the previous section, we discussed the fundamental structure of the Fabry–Perot filter and its associated design principles. According to the emission spectrum shown in Figure3.6, the upconversion nanoparticles exhibit two prominent emission peaks at approximately 365nm and 475nm. NADH molecules absorb photons near 365nm and subsequently emit fluorescence centered around 469nm, which spectrally overlaps with the 475nm emission from the UCNPs. This overlap introduces significant optical interference, thereby compromising the accuracy and reliability of NADH fluorescence measurements. To address this issue, a Fabry–Perot filter was specifically designed to suppress the 475nm emission while allowing efficient transmission of the 365nm excitation light. This spectral selectivity improves the signal-to-noise ratio and enables accurate detection of NADH-derived fluorescence.

3.2.1 Choice of Material

The Fabry–Perot filter is composed of a mirror stack and a central cavity. The mirror stack consists of alternating layers of high (H) and low (L) refractive index materials arranged in a periodic structure. The selection of materials for these layers is guided by several key criteria:

- The materials must be biocompatible, and ideally biodegradable to further enhance in vivo compatibility.
- To ensure constructive interference and equal amplitude of reflected light waves, the refractive indices of the thin-film layers must satisfy specific optical conditions, as described in the following equation:

$$n_1 = \sqrt{n_{air} \cdot n_{substrate}} \tag{3.1}$$

Given that the refractive index of air is approximately 1, and the underlying substrate is SiO_2 with a refractive index of about 1.46, the ideal refractive index for the first layer becomes:

$$n_1 = \sqrt{1 \cdot 1.46} = 1.21 \tag{3.2}$$

Considering both the optical requirements and biocompatibility constraints, SiO_2 (as the low-index material) and Si_3N_4 (as the high-index material) are commonly selected as the dielectric constituents of the mirror stack. This material pair is widely reported in the literature for their favorable optical contrast, chemical stability, and compatibility with microfabrication processes [47].

3.2.2 Modeling

The refractive indices of SiO_2 and Si_3N_4 are approximately 1.46 and 2.0, respectively. For the mirror stack, which is designed to block light at 475nm, the optical thickness of each layer can be determined based on the quarter-wavelength condition:

$$t_{SiO_2} = \frac{\lambda}{4 \cdot n_{SiO_2}} = \frac{475nm}{4 \cdot 1.46} \approx 80nm \tag{3.3}$$

$$t_{Si_3N_4} = \frac{\lambda}{4 \cdot n_{Si_3N_4}} = \frac{475nm}{4 \cdot 2} \approx 60nm \tag{3.4}$$

For the cavity layer, which is intended to enhance transmission at 340nm, the optical thickness is set to one-half of the target wavelength:

$$t_{SiO_2} = \frac{\lambda}{2 \cdot n_{SiO_2}} = \frac{340nm}{2 \cdot 1.46} \approx 116nm \tag{3.5}$$

$$t_{Si_3N_4} = \frac{\lambda}{4 \cdot n_{Si_3N_4}} = \frac{340nm}{2 \cdot 2} \approx 85m \tag{3.6}$$

Following the design reported in the literature (Figure2.13), the complete structure of the Fabry–Perot filter is Air-HLHLH-2L-HLHLH-Substrate, which is illustrated in Figure3.7.

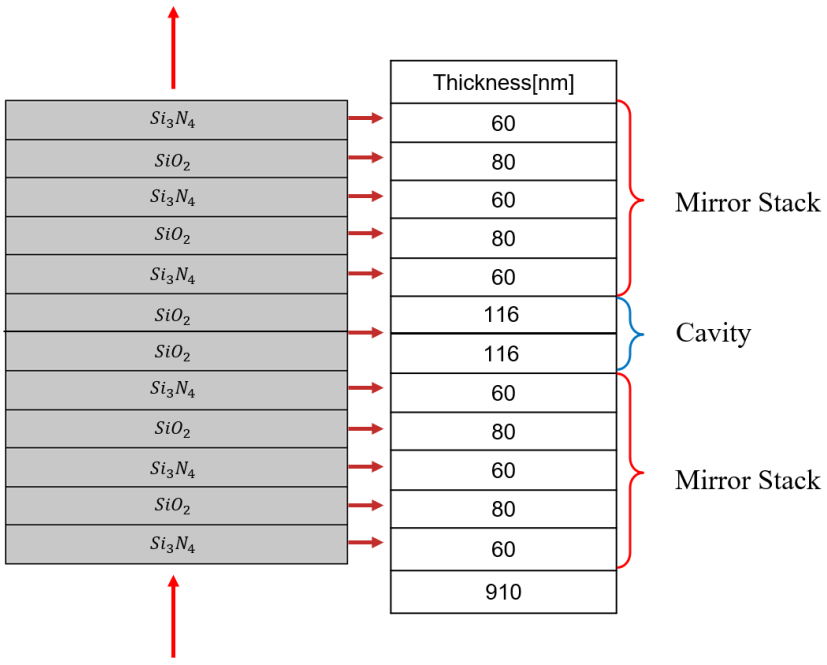

Figure 3.7: Scheme of the Fabry–Perot Filter Model.

3.2.3 Simulations

The previous section outlined the basic structure of the Fabry–Perot filter and derived the theoretical thickness of each constituent layer. To verify the feasibility of this design and evaluate whether the theoretical layer parameters deliver optimal spectral selectivity and transmittance, numerical simulations were conducted using optical modeling tools.

Fabry–Perot Filter Structure

Figure3.8 shows the simulated transmission spectrum of the current Fabry–Perot filter design. At 340nm, the filter exhibits a transmission of 90.9%, while at 469nm, the transmission drops to 4.9%, resulting in a transmission ratio of 18.55 between 340nm and 469nm. This result indicates high transmittance at the target UV wavelength and effective blocking at the blue wavelength, confirming the functionality of the design reported in the literature.

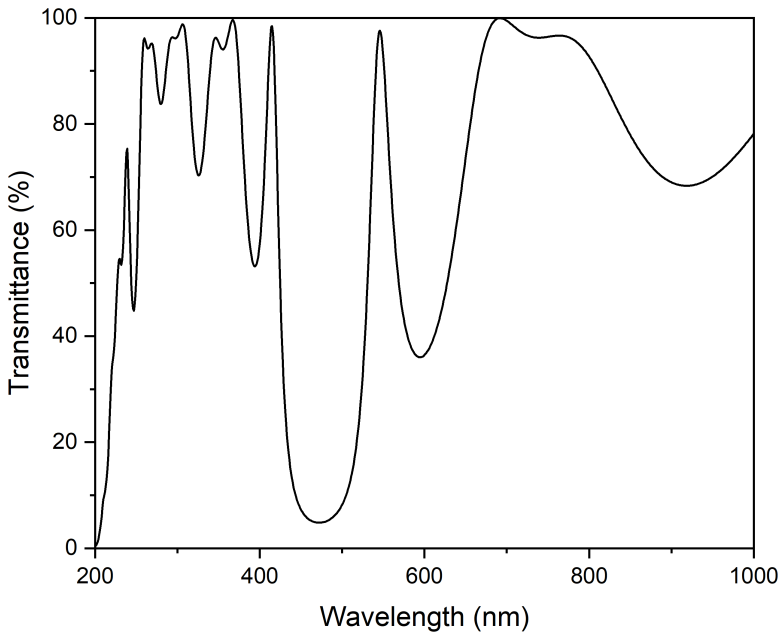

Figure 3.8: Simulation of the Fabry-Perot Filter.

Layer Thickness Optimization

To determine whether the theoretical thicknesses are optimal in practice, COMSOL Multiphysics simulations were conducted. By systematically varying the thicknesses of SiO_2 and Si_3N_4 from 40nm to 90nm in 2nm increments, a total of 676 unique layer configurations were generated and simulated. The transmission performance for each combination was evaluated at both 340nm and 469nm.
The simulation results are presented in Appendix B. In each plot, the x-axis represents the SiO_2 thickness, the y-axis indicates the transmittance, and each curve corresponds to a different Si_3N_4 thickness. To facilitate intuitive evaluation of filter performance, the transmission ratio ($\frac{t_{340nm}}{t_{469nm}}$) was calculated for all configurations shown in Figure3.9. The top five combinations with the highest transmission ratios are summarized in Table3.2.

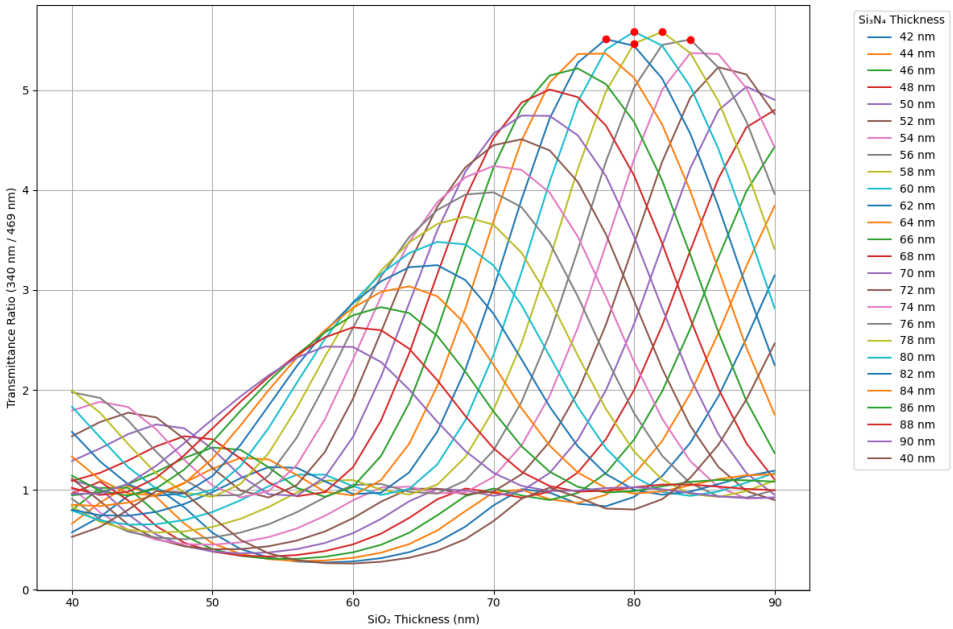

Figure 3.9: The ratio of the 340nm and 469nm.

	SiO_2, nm	Si_3N_4, nm
1	80	60
2	82	58
3	78	62
4	84	56
5	80	58

Table 3.2: The Top Five Thickness Combinations

The simulation results reveal that the optimal thicknesses are 80nm for SiO_2 and 60nm for Si_3N_4, which closely align with the theoretical predictions for the mirror stack configuration, where the thicknesses are designed to satisfy the quarter-wavelength condition at 475nm.

Fabrication Tolerance and Thickness Adjustment

During the fabrication of the Fabry–Perot filter, inevitable deposition errors may cause slight deviations in layer thickness, leading to variations in the optical performance. To account for these fabrication tolerances, this section investigates how global thickness variations affect the transmission spectrum.

Figure3.10 illustrates the spectral shifts caused by uniformly increasing or decreasing the thickness of all layers. When the overall thickness increases, the transmission curve shifts toward longer wavelengths (right shift); conversely, reducing the thickness causes a shift toward shorter wavelengths. This behavior is consistent with interference theory, where the optical path length determines the resonance condition.

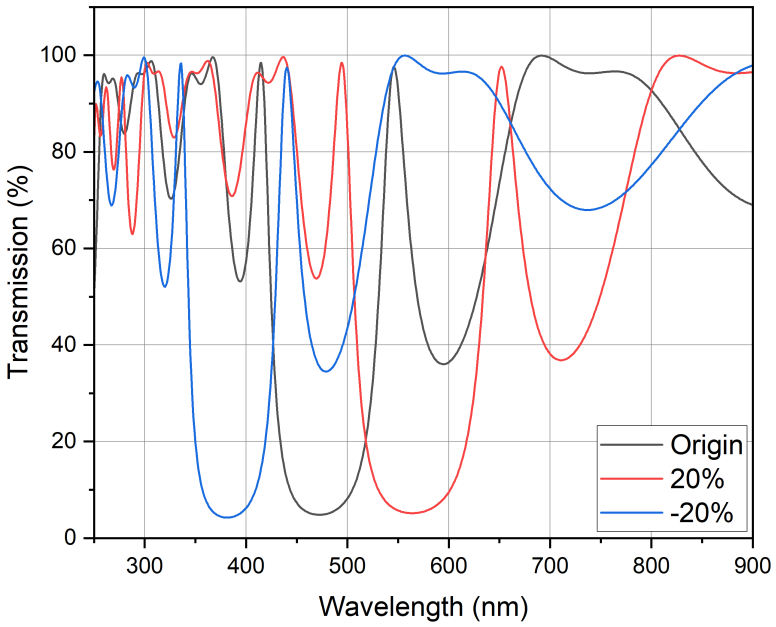

Figure 3.10: The curve shifts when entirely changing the structure. The rest of the curve is shown in Appendix C.

These results suggest that fine-tuning the total thickness after fabrication can further optimize the filter performance, especially if slight deviations from the design values are detected during inspection.

3.2.4 Process Steps

As discussed in the previous section, the structure and layer thickness of the Fabry–Perot filter are critical to its optical performance. Inductively Coupled Plasma Chemical Vapor Deposition (ICPCVD) is employed for thin-film deposition in this work. ICPCVD is a specialized form of CVD that utilizes inductively coupled plasma to activate the precursor gases, enabling deposition at lower temperatures while forming relatively dense and uniform films. This is particularly advantageous for optical filters, as it minimizes photon loss due to surface scattering from defects.

Both SiO_2 and Si_3N_4 layers are deposited by introducing their respective precursor gases into the chamber, where they undergo plasma-enhanced reactions to form dense films. However, the deposition rate and film quality are sensitive to the selected process recipe, including gas flow rates, power, and temperature settings. Moreover, slight variations in deposition conditions across different runs can introduce minor thickness errors, which—as discussed previously—can cause spectral shifts in the transmission curve.

To mitigate this issue, a calibration step using ellipsometry is performed prior to each full filter fabrication. Specifically, a test deposition is carried out using the predefined recipe to deposit a 1-minute layer of SiO_2 and SiN_4, respectively. The thicknesses of these test films are then measured using an ellipsometer. The measured values are used to calibrate the deposition rates of ICPCVD, ensuring that the final Fabry–Perot filter matches the intended design.

3.3 Structure design of the Light Emitter

Figure3.11 presents the fabrication flow of the light emitter. The device is constructed on a 1-inch fused silica wafer with a thickness of 25µm, which serves as the substrate. A Fabry–Perot filter is then deposited directly onto the substrate via inductively coupled plasma chemical vapor deposition (ICPCVD) to suppress blue light transmission while allowing ultraviolet (UV) light to pass. To improve the adhesion and distribution of nanoparticles, the filter surface can be treated with oxygen plasma prior to nanoparticle deposition. The upconverting nanoparticles (UCNPs) are subsequently applied onto the filter either by spin-coating to form a uniform layer or by drop-casting to maximize particle loading. Finally, to protect the UCNPs from environmental degradation, a thin, optically transparent Al_2O_3 encapsulation layer is deposited using atomic layer deposition (ALD).
Figure3.12 shows the integrated structure of the light emitter, incorporating all functional components. Upon illumination with near-infrared (NIR) light at 808nm, the upconverting nanoparticles (UCNPs) on the top layer convert the incident photons into both ultraviolet (UV, 360nm) and blue (450–470nm) emissions. With the NIR photons incident perpendicularly to the device surface, diffraction losses during conversion and transmission are minimized. The underlying Fabry–Perot filter is designed to suppress the blue emission while allowing UV light to pass through, thereby enabling selective excitation of target molecules such as NADH. A thin Al_2O_3 encapsulation layer protects the UCNPs from environmental degradation without significantly affecting optical transmission.

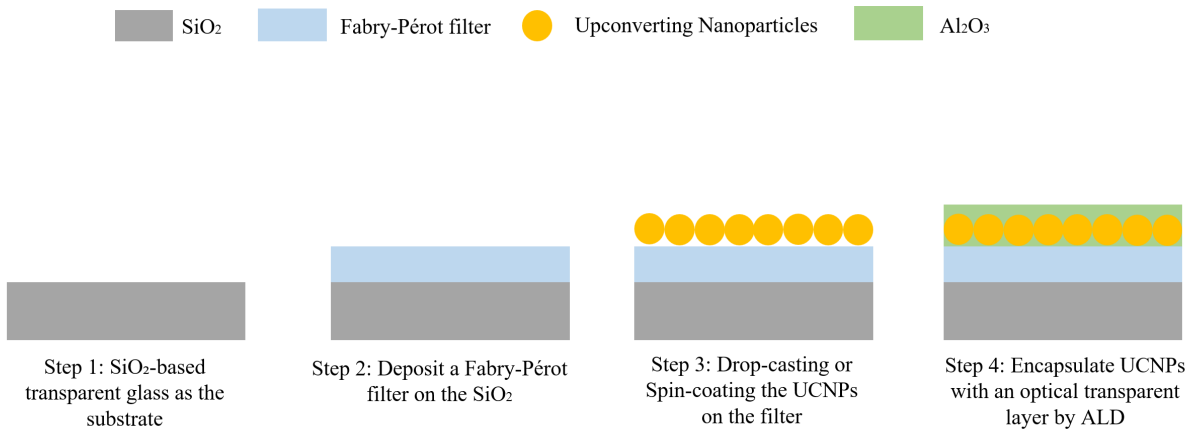

Figure 3.11: The flowchart of the Light Emitter.

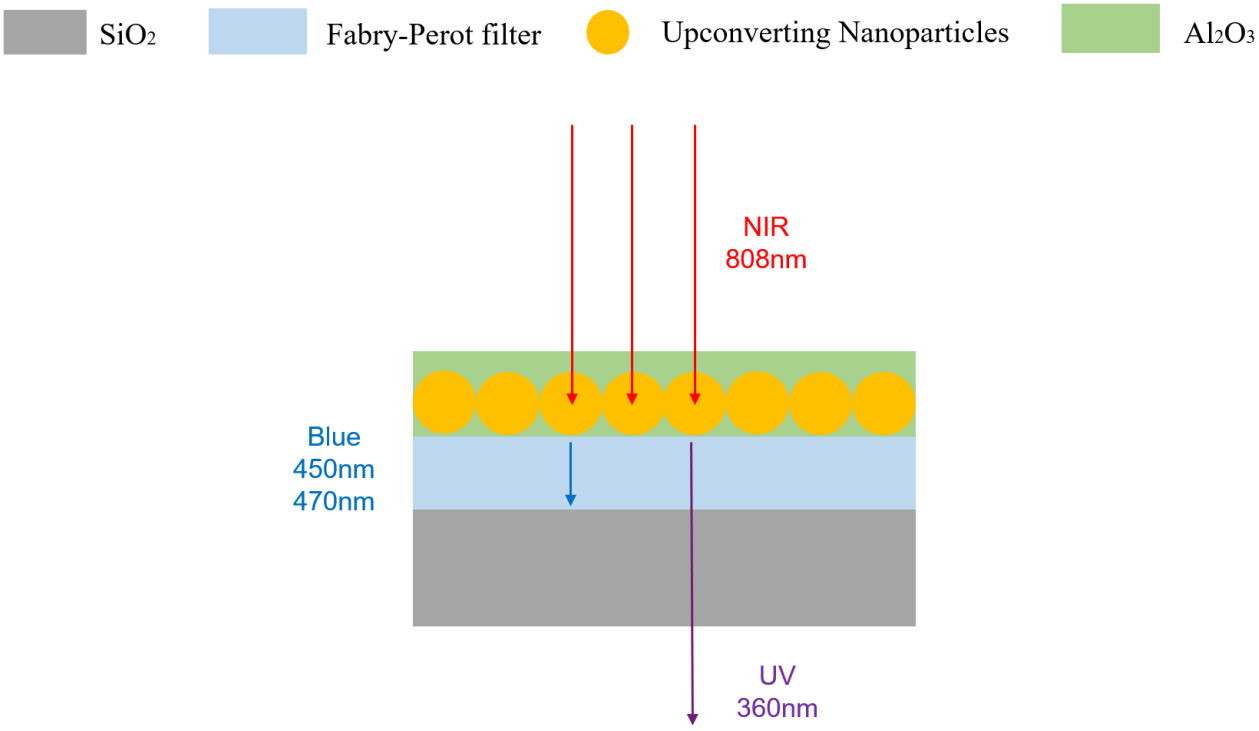

Figure 3.12: The Structure of the Light Emitter

3.4 Material Characterization

Different characterization methods can be used to evaluate the light emitter's performance. One method involves coating the upconverting nanoparticles on the substrate and analyzing the coating layer's thickness and wafer coverage. These results reflect the surface morphology and particle distribution of the sample.

3.4.1 Optical Microscopy (OM)

Optical microscopy uses visible light and lenses to magnify samples, allowing basic structural observation. However, the 30nm nanoparticles are below the resolution limit of OM, and the system's transparency limits light reflection, reducing image contrast. While OM cannot resolve individual nanoparticles, it can provide a rough estimation of wafer coverage due to visible stains from drop-casting. By analyzing these boundaries, the macroscopic distribution of particles can be assessed.

3.4.2 Scanning Electron Microscopy (SEM)

Following OM, SEM offers higher-resolution surface imaging. It uses an electron beam that interacts with atoms in the sample to generate surface and compositional signals, forming high-resolution images. Using the Hitachi S4800 in the Kavli Nanolab, SEM can resolve features down to 1nm at 15kV, meeting the resolution requirement. However, as the emitter is non-conductive, electron accumulation on the surface creates local electric fields that distort the image. To mitigate this, a thin gold coating is applied to form a conductive path for charge dissipation, thereby improving imaging quality.
Moreover, reducing the accelerating voltage from 15kV to 5kV can further optimize image clarity. Although this adjustment slightly compromises resolution, it minimizes electron penetration and surface charging, leading to clearer imaging of non-conductive samples.
However, SEM is inherently an invasive technique, as its imaging principle relies on continuous electron bombardment. With prolonged exposure and low adhesion between the nanoparticles and the substrate, the structural integrity of the sample may deteriorate over time, potentially affecting measurement accuracy.

3.4.3 Atomic Force Microscopy (AFM)

While OM and SEM assess surface coverage, AFM provides nanoscale topographic mapping. It scans the surface with a sharp tip to produce 3D images. By scanning a $10\mu m \times 10\mu m$ central region using Bruker FastScan AFM, the thickness of the nanoparticle layer can be quantified based on step height, offering insight into film uniformity and deposition efficiency.
However, directly measuring the nanoparticle thickness is challenging due to the wafer's inherent surface roughness, which can obscure the coating's actual height. To address this, a masking strategy is applied during sample preparation. A piece of adhesive tape is first placed on the wafer surface before drop casting the nanoparticles. After the coating process, the tape is removed, leaving a clean reference region adjacent to the coated area. Both regions are then scanned within the same AFM frame, allowing the step height between the coated and uncoated areas to be measured accurately. This approach enables a reliable estimation of the nanoparticle layer thickness.

3.5 Optical Test Setup

While the previous characterization methods focus on evaluating the morphology and surface coverage of the upconverting nanoparticles, additional experiments are required to assess the integrated emitter system's optical transmission and upconversion performance. By designing specific optical setups, the efficiency of the upconversion process and the filtering behavior of the Fabry–Perot structure can be systematically investigated.

3.5.1 Spectrometer

A spectrometer is an optical instrument that measures light intensity as a function of wavelength. Due to limitations in detector sensitivity, optical material transparency, grating efficiency, and resolution trade-offs, a single spectrometer cannot cover the entire UV–NIR range. Sensitivity often decreases near the detection range boundaries, resulting in higher background noise and spectral distortion. To obtain a complete UV–NIR spectrum, multiple spectrometers are typically used. These are generally categorized into UV–VIS, VIS–NIR, and FTIR types. In this work, a Maya2000 Pro spectrometer (155–380nm) and a FLAME spectrometer (360–1000nm) are employed in combination (Figure3.13) to provide a continuous spectral profile for sample evaluation. After acquisition, the spectrometer converts optical signals into electrical signals, which are processed and visualized using OceanView software. Two measurement modes are available. When a reference spectrum is acquired, the output represents relative transmittance with physical meaning. In this case, the x-axis represents wavelength (nm) and the y-axis represents transmittance (%), calculated as:

$$Transmission = \frac{Sample\ single}{Reference\ signal} \times 100\% \tag{3.7}$$

To obtain transmission spectra, a blank substrate is first placed at the sample position as the reference, representing full transmission without absorption. These two measurements—the blank spectrum and the background noise—are recorded to establish the reference signal, ensuring that the transmittance is defined as 100% when the blank sample is in place. The light source is then turned off to measure ambient background noise. Finally, the target sample is inserted and its transmission signal is recorded. In the second mode, no reference spectrum is used. The spectrometer directly displays the raw relative detector signal, expressed in arbitrary units (a.u.). Although this mode has no absolute physical meaning, it enables comparison of relative intensity under identical measurement conditions. Based on these principles, the spectrometer can be applied to measure both spectral transmission and emission characteristics of the sample.

Figure 3.13: (a) Maya2000 Pro spectrometer can detect signals from 155-380nm. (b) FLAME spectrometer can detect signals from 360–1000nm

Fabry-Perot Filter measurement

Following this methodology, spectrometers can be used to assess the transmission performance of the Fabry–Perot filter. Figures3.14 and 3.15 respectively illustrate the schematic and the real setup for the spectrometer-based measurement system. To enable broadband transmission characterization, a DH-2000 light source is used, which provides a stable and continuous output from 215–2500nm using a combination of a 25W deuterium lamp and a 20W halogen lamp[48]. Although its relatively low optical power is insufficient to excite upconversion particles, it is adequate for generating reliable transmission spectra. To ensure both optical intensity and directionality, a fiber optic is used to couple the light source to the optical setup. The fiber confines the photons to propagate along a defined axis, allowing the output beam to be directed toward the target location without misalignment. When photons exit the fiber into air, the refractive index change between the fiber core and air causes the beam to diverge according to the fiber's numerical aperture (NA). A collimating lens is therefore positioned immediately after the fiber output to transform the divergent beam into a parallel beam, maximizing the incident power on the sample. After passing through the Fabry–Perot filter, which selectively transmits the desired wavelengths, the transmitted photons are collected by a focusing lens. This lens concentrates the light onto the entrance of the receiving fiber optic, ensuring efficient coupling into the spectrometer for spectral analysis. If the resulting spectrum exhibits high transmission in the UV region and low transmission around 475nm, it indicates that the filter is functioning as intended, consistent with the simulation results. Conversely, if the measured spectrum significantly deviates from this expected pattern, thickness adjustments—based on the shifting principles described in Section 3.2.3 will be necessary to correct the spectral response.

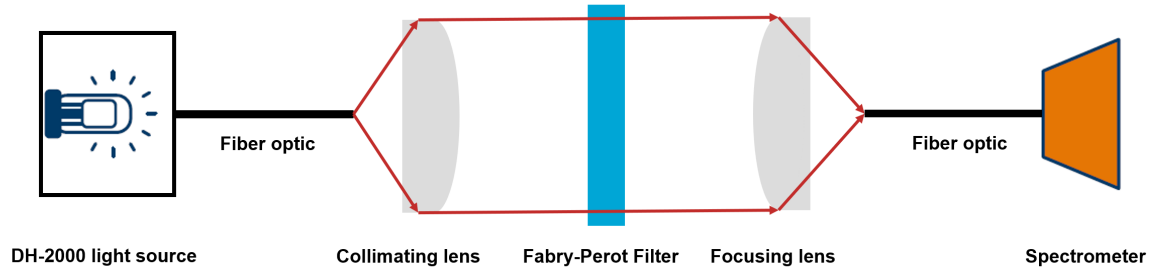

Figure 3.14: Schematic diagram of the spectrometer-based Fabry–Perot filter measurement setup.

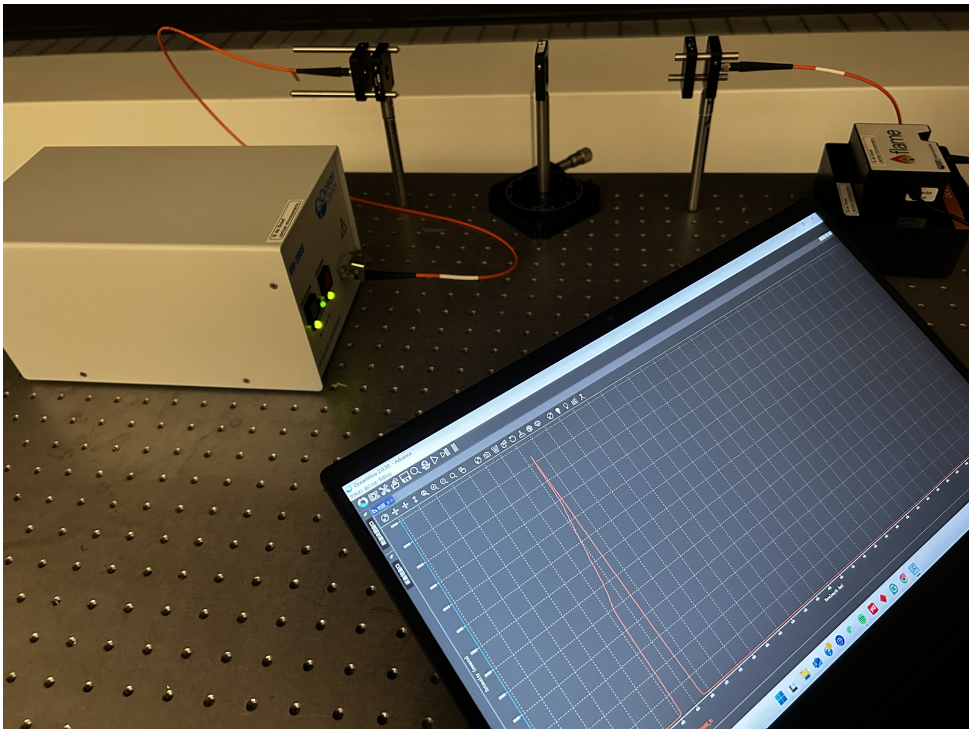

Figure 3.15: Photograph of the actual spectrometer-based measurement setup for filter.

Upconversion measurement

The schematic diagram of the spectrometer-based upconversion measurement setup is shown in Figure3.16, illustrating the optical path from the xenon lamp to the spectrometer via the condenser lens, monochromator, collimating lens, light emitter, bandpass filter, integrating sphere, and fiber optic coupling. A photograph of the actual experimental arrangement is presented in Figure3.17, showing the corresponding components in their physical configuration.

In this setup, the spectrometer was employed to evaluate the upconversion performance of the light emitter. Since the DH-2000 light source lacks sufficient power to excite upconverting nanoparticles (UCNPs), a 150 W xenon lamp was used as the excitation source. The broadband output (200–1000 nm) from the xenon lamp was spectrally filtered using a monochromator to select the desired 808 nm excitation photons. Because the xenon lamp output is highly divergent and the monochromator requires light to be focused onto its entrance slit, a condenser lens was placed between the light source and the monochromator to improve photon coupling efficiency and minimize optical losses.

The spectrally filtered beam then passed through a collimating lens before reaching the light emitter. This ensured that the excitation beam was parallel and incident perpendicular to the sample surface. UCNPs emission is non-directional, so an integrating sphere was used to collect photons emitted in all directions, maximizing the detected signal. The sphere's output port was coupled to a fiber optic, which transmitted the collected light to the spectrometer. Unlike the Fabry–Perot transmission measurements, where transmittance was calculated relative to a reference, here the results are presented in arbitrary units (a.u.) to reflect relative intensity changes. The baseline spectrum was first acquired using a blank substrate. Replacing the blank with the light emitter and observing a distinct UV peak indicated the presence of upconversion emission.

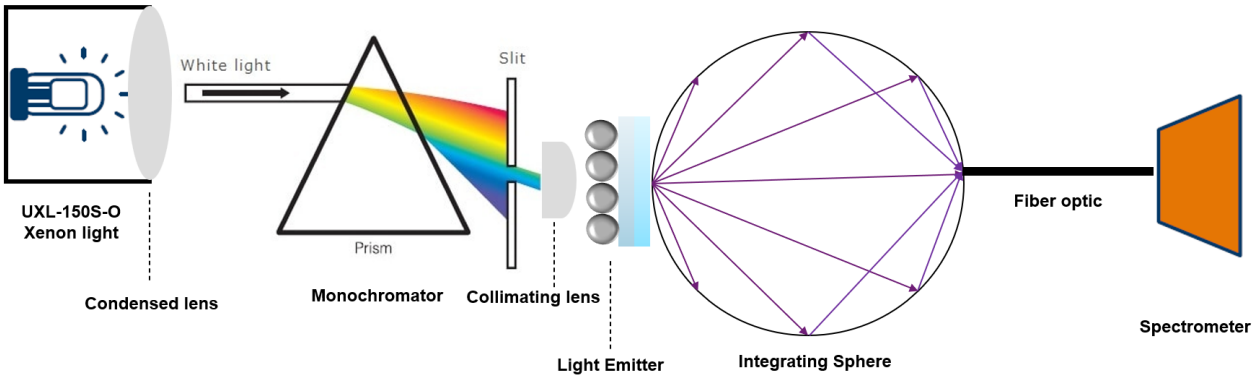

Figure 3.16: Schematic Diagram of the Spectrometer-Based upconversion Measurement Setup

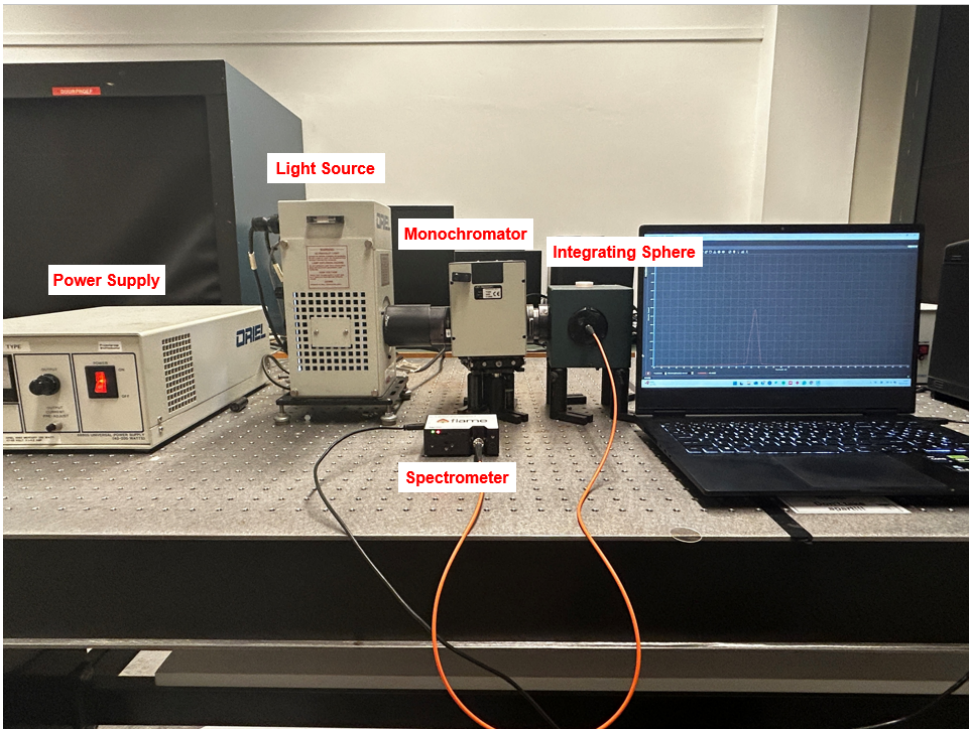

Figure 3.17: Photograph of the actual spectrometer-based measurement setup for UCNPs measurement.

Absorption measurement

The spectrometer can also be used to investigate the absorption behavior of UCNPs. This setup is identical to that used for the upconversion measurement, but the analysis focus is different. Instead of examining peaks at 360 nm and 475 nm, this measurement specifically aims to determine whether the spectrum shows a dip relative to the baseline around 808 nm, which would indicate NIR photon absorption and allow estimation of its extent.

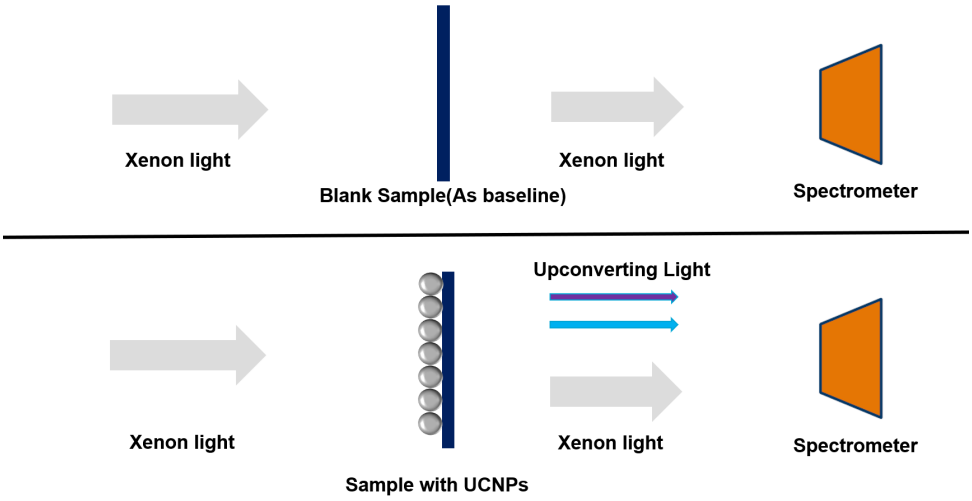

Figure 3.18: Working principle of the spectrometer for Light Emitter

3.5.2 Photodetector

Xenon light based setup

A spectrometer is effective for analyzing the spectral characteristics of optical filters and evaluating the emission profile of upconversion processes. However, these spectral plots do not directly reflect the absolute emission intensity. To accurately quantify the upconversion performance, a photodetector is employed to measure the optical power, enabling calculation of the Energy Conversion Efficiency, defined as the ratio of the upconverted emission power to the incident NIR excitation power. The system consists of two main components: a photodetector to detect optical intensity and a power meter to display the measured values. Unlike a spectrometer, a photodetector cannot resolve wavelengths—it only provides real-time total light intensity.

Figure 3.19 illustrates the schematic of the setup, which shares the same basic structure as the spectrometer-based configuration. The main difference is that, in this setup, a bandpass filter is inserted after the light emitter to selectively transmit photons within a narrowly defined wavelength range while blocking all others. These optical interference filters produce sharp transmission peaks at the target wavelength but are highly sensitive to the incidence angle. Therefore, the collimating lens placed before the light emitter is particularly important, as it helps convert the divergent beam into a parallel one, minimizing angular deviations that could otherwise shift the transmission wavelength and reduce the target photon throughput.

Two different filters were used depending on the measurement objective. The 360nm filter was employed to isolate UV emission for direct observation of the upconversion phenomenon, while the 475nm filter was used to evaluate the Fabry–Perot filter's ability to suppress blue emission and prevent unwanted spectral components from reaching the detector. For each filter, measurements were first taken with a blank substrate, followed by measurements with the UCNPs-coated sample. The difference in signal intensity between these two conditions was attributed to upconverted emission.

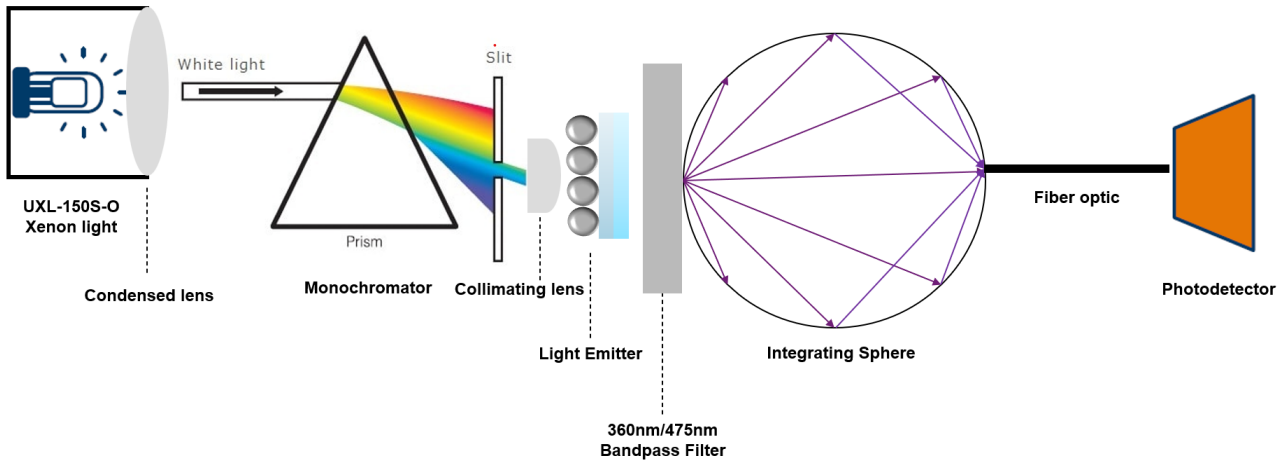

Figure 3.19: Schematic Diagram of the Photodetector-Based upconversion Measurement Setup

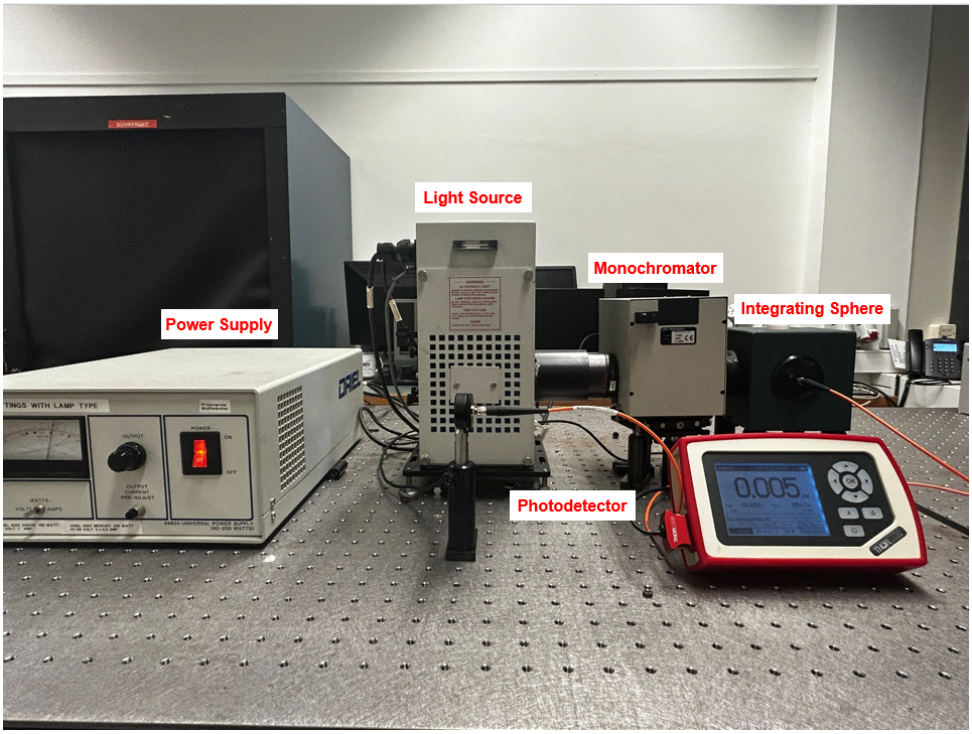

Figure 3.20: Photograph of the actual photodetector-based measurement setup for UCNPs measurement.

The setup described above represents the ideal configuration for detecting upconversion emission. In practice, however, a significant number of photons are lost as the beam travels from the xenon light source through the monochromator and integrating sphere, resulting in a reduced excitation intensity by the time the photons reach the sample. This attenuation, combined with the inherently low upconversion efficiency of UCNPs, means that the generated UV photon flux is already weak. Further losses inside the integrating sphere can reduce the signal even more, leaving only a small fraction of photons detectable by the photodetector, which severely compromises measurement accuracy. To address this, the setup shown in Figure3.21 eliminates the monochromator, integrating sphere, and fiber optics, instead placing the photodetector, sample, and bandpass filter directly in front of the light source. This configuration ensures that the UCNPs receive the maximum possible excitation energy.

Figure 3.21: Updated photodetector setup with the detector placed directly in front of the light source. The sample and filter are mounted onto the detector for accurate intensity measurement.

However, this measurement approach still introduces considerable inaccuracies. The xenon source emits a broadband spectrum, and the UCNPs may absorb multiple wavelengths beyond the target 808nm excitation, making it difficult to identify which specific wavelength is responsible for the upconversion. Moreover, the photodetector cannot isolate the 808nm component from the broadband excitation, preventing accurate determination of the absorbed excitation power. As upconversion emission is inherently weak, the measured signal difference between the sample and the blank can also be affected by various background factors and noise.

Laser diode based Setup

Figure3.23 shows the experimental arrangement of the laser diode system. To eliminate interference from ambient light, the entire setup was enclosed in a light-tight box. The laser diode system consists of an external temperature and current controller connected to a laser diode adapter inside the enclosure. Because the laser diode output is highly divergent, a collimating lens was placed at the output to produce a parallel beam. After passing through the sample and the bandpass filter, only photons within the target wavelength range were transmitted. A subsequent focusing lens directed the filtered beam onto the photodetector for power measurement.

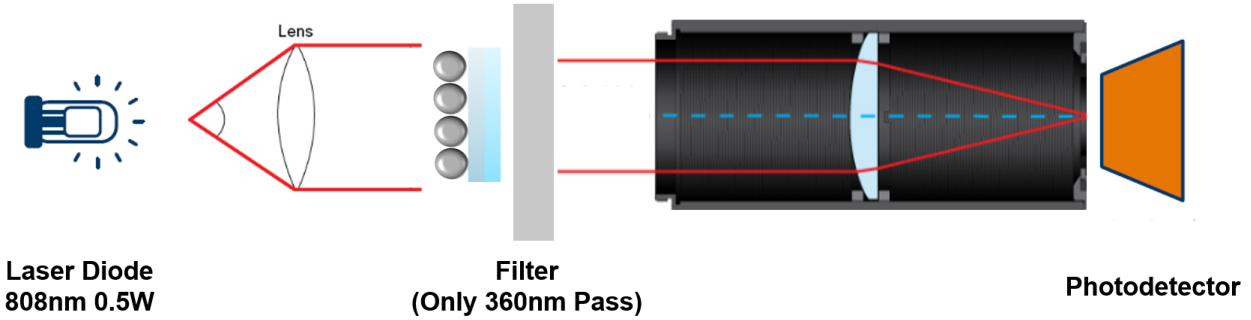

Figure 3.22: Schematic Diagram of the Photodetector-Based upconversion Measurement Setup by laser diode

Figure 3.23: Left: Laser diode setup enclosed in a light-tight box to prevent ambient light interference. Right: Power measurement of the laser diode output using a photodetector.

Since NIR photons are invisible to the human eye, an NIR detector card was used to convert the infrared light into visible red light. When the laser diode was operated without any optical elements, Figure3.24 shows that the output beam was highly divergent. Due to the asymmetric transverse and longitudinal mode profiles, the divergence angle was much larger along the x-axis than along the y-axis. This large divergence significantly reduces the optical intensity per unit area.

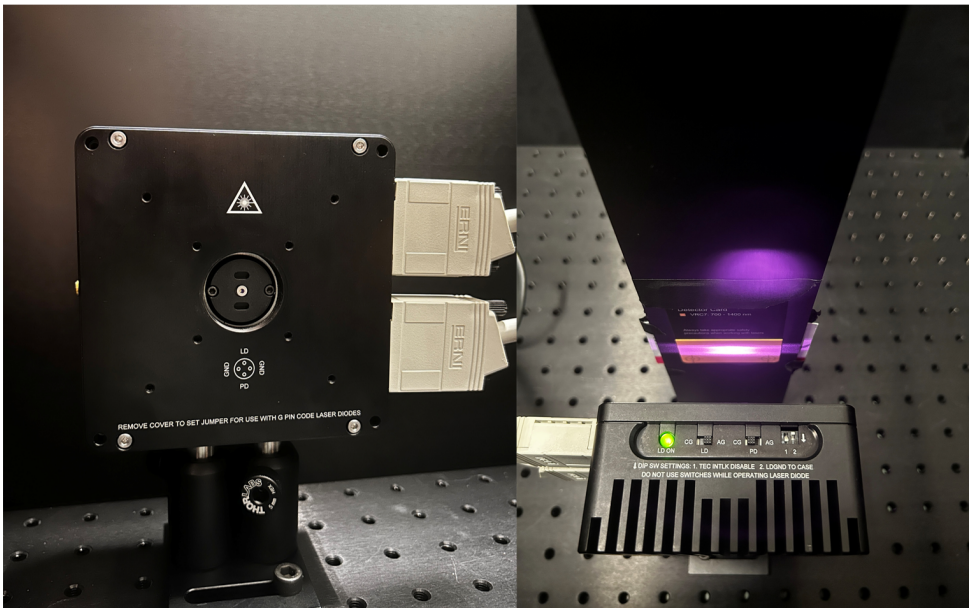

Figure 3.24: Raw laser diode structure and its light spot.

After introducing a collimating lens, the beam was noticeably more concentrated compared to Figure3.25, forming an elliptical spot. This is because the collimating lens converted the divergent beam into an approximately parallel beam. However, since the divergence angles along the two axes were different, the lens applied the same correction in both directions, resulting in an elliptical rather than circular profile.

Figure 3.25: Collimating lens with laser diode structure and its light spot.

Finally, after adding a focusing lens, the beam was tightly focused into a small spot(Figure3.26). By calculating the area of the focal point, the final spot size was determined to be 0.785 cm².

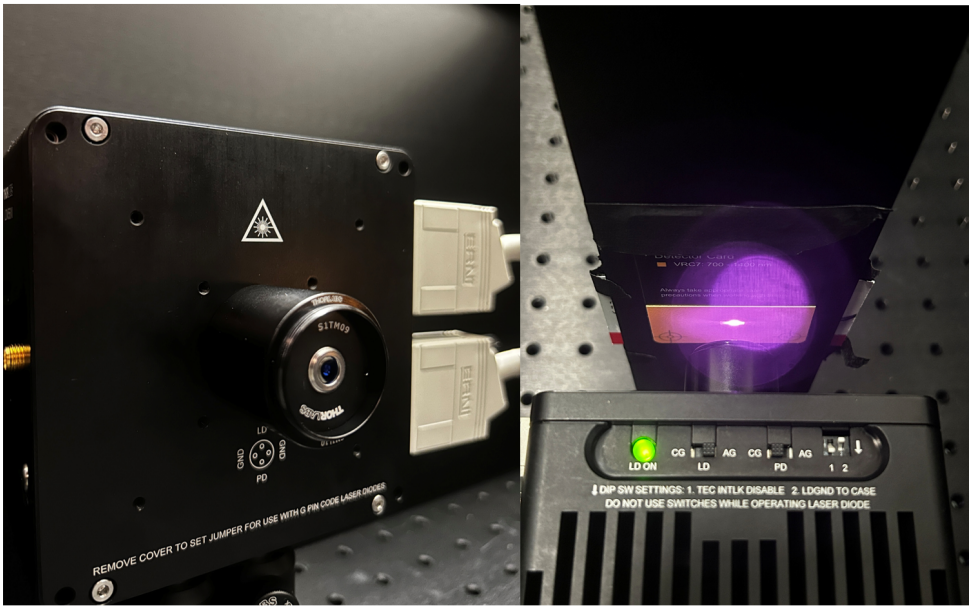

Figure 3.26: Focusing lens with laser diode structure and its light spot.

The excitation and emission powers measured under monochromatic excitation were used to calculate the external energy conversion efficiency (ECE), defined as the ratio of the emitted UV power to the incident 808nm excitation power at the sample:

$$\eta_{\mathrm{ECE}} = \frac{P_{\mathrm{em}}}{P_{\mathrm{ex}}} \tag{3.8}$$

Here, P_{ex} was measured directly at the sample plane without the use of optical filters, while P_{em} was obtained under the 360 nm bandpass filter condition as the difference in detected power between the UCNPs-coated sample and the blank substrate, thereby isolating the upconverted emission. In addition to ECE, the photoluminescence quantum yield (PLQY) was determined to quantify the photon yield. PLQY is defined as the number of photons emitted at 360 nm per photon absorbed at 808 nm:

$$\mathrm{PLQY} = \frac{\text{Number of emitted photons}}{\text{Number of absorbed photons}} = \frac{P_{\mathrm{em}} \cdot \lambda_{\mathrm{em}}}{P_{\mathrm{abs}} \cdot \lambda_{\mathrm{ex}}} \tag{3.9}$$

Both the absorbed and emitted photon numbers were derived from the optical powers measured by the photodetector and converted to photon numbers using (N=$\frac{P\lambda}{hc}$). This approach ensures consistency between the ECE and PLQY calculations, while clearly distinguishing between energy-based and photon-based metrics.

Chapter 4

Experiments and Results

4.1 Upconverting nanoparticles

The upconverting nanoparticles used in this experiment are $NaYF_4$:Yb,Tm,Nd @ $NaYF_4$:Yb,Nd at a concentration of 10mg/mL, dispersed in deionized water. As described in the previous section, the fabrication process removes the hydrophobic ligand (e.g. oleic acid) but does not introduce any hydrophilic ligand. As a result, the nanoparticles can temporarily disperse in aqueous solution but tend to aggregate over time, as shown in Figure4.1.

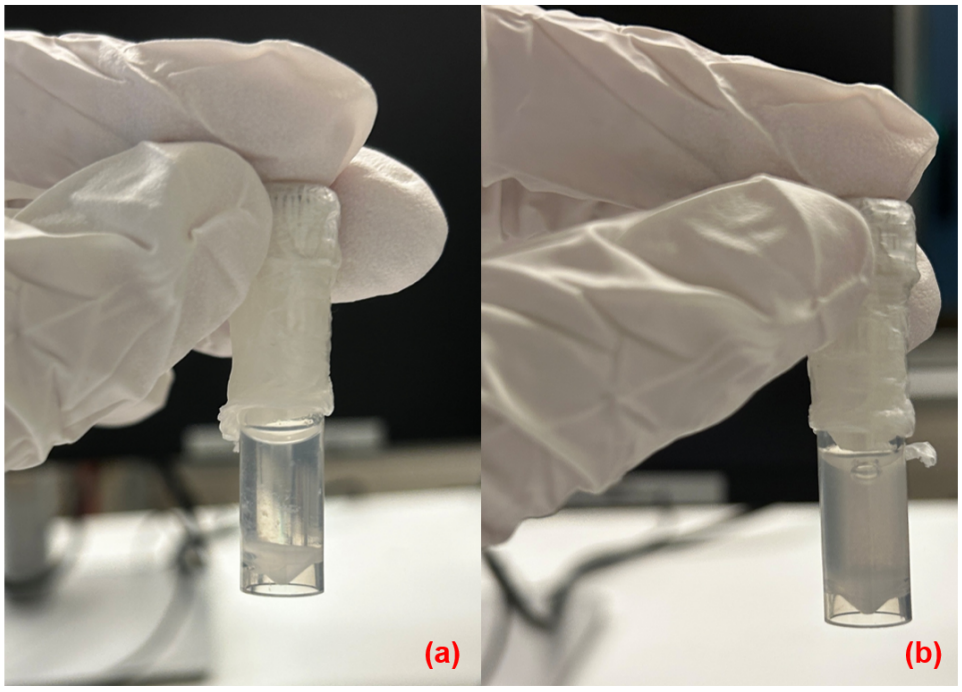

Figure 4.1: (a) The particles precipitate before the treatment. (b) The particles separate in the solution under ultrasonication and vortex mixing.

After 10 minutes of ultrasonication followed by 10 minutes of vortex mixing, the particles appear temporarily dispersed. However, they gradually precipitate to the bottom of the container within a short time frame. During this limited dispersion window, the solution was aliquoted into several samples with different concentrations: 0.5mg/mL, 2mg/mL, 5mg/mL, and 10mg/mL.

Before the coating process, the substrate was treated in a Diener Atto Plasma Reactor for 10 min. This oxygen plasma treatment activates the substrate surface, thereby improving the adhesion between

the nanoparticles and the substrate. Following the surface treatment, nanoparticle solutions with different concentrations were prepared for coating tests. The preparation details for each concentration are summarized in Table 4.2. For the drop-casting method, the nanoparticle solution was directly dispensed onto the wafer surface, followed by annealing at 100°C for 10min. For spin coating, the solution was applied at 1000rpm for 2min and subsequently annealed under the same conditions.

	Drop Casting 1	Drop Casting 2	Drop Casting 3	Spin Coating 1	Spin Coating 2	Spin Coating 3
0.5mg/mL	100°C 0.05mL			1000rpm 2min 100°C 0.05mL		
5mg/mL		100°C 0.05mL			1000rpm 2min 100°C 0.05mL	
2mg/mL			100°C 0.05mL			1000rpm 2min 100°C 0.05mL

Figure 4.2: (a) The particles precipitate before the treatment. (b) The particles separate in the solution under ultrasonication and vortex mixing.

Figure4.3 compares two samples prepared using 5mg spin coating and drop casting, respectively. When placed under illumination, neither sample exhibited visible luminescence to the naked eye. In the drop-casted sample, a pronounced coffee-ring effect was observed, caused by the non-uniform evaporation of the solvent. As the solvent dries, the solutes are driven to the edges, forming a ring-like deposit structure.

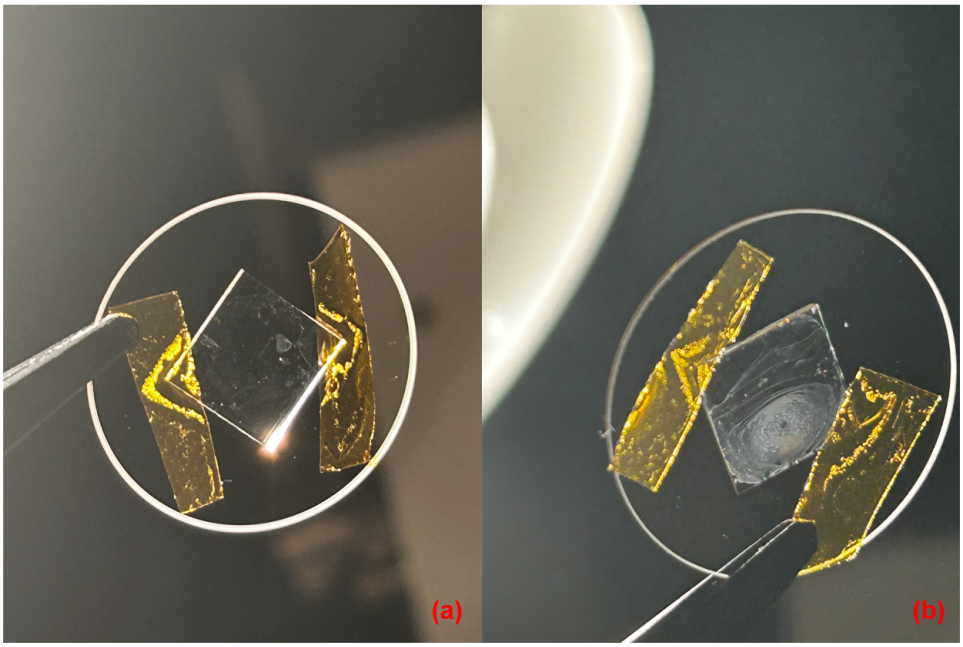

Figure 4.3: (a) The sample by spin coating (b) The sample by drop casting.

4.2 Fabry-Perot Filter

Since the deposition of silicon nitride strongly depends on the ratio of precursor gases, only specific gas ratios can reliably form the Si_3N_4 phase. To avoid ambiguity in this section, the silicon nitride layer is hereafter referred to as "SiN". In the Figure3.7, we have already discussed the structure of the Fabry–Perot filter. During fabrication, the first step is to calibrate the deposition rate using an ellipsometer to minimize thickness errors. Since ellipsometry relies on light reflection, a silicon wafer is used as the calibration substrate to ensure accurate measurements.

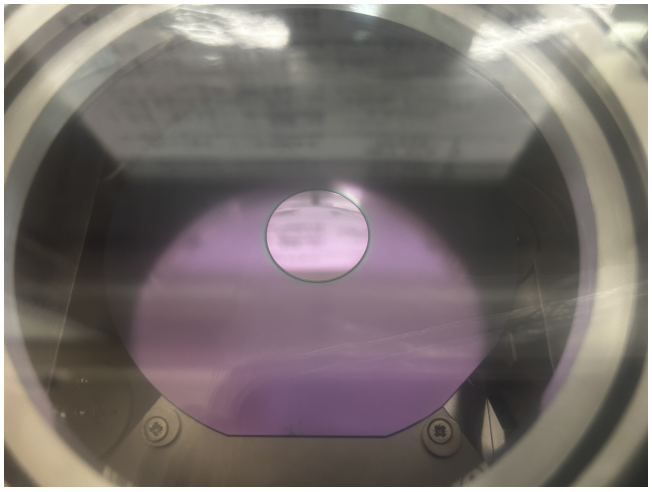

Figure 4.4: The Fabry-Perot Filter depoite on the SiO2 substrate

The deposition rates are approximately x nm/min for SiO_2 and y nm/min for SiN. These rates may vary slightly due to machine conditions but typically remain within a predictable range. Figure4.4 shows the fabricated Fabry–Perot filter deposited at 150°C. When tested with a spectrometer, the transmission curve is shown in Figure4.5 (a). Compared with the simulation in Figure4.5 (b), the curve above 400nm aligns well, but a slight shift is observed, likely due to fabrication error, which can be optimized. However, in the UV region (<400nm), the transmission drops significantly, deviating from simulation expectations.

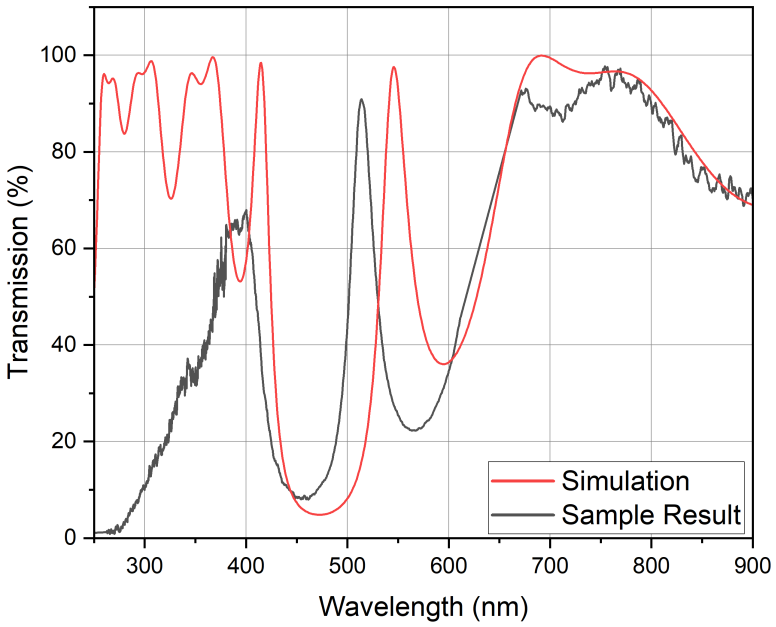

Figure 4.5: The result of the Fabry-Perot Filter(Black Curve) comparing with the simulation(Red Curve).

Several factors could contribute to this UV suppression:

- Deposition Conditions: ICPCVD sequentially deposits alternating layers. Residual gases between deposition steps may form interfacial impurities, especially between SiO_2 and SiN that absorb UV photons.
- Intrinsic Absorption: The density and surface roughness of the layers affect UV transmission. As the surface roughness approaches the wavelength scale, significant scattering can occur, especially for shorter wavelengths.
- Defect States: ICPCVD uses SiH_4 and N_2 as precursor gases to form SiN. It is inevitable that bonds like Si–H and N–H form, introducing defects that increase absorption, particularly in the UV regime.

To isolate the dominant factor, a single SiN layer (60nm thick) was deposited and measured. As shown in Figure4.6, even this single layer showed poor UV performance, indicating that interfacial impurities were not the sole cause, thereby excluding intrinsic absorption as the primary factor.

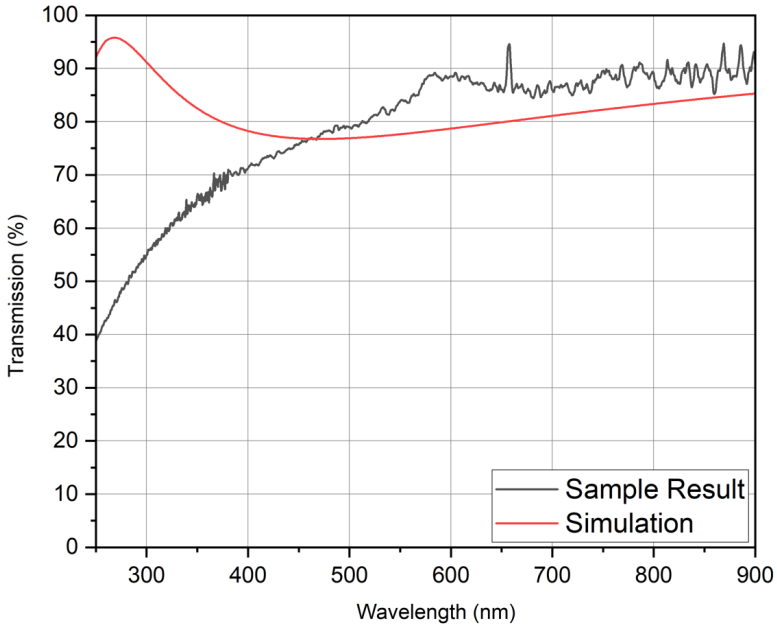

Figure 4.6: The result of the single layer of the SiN compare with the simulation

Next, high-temperature deposition (up to 350°C) was attempted to improve film density and reduce defects. However, Figure4.7 shows the transmission still deviated from simulation, suggesting that high temperature alone does not resolve UV suppression.

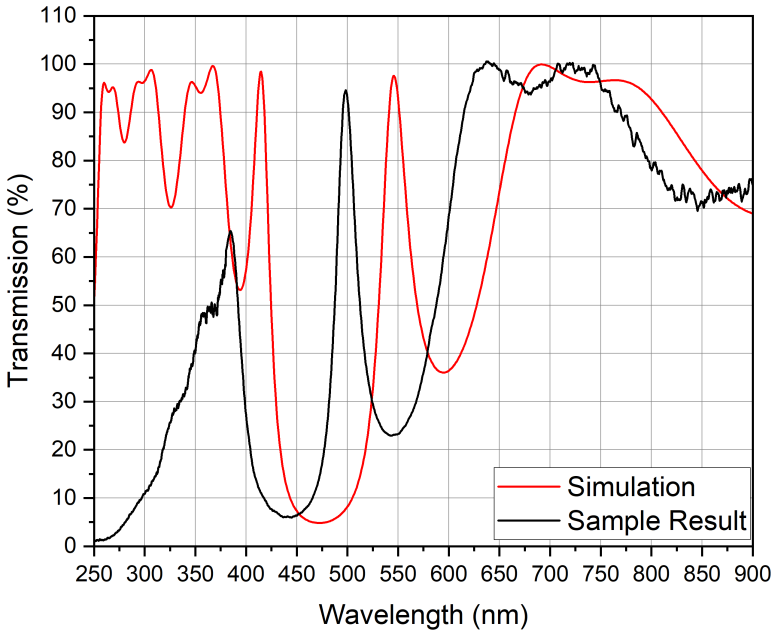

Figure 4.7: The result of the Fabry-Perot Filter fabricate under the 350°C compare with the simulation

This indicates that defect formation is the dominant limiting factor. Literature reports show that adjusting the precursor gas ratio can significantly reduce defect-related absorption. As shown in Figure4.8 and Figure4.9, four gas recipes were tested. The nitrogen-rich (N-rich) recipe exhibited the lowest optical absorption across relevant factors, indicating better transparency in the UV[47].

Wafer type	Recipe	Φ_{SiH4} [sccm]	R_g
A	Slightly Si-Rich	96	0.149
B	Stoichiometric	84	0.132
C	Slightly N-rich	70	0.113
D	N-rich	45	0.076

Figure 4.8: The recipe of four different wafer
[47]

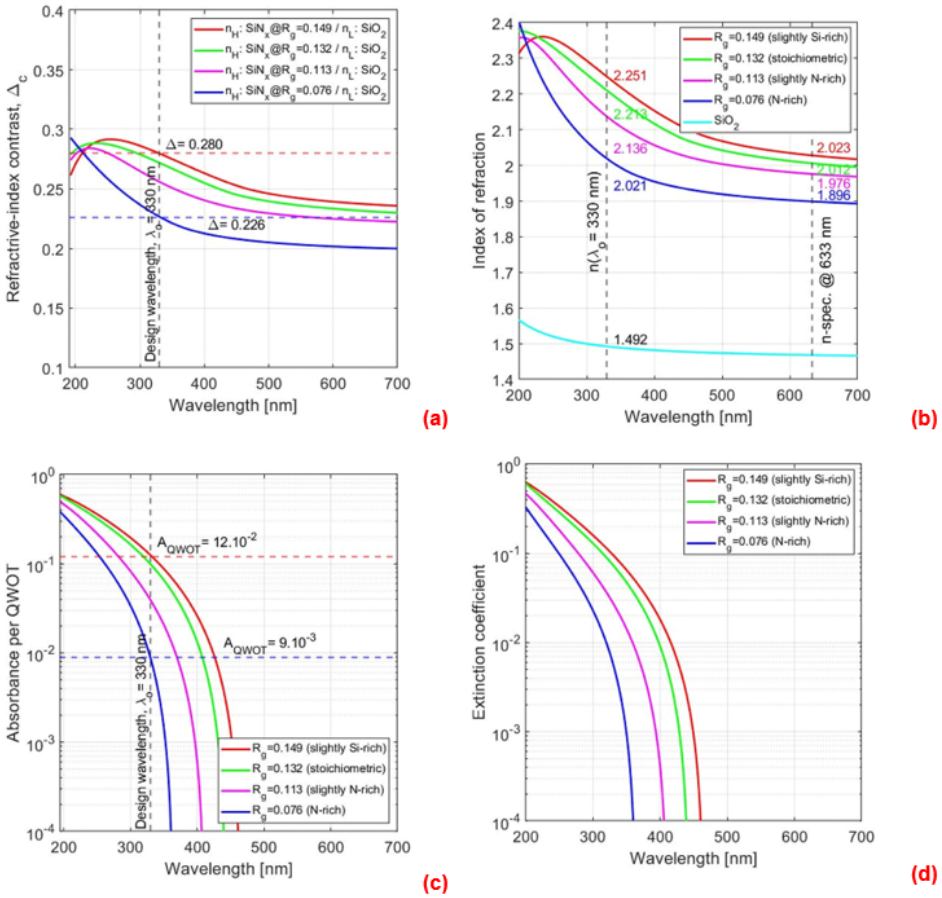

Figure 4.9: (a) Refractive-index contrast: Difference between the high-index and low-index materials.The higher value represent the stronger reflectivity. (b) Index of refraction: The ratio of the speed of light in vacuum to that in the material. (c) Absorption per QWOT(Quarter-Wavelength Optical Thickness): The amount of optical absorption normalized by a layer. (d) Extinction coefficient: How strongly the material absorbs light.
[47]

$$R_g = 0.076 = \frac{\phi_{SiH_4}}{\phi_{SiH_4} + \phi_{N_2}} \tag{4.1}$$

SiH_4	4sccm
N_2	50sccm

By adopting this N-rich recipe, with SiH_4:N_2 = 4:50 sccm as shown in Equation4.1, the UV transmission curve aligned with simulation results as shown in Figure4.10, confirming improved filter performance.

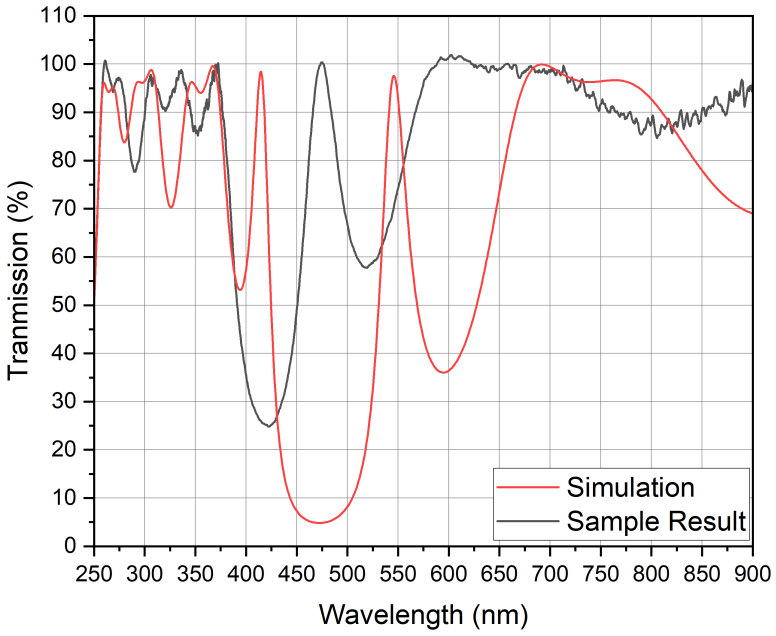

Figure 4.10: The result of the nitrogen-rich recipe Fabry-Perot Filter compare with the simulation

However, a slight spectral shift still remained. As discussed in Section 3.2.3, globally increasing the layer thickness can red-shift the transmission band. The Figure4.11 illustrates the spectral shift of 15% under different deposition temperatures. Compared with the initial curve, the shifted Fabry–Perot filter exhibits low transmittance at 475nm and high transmittance at 360nm in both temperature conditions. Specifically, at 150°C, the transmittance at 360nm reaches 96.00%, while that at 475nm is 28.70%, yielding a ratio of 3.48. At 350°C, the transmittance at 360nm is 96.67%, whereas that at 475nm is 22.64%, corresponding to a ratio of 4.27. Although these values still deviate from the ideal case predicted by COMSOL simulations, the results—considering fabrication and measurement imperfections—demonstrate that the filter effectively facilitates photon transmission at 360nm while suppressing those at 475nm. Moreover, the superior performance observed at 350°C suggests that higher deposition temperatures lead to films of improved quality, thereby enhancing optical selectivity.

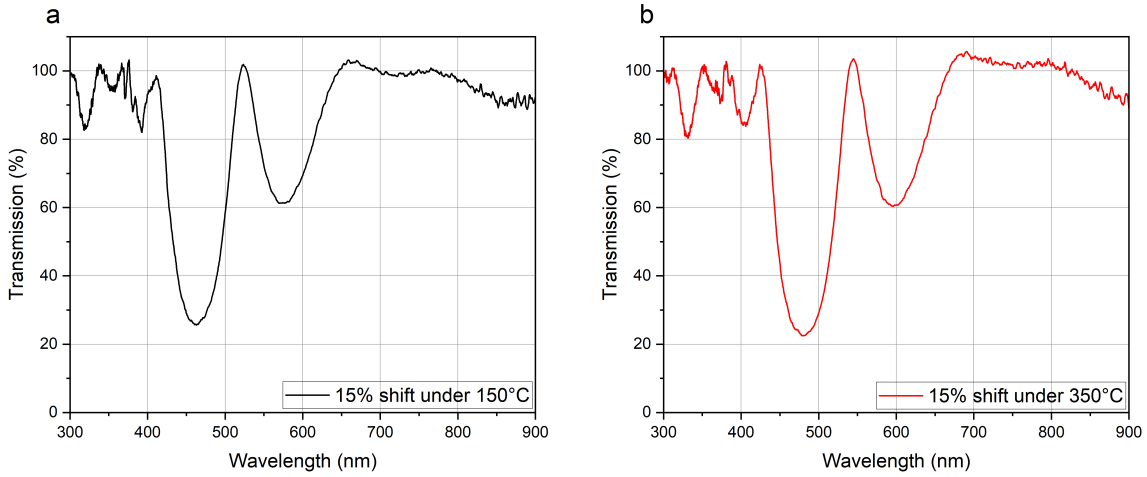

Figure 4.11: Based on the previously optimized recipe, the Fabry–Perot filter was fabricated with a 15% increase in layer thickness to induce a red shift and achieve the target spectral position. Two samples were prepared under different deposition conditions: (a) deposition at 150°C and (b) deposition at 350°C.

4.3 Material Characterization

4.3.1 Morphological characterization

Since the diameter of the upconverting nanoparticles is approximately 30nm, direct observation is challenging. However, their surface morphology can be visualized using scanning electron microscopy (SEM). Figure4.12 shows a 5mg/mL nanoparticle solution spin-coated at 2500rpm. The result indicates a sparse distribution of nanoparticles, implying low adhesion between the particles and the substrate under high spinning rates.

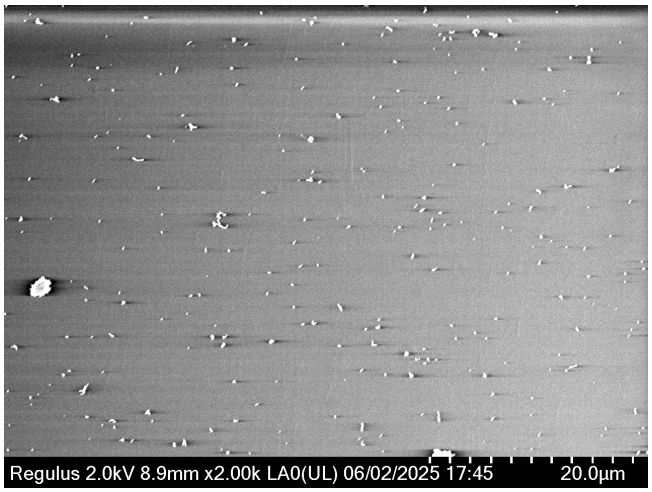

Figure 4.12: SEM image of UCNPs (5 mg/mL) spin-coated at 2500 rpm for 1 min, captured at 2500× magnification.

Figure4.13 shows samples prepared at 2mg/mL and 0.5mg/mL concentrations, both spin-coated at 1000rpm. The lower spinning speed allows more retention, but due to the lower initial concentration,

very few particles remain on the surface, indicating that most particles are lost during the spin-coating process.

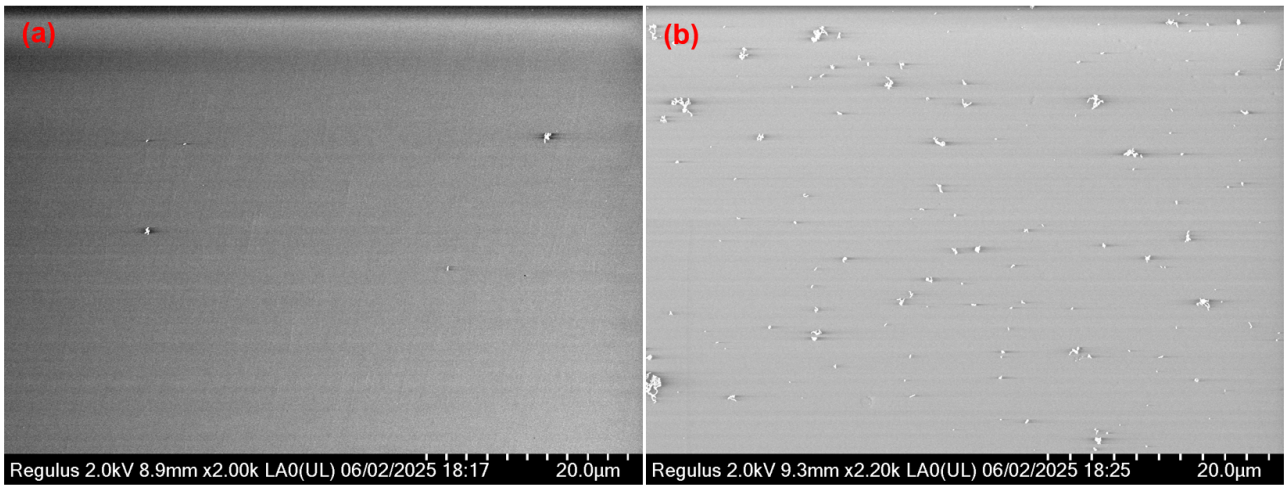

Figure 4.13: SEM images of UCNPs deposited by spin coating at different concentrations and 2000× magnification: (a) 0.5 mg/mL; (b) 2 mg/mL. The particle density increase significantly with higher concentration.

To improve particle retention, a 5mg/mL solution was spin-coated at 1000rpm for 1 minute. Figure4.14 demonstrates that a lower spinning speed combined with a higher concentration leads to greater particle attachment, although adhesion is still insufficient for dense coverage.

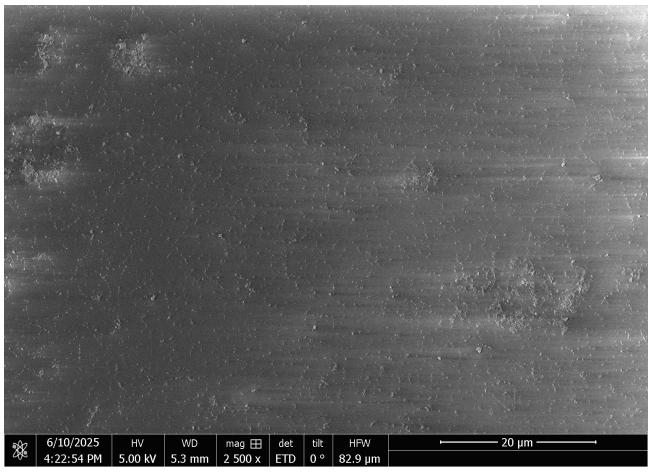

Figure 4.14: SEM image of UCNPs (5 mg/mL) spin-coated at 1000 rpm for 1 min, captured at 2500× magnification.

To further enhance surface coverage, drop casting was employed using the same 5mg/mL solution. This method minimizes centrifugal loss, allowing more nanoparticles to remain on the substrate. Figure4.15 presents the drop-cast sample observed under optical microscopy (OM). While the resolution of OM is insufficient to resolve individual nanoparticles, a clear boundary between the coated and uncoated regions confirms high surface coverage.

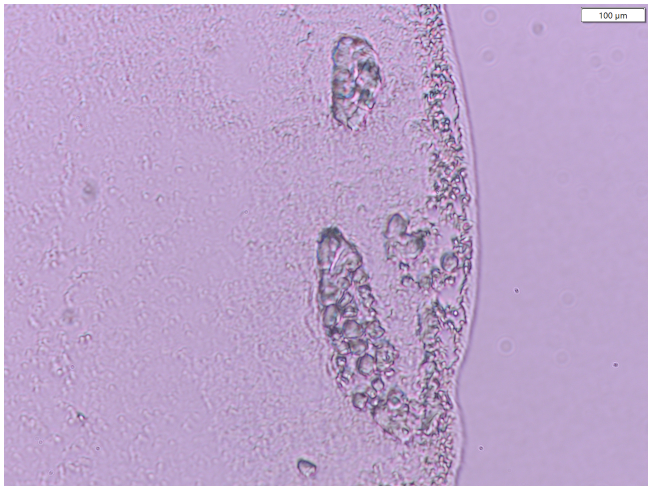

Figure 4.15: Optical microscopy image of UCNPs (5 mg/mL) deposited by drop-casting.

Under SEM (Figure4.16), particle aggregation is observed in localized areas, while the remaining regions exhibit a uniform dispersion of nanoparticles. Compared to spin-coated samples under high magnification, the drop-cast sample displays a significantly higher nanoparticle density in Figure4.17.

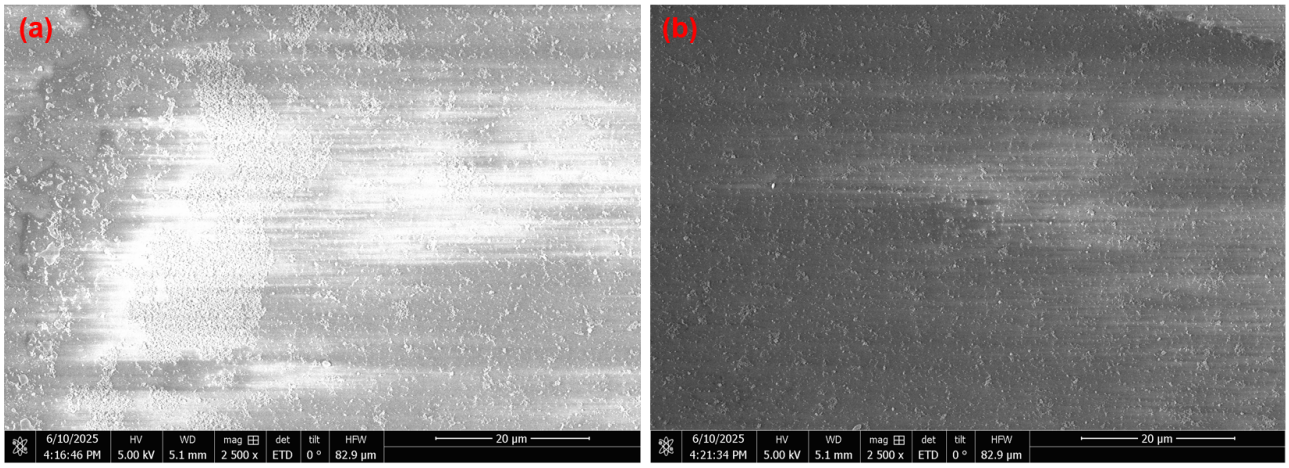

Figure 4.16: SEM images of UCNPs (5 mg/mL) deposited by drop-casting at 2500× magnification: (a) dense aggregation area; (b) relatively uniform region with reduced particle overlap.

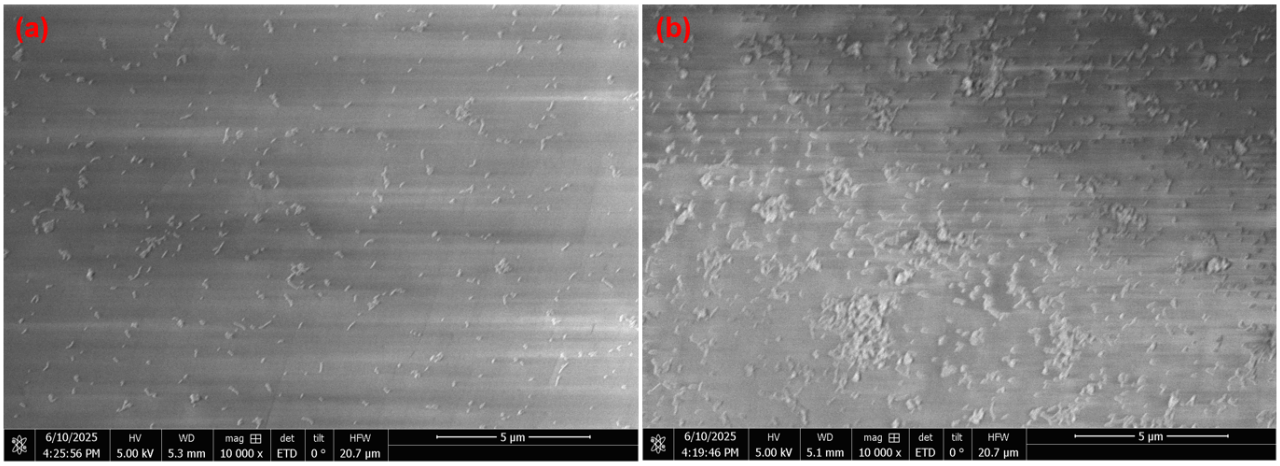

Figure 4.17: SEM images of UCNPs (5 mg/mL) deposited on wafers at 10,000× magnification: (a) spin-coated at 1000 rpm for 1 min, (b) drop-cast.

However, due to the insulating nature of the sample, SEM imaging initially suffered from charging effects, complicating analysis. To mitigate this, a 15nm gold layer was sputtered onto the surface to improve conductivity and facilitate electron escape. Nevertheless, the sputtering process mechanically disturbed the loosely adhered nanoparticles, causing partial particle detachment, thereby hindering observation.

To prevent particle loss during imaging, a copper tape was applied around the sample (Figure4.18). The white ring structure observed is a typical coffee-ring pattern resulting from drop casting. When imaging near the copper tape, the electrons can dissipate through the conductive tape, thus reducing charging effects and enabling high-quality SEM imaging.

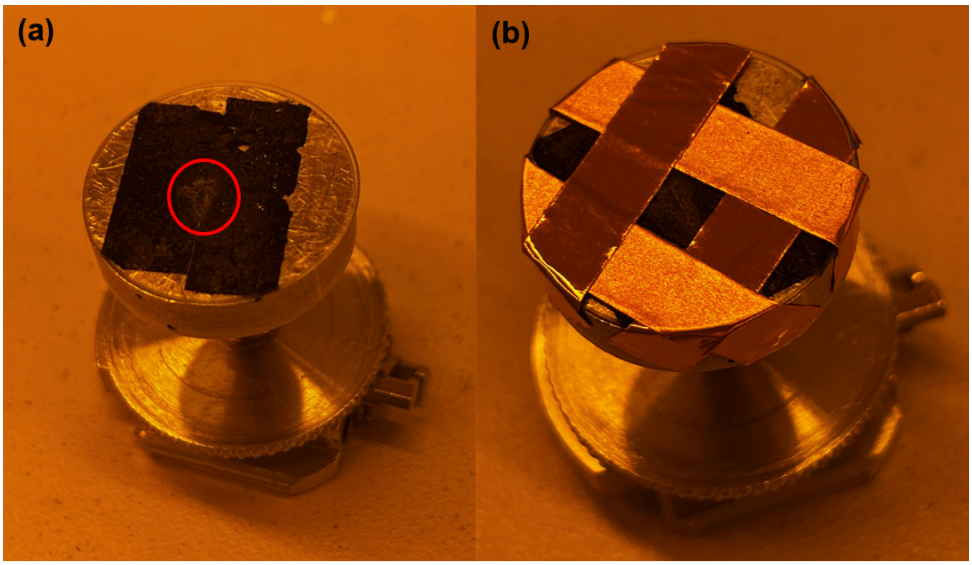

Figure 4.18: Photographs of sample mounting for SEM analysis. (a) The coffee-ring structure (highlighted by the red circle) is selected as the observation region. (b) Copper tape is applied to cover the sample while exposing the coffee-ring edge, allowing charge dissipation and minimizing charging artifacts during SEM imaging.

SEM observation reveals that the drop-cast sample exhibits two distinct regions. One region shows a dense distribution of nanoparticles across the surface with minimal aggregation (Figure4.19 (a)),

whereas the other remains sparsely coated due to the inherent non-uniformity of the drop-casting process. In these sparse areas, exposed SiO substrate is clearly visible, with only minimal nanoparticle presence.

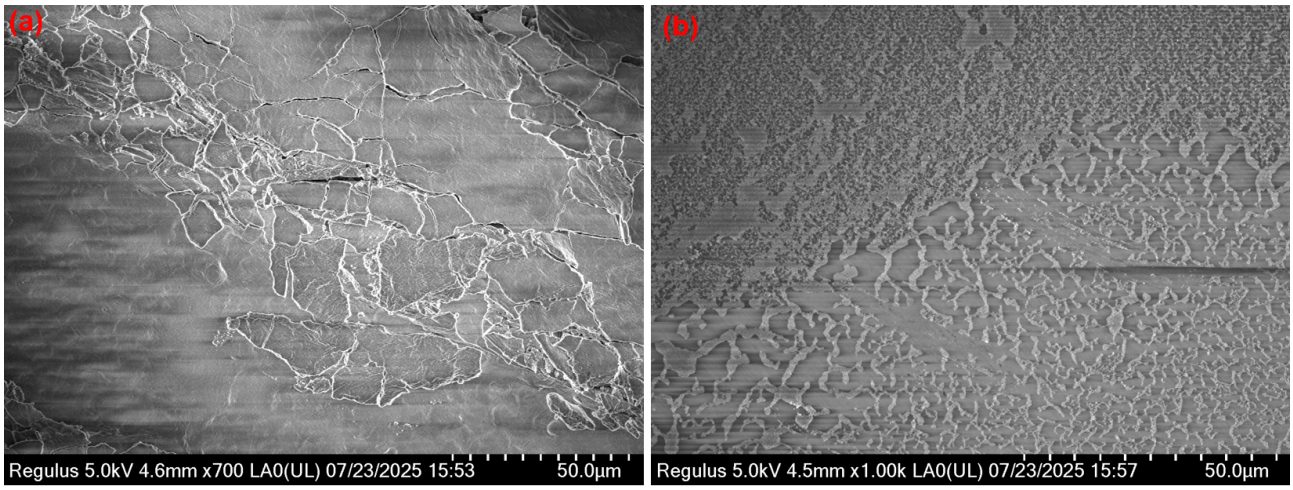

Figure 4.19: SEM images showing the dense and sparse regions of UCNPs (5mg/mL) deposited by drop-casting. (a) Densely coated region with high nanoparticle coverage and minimal aggregation (captured at 1000×). (b) Sparsely coated region with exposed SiO_2 substrate due to the inherent non-uniformity of drop casting (captured at 700×). Both images show the same field width of 50m, as indicated by the scale bars.

High-magnification imaging(Figure4.20) of the densely coated area confirms that the nanoparticles have an average diameter of approximately 30nm, consistent with the manufacturer's specifications.

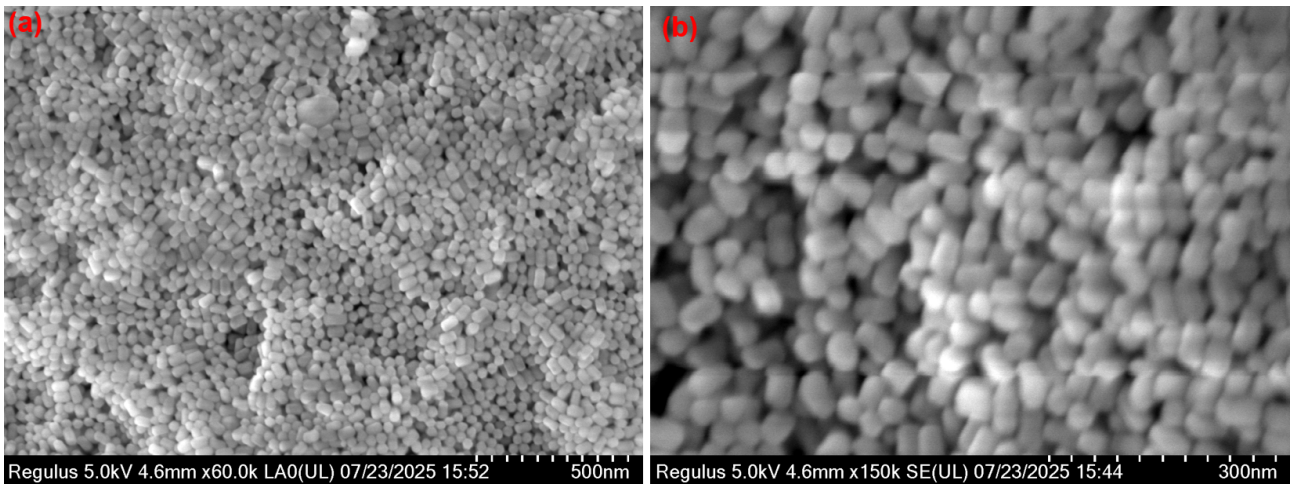

Figure 4.20: High-magnification SEM images of the densely coated region from drop-casted UCNPs (5mg/mL). (a) Overview of the nanoparticle-packed surface at 60,000× magnification. (b) Further magnified view at 150,000×; comparison with the scale bar confirms that the average particle size is approximately 30nm, consistent with the manufacturer's specifications.

Figure4.20 already shows clear observation of the nanoparticle morphology. However, in areas where the particles do not fully cover the substrate, the image quality(Figure4.21) significantly deteriorates. This suggests that a continuous nanoparticle layer may act as a "buffer structure" for charge

dissipation, with interstitial gaps between particles facilitating localized electron movement, thereby allowing charges to escape. In contrast, regions of bare SiO_2 expose a smooth surface that promotes charge accumulation, exacerbating charging effects.

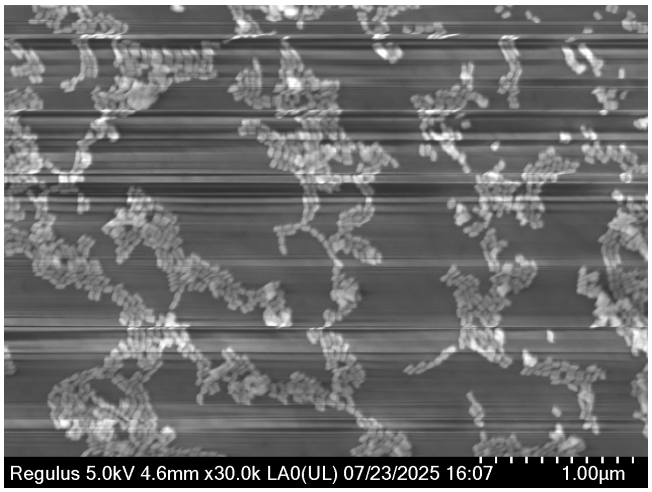

Figure 4.21: In regions where the nanoparticles are only partially distributed, the exposed substrate contributes to poor image quality.

Finally, to estimate the film thickness, atomic force microscopy (AFM) was used over a $10\mu m \times 10\mu m$ scan area. Due to the intrinsic non-uniformity of the drop-casting process, the nanoparticles cannot be evenly distributed across the substrate, resulting in distinctly different morphologies for each prepared sample. Therefore, the region with the highest particle aggregation—corresponding to the most densely packed white precipitate—was selected for observation in order to compare the thickness between sparsely coated and fully coated areas.

Figure4.22 presents the two-dimensional AFM topography of the region with the highest particle density, revealing a highly uneven surface profile. A pronounced peak is observed at the center, whereas the thickness gradually decreases toward the edges. Figure4.23 shows the corresponding three-dimensional AFM rendering, illustrating the pronounced height variation. The maximum thickness in the central region reaches $1.06\mu m$, which, given an individual nanoparticle diameter of approximately $30nm$, corresponds to roughly 35 stacked layers. This finding confirms that a sufficient quantity of nanoparticles is deposited on the substrate surface.

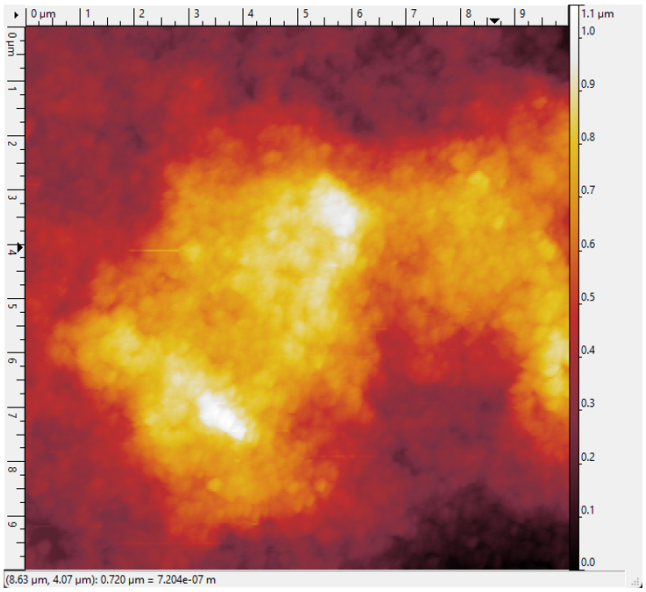

Figure 4.22: Two-dimensional AFM topography of the region with the highest particle density.

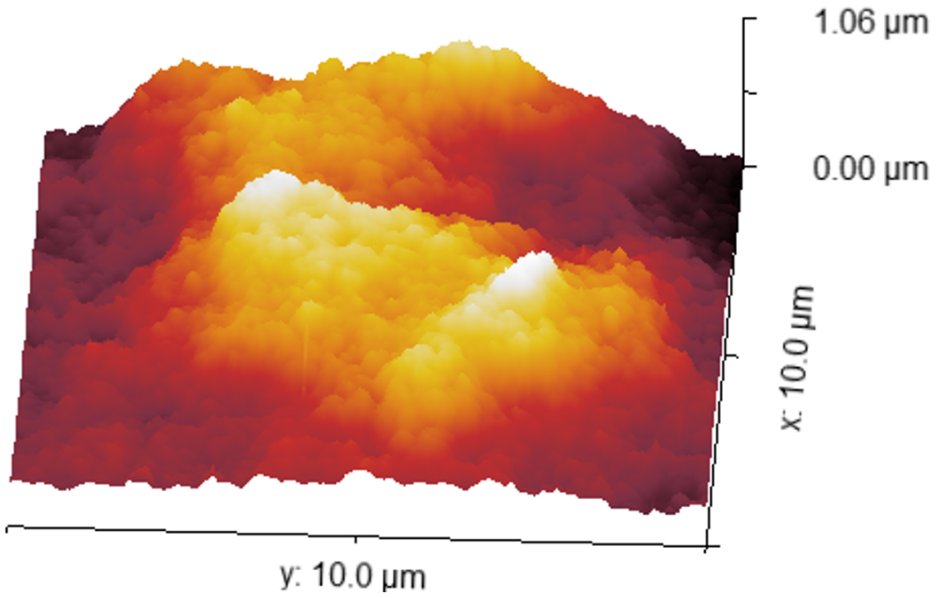

Figure 4.23: Three-dimensional AFM topography of the region with the highest particle density.

4.3.2 Optical characterization

The optical characterization aims to evaluate the luminescence behavior of the nanoparticles after coating them onto the substrate. Under light illumination, observable luminescence from UCNPs indicates successful excitation. According to the manufacturer's guideline, a light intensity above 0.5W is required to achieve effective excitation.

However, in the current optical setup, although the Xenon lamp has a nominal electrical input of 150W, the actual optical intensity at 808nm is not directly measurable. Significant photon loss occurs throughout the optical path—including the monochromator, integrating sphere, and optical fiber—before reaching the photodetector. As shown in the following Chart4.1, the final detected

power is only 0.1nW, far below the required excitation threshold. Even when a condenser lens is used to concentrate the light, the improvement in intensity is minimal. Therefore, to ensure sufficient excitation of the UCNPs, the sample must be positioned directly in front of the light source, bypassing all intermediate optical components as shown in Figure3.21.

Power Supply	Light Source	Monochromator	Integrating Sphere	Condenser lens	Power Density
✓	✓	✓	✓	✗	0.1nW
✓	✓	✓	✓	✓	0.2nW
✓	✓	✓	✗	✗	4.5nW
✓	✓	✓	✗	✓	10.2nW
✓	✓	✗	✗	✗	Too High

Table 4.1: Power density under different optical configurations

To further investigate the significant photon loss suspected in the self-built setup, the same UCNPs-coated sample was examined using a commercial spectrofluorometer (FLS980, Edinburgh Instruments). The optical configuration of the FLS980 is largely equivalent to that of the custom-built system, comprising a monochromator, integrating sphere, detector, and identical optical path geometry. The primary distinction lies in the excitation source: the custom system employs a 150W xenon lamp, whereas the FLS980 is equipped with a 350W xenon lamp. Despite the higher nominal source power, the emission spectrum acquired with the FLS980 in the 300–500nm range did not exhibit a discernible upconversion emission peak under 808nm excitation shown in Figure. Direct measurement of the excitation power at the sample plane using a photodetector yielded only 0.07mW at 808nm, indicating that insufficient excitation intensity is the most probable cause of the absence of detectable upconversion emission in both measurement systems.

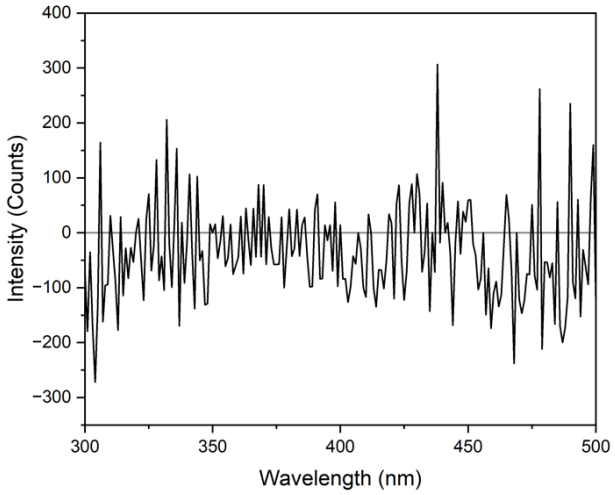

Figure 4.24: The emission spectrum in the 300–500 nm range under 808 nm excitation measured using the FLS980 spectrofluorometer

Figure4.25 presents the emission spectra of the blank substrate (red) and the UCNPs-coated sample (black) recorded using two spectrometers. The left panel covers the short-wavelength range (200–400nm), while the right panel covers the longer-wavelength range (400–1100nm). The spectral differences between the two samples were further analyzed by subtracting the blank spectrum from

the UCNPs-coated spectrum, as shown in Figure4.26. The resulting differential spectrum exhibits distinct emission peaks in the 300–350nm and 400–500nm regions, corresponding to characteristic upconversion emissions at approximately 360nm and 475nm, respectively, as reported in the literature[44]. Although the optical setup limits the spectral resolution, the observed peaks confirm that the UCNPs produce strong upconversion luminescence under high-intensity excitation.

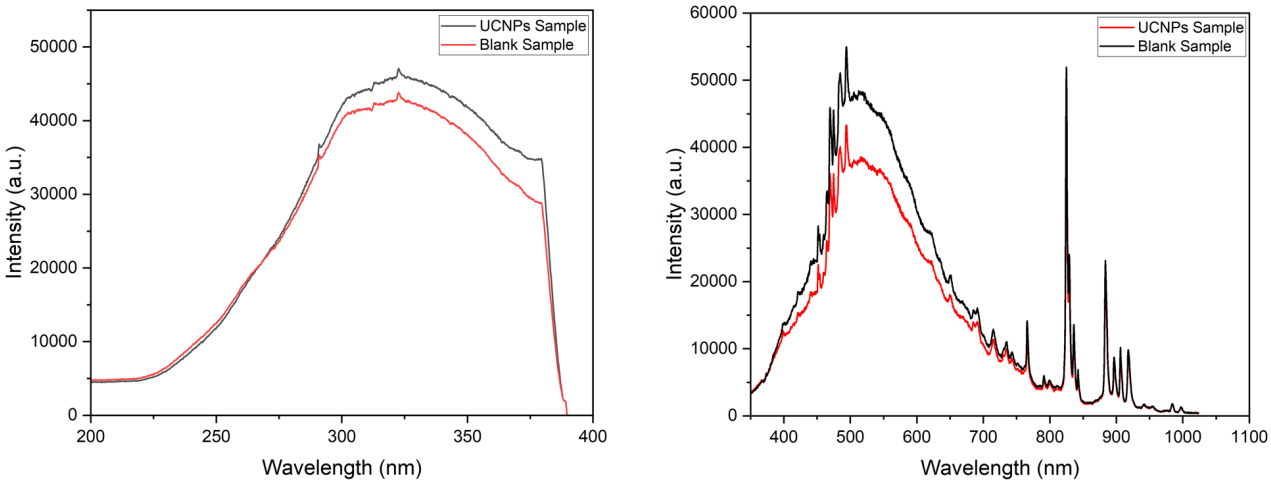

Figure 4.25: Spectral intensity measured using two spectrometers under identical conditions. The black curve represents the signal from the sample coated with upconversion nanoparticles (UCNPs), while the red curve corresponds to the blank substrate. (a) UV spectral range (200–400 nm), and (b) visible to near-infrared spectral range (400–1100 nm). The Y-axis denotes raw detector intensity in arbitrary units (a.u.).

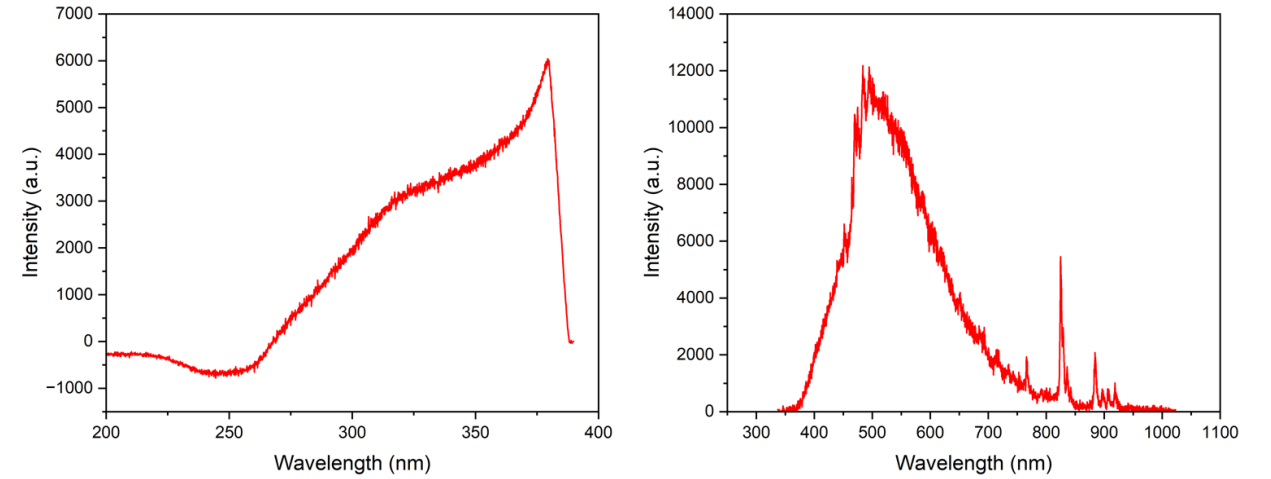

Figure 4.26: Difference spectra obtained by subtracting the blank substrate signal from the UCNPs-coated sample. The resulting curves represent the net luminescence generated by the upconversion nanoparticles under excitation. (a) Spectral difference in the UV region (200–400 nm), and (b) spectral difference in the visible to near-infrared region (400–1100 nm).

Regarding the absorption characteristics of the upconversion process, these were intended to be measured using the Flame spectrometer. However, due to its high sensitivity, the spectrometer saturates under strong light exposure, exceeding its dynamic range. To obtain a rough estimate of the

emission profile, the integration time was significantly reduced, allowing for a coarse spectral plot. While this adjustment made it possible to observe the general luminescence trend, it compromised the spectral resolution, preventing the detection of absorption valleys in the curve.

When using a photodetector to evaluate the upconversion efficiency, the measurement setup is shown in the Figure3.21, including a sample and an optical filter placed in front of the detector. To determine the luminescence intensity, measurements were conducted for both a blank sample and a UCNPs-coated sample. After the signal stabilized, steady-state intensities were recorded. The resulting Chart4.2 presents emission intensities at 360nm and 475nm.

	UCNPs Sample	Blank Sample	Δ
360nm	0.028mW	0.020mW	0.008mW
475nm	0.093mW	0.048mW	0.045mW

Table 4.2: Measured Emission Intensity of s-Coated and Blank Samples at 360nm and 475nm.

The sample containing nanoparticles exhibits a significantly higher photon intensity compared to the blank, indicating effective upconversion. The Δ value, representing the intensity difference between the coated and blank samples, confirms this enhancement. According to previous studies, upconversion emission at 475nm is typically stronger than at 360nm, and the measured delta values are consistent with this established behavior.

4.3.3 Integrating different parts of the system

In the previous sections, the performance of the Fabry–Perot filter and the upconversion behavior of the UCNPs were evaluated separately. Here, both components are integrated to assess the overall performance of the light emitter. Figure4.27 presents three samples: (a) the standalone Fabry–Perot filter, (b) the filter drop-cast with 5mg of UCNPs, and (c) the filter drop-cast with 10mg of UCNPs. Examination of the sample morphology reveals that it is challenging to achieve consistent coating quality. For instance, in the 10mg drop-cast sample, a large number of particles are concentrated near the substrate edge rather than the center. This is attributed to the non-uniform evaporation rate across the droplet surface: the larger curvature at the edge leads to faster evaporation, which induces an outward capillary flow from the center toward the edge. Suspended particles are carried along this flow, resulting in a higher concentration at the periphery.

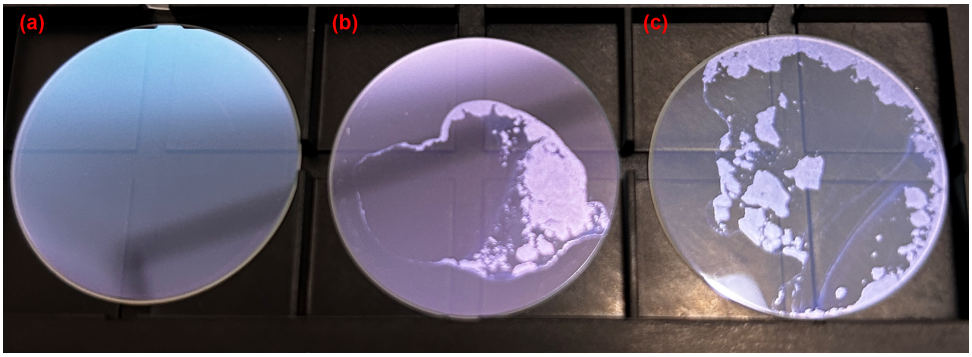

Figure 4.27: Photographs of (a) Fabry–Perot filter (FP), (b) FP drop-cast with 5 mg UCNPs, and (c) FP drop-cast with 10 mg UCNPs.

In the earlier measurements(Section 4.3.2), the upconversion intensity was recorded using a xenon light source. However, due to the broadband spectrum of the xenon lamp, the excitation light intensity could not be precisely quantified, making it impossible to calculate the energy conversion efficiency. To address this limitation, the setup was replaced with a laser diode system, enabling accurate measurement of the excitation intensity and, consequently, the upconversion light output. First, the photodetector was directly connected to the laser diode to measure the initial excitation intensity. As shown in Figure4.28, the measured output power was 0.5 W, which meets the operating requirements of the laser diode and ensures stable performance during subsequent experiments.

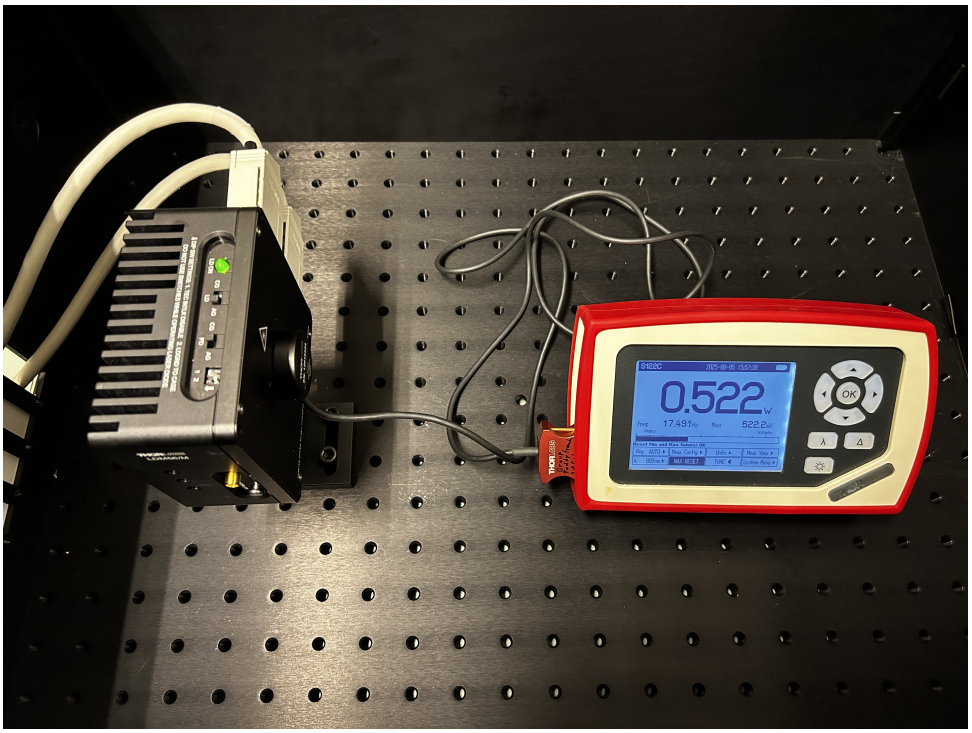

Figure 4.28: Intensity of laser diode.

After collimating the beam, the remaining 808nm photon power was measured. A blank Fabry–Perot (FP) filter and an FP filter coated with nanoparticles were then placed in the beam path to compare the transmitted intensity. The measured power after collimation was 0.44W. Subsequent measurements with the two samples showed no significant difference in transmitted power.

To enhance upconversion excitation, the positions of the focusing lens and the sample were swapped, enabling the laser to be more tightly focused onto the sample. Although focusing reduced the bandpass filter's spectral blocking performance, this configuration was necessary to meet the critical excitation threshold of the UCNPs.

Under focused excitation, Chart4.3 shows the measured intensities for different samples at 808nm. The blank FP filter data indicate that the reduced spectral selectivity of the bandpass filter increased the background noise.

	Pure Fabry-Perot Filter	5mg UCNPs coated on the Fabry-Perot Filter	10mg UCNPs coated on the Fabry-Perot Filter
360nm	$8.1\mu W$	$10.80\mu W$	$10.76\mu W$
475nm	$0.57\mu W$	$0.62\mu W$	$0.74\mu W$

Table 4.3: Measured emission intensity of integrated light emitter at 360nm and 475nm.

At 360nm, the measured powers were $2.70\mu W$ for the 5mg UCNPs-coated sample and $2.66\mu W$ for the 10mg sample, confirming the occurrence of upconversion. The slightly lower UV emission from the 10mg sample, despite its higher loading, can be attributed to the particle distribution: as shown in Figure4.27, the higher concentration caused particles to accumulate predominantly at the substrate edges, reducing the effective illuminated area.

At 475nm, the measured powers were $0.05\mu W$ (5mg) and $0.17\mu W$ (10mg), demonstrating that the integrated light emitter system effectively suppressed blue light transmission through the Fabry-Perot filter.

Based on the measured data, the energy conversion efficiency (ECE) can be calculated. Since the upconversion emission is isotropically distributed, only approximately half of the emitted photons can be detected by the photodetector in this setup. Therefore, to obtain a more accurate estimation of the efficiency, the calculated value should be multiplied by a factor of 2. For the sample with 5 mg of nanoparticles, the ECE is:

$$ECE_{5mg} = 2 \times \frac{2.7\mu W}{0.463W} \times 100\% = 0.0012\% \tag{4.2}$$

For the sample with 10 mg of nanoparticles, the ECE is:

$$ECE_{10mg} = 2 \times \frac{2.66\mu W}{0.463W} \times 100\% = 0.0011\% \tag{4.3}$$

Based on the excitation power and the light spot area, the power of the 808nm photons used for excitation is 0.463W. With the focused light spot covering an approximate area of 0.785cm², the excitation intensity can thus be calculated as:

$$I = \frac{P}{A} = 0.59W/cm^2 \tag{4.4}$$

As mentioned earlier, the UCNPs supplier recommends using at least a 0.5W laser for effective excitation. The calculated unit intensity of 0.59W/cm² confirms that this setup meets the excitation threshold.

Chapter 5

Discussion

In Section 2.6, three key challenges were identified based on both the state-of-the-art and the specific design requirements of this project: (i) selecting upconversion materials with high ultraviolet emission efficiency, (ii) determining an excitation light intensity sufficient to activate the UCNPs without causing damage to skin or underlying tissue, and (iii) ensuring that the optical filter can effectively block unwanted photons while allowing target photons to pass freely. The present study addressed these issues through the design, fabrication, and characterization of a light emitter, yielding promising results. Nevertheless, several limitations remain, which warrant further investigation and define potential directions for future development of the emitter.

5.1 Upconverting nanoparticles

In previous experiments with UCNPs, several key issues have been identified that negatively affect sample quality. The most prominent challenge is the weak adhesion between nanoparticles. Due to the fabrication method used by the supplier—where the original oleic acid (OA) ligands were only removed without any subsequent surface modification—the particles exhibit poor dispersibility and limited stability in aqueous solutions. Even after prolonged ultrasonication, the nanoparticles remain suspended for only a short duration. Moreover, during sample preparation, the weak adhesion results in sparse and uneven distribution when applying spin coating, making it difficult to achieve a dense and uniform film.

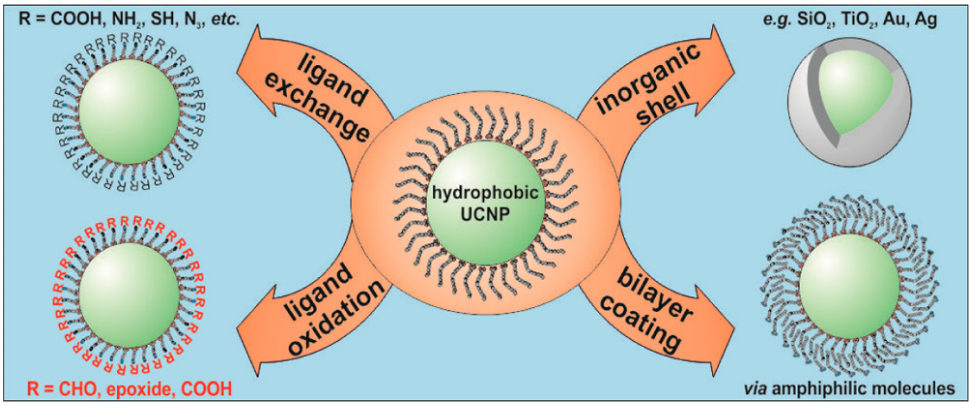

Figure 5.1: Four different methods to convert the Hydrophobic to Hydrophilic Surfaces. [46]

To address the hydrophobic nature of UCNPs and improve their adhesion, several surface modification strategies have been explored[46], as illustrated in the Figure5.1. These strategies aim to

enhance the hydrophilicity of the particles and include the following four approaches:

1. Modification of the Original Ligand: The OA ligands are chemically modified without removal, typically via oxidation, introducing hydrophilic functional groups such as carboxyl or epoxy groups to improve water compatibility.

2. Bilayer Coating with Amphiphilic Molecules: Amphiphilic molecules or polymers with hydrophobic tails and hydrophilic heads are used to wrap around the OA-coated nanoparticles, forming a bilayer or polymer shell that improves aqueous dispersion.

3. Hydrophilic Shell Coating: A hydrophilic inorganic or polymeric shell is directly coated onto the nanoparticle surface. This not only improves hydrophilicity but also provides a protective inert layer to reduce surface quenching effects.

4. Ligand Exchange with Hydrophilic Molecules: The original OA ligands are completely removed and replaced with new hydrophilic ligands such as PEG, carboxylic acids, or phosphates, enhancing water solubility and colloidal stability.

Apart from adhesion, another key limiting factor is the low upconversion efficiency. According to the results, under 808nm laser excitation at 0.5W, the energy conversion efficiency is only 0.001%. Enhancing this efficiency could be approached from two perspectives: deposition method and excitation source. Regarding the deposition method, the present study employed drop-casting, which was sufficient to confirm the occurrence of upconversion but yielded only weak emission. This is attributable not only to the inherently low conversion efficiency but also to the possibility that multilayer particle stacking prevents some nanoparticles from being effectively excited by 808nm photons. Spin coating, which can produce a uniform, non-aggregated surface, could further improve efficiency. Combined with the previously discussed adhesion enhancement strategies, resolving the adhesion issue in future experiments would enable the use of spin coating to form a uniform thin film for more efficient NIR photon absorption.

5.2 Intensity of light

From the perspective of excitation intensity, the current setup required an optical power density of approximately 0.5W/cm² to observe measurable upconversion. Further increasing the excitation intensity could significantly enhance the conversion efficiency. However, although a high-power continuous light source can generate strong UV emission via upconversion, it also poses potential safety risks to human skin and underlying tissues. A promising alternative is to employ pulsed excitation, which delivers energy at controlled intervals. This strategy can sustain adequate upconversion output while reducing the risk of thermal and phototoxic damage to biological tissues. Consequently, optimizing the parameters of pulsed excitation represents an important direction for future work.

5.3 Fabry-Perot Filter

Regarding the simulation and fabrication of the Fabry–Perot filter, the results demonstrate that at a deposition temperature of 350°C, ICPCVD can effectively produce a filter with a transmission rate of 96.67% at 360nm and a rejection rate of 77.46% at 475nm. Furthermore, after integrating the UCNPs with the filter, laser excitation of the 5mg UCNPs sample resulted in only 0.05μW of 475nm photons being transmitted, corresponding to approximately 1/50 of the transmitted power at 360nm. This clearly highlights the filter's ability to suppress unwanted blue emission while allowing efficient

UV transmission. Nevertheless, several aspects of the filter's design and performance warrant further discussion and define directions for future research.

In the discussion of NADH absorption spectrum, Fabry–Perot filter design, and subsequent UCNPs selection and optical characterization, a spectral mismatch in the UV region was observed. Although the absorption peak of NADH is centered around 340nm, the emission peak of the selected UCNPs appears closer to 360nm, which introduces a certain degree of spectral deviation. However, neither NADH absorption nor UCNPs emission is characterized by a sharp, narrow peak; instead, both exhibit relatively broad spectral profiles. As shown in the Figure2.2, NADH exhibits a broad absorption band from 300 to 400nm, while the vendor-supplied spectrum of UCNPs indicates UV emission covering approximately 320–380nm(Figure3.6). Furthermore, based on result shown in Figure4.26, the actual emission range of the UCNPs extends from 250 to 380nm, fully encompassing the NADH absorption region. Taken together, the UCNPs-emitted photons are well aligned with NADH excitation requirements. Therefore, in the Fabry–Perot filter design, it is essential to ensure high transmittance within the NADH absorption range, while simultaneously achieving minimal transmittance in the blue region to suppress unwanted background.

In the experimental optimization of the Fabry–Perot filter, my focus was placed on adjusting the ICPCVD deposition recipe and addressing spectral shifting due to fabrication errors. However, the influence of incident light angle on filter performance was not investigated. In practical applications, the incident angle can vary due to several factors, which may further impact the transmission characteristics and overall system efficiency. This effect should be considered in future iterations of the filter design.

In addition, analysis of the fabricated filter indicates that the transmittance at 475nm remains around 20%, which deviates from the ideal performance of 4.9% predicted by simulation. Although initial measurements with the laser diode demonstrated that the transmitted blue light is significantly weaker than the UV component, its presence may still affect subsequent detection. If the upconversion efficiency is improved in future designs, the absolute intensity of blue emission will inevitably increase. This residual blue light leakage warrants further investigation due to its potential impact on detection accuracy. In practical scenarios, a portion of the 475nm light passing through the filter could be reflected from the heart surface and ultimately reach the photodetector. Therefore, it is essential to estimate the number of 475nm photons reaching the detector and to quantify their contribution to the measured signal. Such an assessment will determine whether the remaining blue light introduces significant interference and whether additional filter optimization is required to further suppress this residual transmission.

5.4 Optical characterization

5.4.1 Xenon light source

When using the xenon lamp as the excitation source, several limitations were encountered in the optical characterization of UCNPs. As shown in Figure4.25, the emission spectra were recorded by two spectrometers in the 200–400nm and 400–1100nm ranges, respectively. These spectra could not be combined into a single plot due to the different sensitivities and integration times of the instruments: the Maya Pro 2000 has lower sensitivity and allows a 100 ms integration time, whereas the Flame spectrometer is highly sensitive and requires a shorter 1 ms integration time to avoid saturation. This discrepancy prevents direct comparison or merging of the two spectra. In contrast, for Fabry–Perot filter transmission measurements, both spectrometers could be referenced to the same 100% transmittance baseline, enabling direct splicing of the curves.

Photodetector-based measurements with the xenon lamp also suffer from the absence of a monochromator and integrating sphere, which introduces substantial inaccuracies. Variations in the distance and alignment between the light source and detector during measurements lead to inconsistent results. As a result, the recorded intensities cannot represent the absolute upconverted luminescence, as they include background contributions from the broadband xenon lamp. Only the delta value—defined as the difference between the blank and UCNPs-coated samples—can be used to estimate the relative upconversion effect. Furthermore, the actual excitation power at 808nm cannot be quantified, making it impossible to determine whether the UCNPs are fully excited.

One possible improvement, applicable even within the xenon lamp setup, is the integration of an optical attenuator to precisely modulate the excitation intensity. This would allow investigation of the saturation behavior of the UCNPs; once the upconversion process reaches its absorption limit, further increases in excitation power would no longer enhance emission, thereby providing a reliable measure of the maximum performance of the light emitter.

5.4.2 Laser Diode

Although the laser diode setup enables calculation of both the energy conversion efficiency (ECE) and the energy intensity, several improvements are still required, which also indicate directions for future work. In the current configuration, UCNP excitation is achieved exclusively via a focused laser beam to ensure sufficient excitation intensity. However, due to the inherent characteristics of the bandpass filter, optimal rejection performance is achieved only when light is incident perpendicular to its surface. The use of a focused beam introduces angular deviations that can compromise the filter's blocking performance. Future work should therefore investigate the excitation threshold of UCNPs, specifically determining the minimum optical power density required to initiate measurable upconversion. If this threshold is already met under collimated illumination, the priority should shift to optimizing sample preparation to boost emission efficiency. For example, increase the UCNPs loading while ensuring intimate contact with the excitation beam; note that excessive multilayer stacking, although it raises particle quantity, can hinder photon absorption. Conversely, if collimated excitation is insufficient, higher-power laser diodes should be employed to achieve the necessary excitation intensity.

Chapter 6

Conclusion

This project aims to develop an implantable sensor for real-time monitoring of cardiac oxygenation in heart failure patients. The system leverages the luminescent properties of NADH, utilizing a light emitter that converts externally delivered near-infrared (NIR) photons into ultraviolet (UV) photons through upconverting nanoparticles (UCNPs), thereby enabling NADH excitation. To address the spectral overlap issue, where the UCNPs emit both UV and blue light, a Fabry–Perot filter was integrated into the system to suppress the blue component that could interfere with measurement accuracy. COMSOL simulations were conducted to optimize the filter's multilayer thickness configuration, and the impact of precursor gas ratios on deposition defects and filter performance was systematically investigated. The optimized UCNPs were then drop-cast onto the filter surface, and morphological features were analyzed using various material characterization techniques. An optical platform was constructed to evaluate the upconversion performance. Due to the high excitation energy threshold of UCNPs, the xenon-lamp-based setup, although capable of isolating 808nm photons, exhibited insufficient optical intensity. To overcome this limitation, the monochromator and integrating sphere were removed, allowing direct exposure of the sample to the light source. Subsequently, a dedicated optical system employing an 808nm laser diode was developed to achieve stable excitation and accurately quantify the upconversion efficiency. Overall, under 808nm excitation, a clear upconversion luminescence was observed. The Fabry–Perot filter effectively suppressed blue light while maintaining high transmittance in the UV region. These results confirm the feasibility of the proposed light emitter system for implantable cardiac oxygen monitoring. Importantly, this light emitter successfully eliminates the need for implantable batteries, enabling detection through external illumination. While the system still faces challenges such as low upconversion efficiency and lack of biodegradability, these limitations provide clear directions for future research and optimization.

References

[1] Véronique L Roger. "Epidemiology of heart failure". In: *Circulation research* 113.6 (2013), pp. 646–659.

[2] Daniel Burkhoff et al. "Reverse remodeling with left ventricular assist devices". In: *Circulation research* 128.10 (2021), pp. 1594–1612.

[3] Emma J Birks et al. "Prospective multicenter study of myocardial recovery using left ventricular assist devices (RESTAGE-HF [remission from stage D heart failure]) medium-term and primary end point results". In: *Circulation* 142.21 (2020), pp. 2016–2028.

[4] Anthony Saxton, Muhammad Ali Tariq, and Bruno Bordoni. "Anatomy, thorax, cardiac muscle". In: *StatPearls [Internet]*. StatPearls Publishing, 2023.

[5] Mahmoud Abdellatif, Simon Sedej, and Guido Kroemer. "NAD+ metabolism in cardiac health, aging, and disease". In: *Circulation* 144.22 (2021), pp. 1795–1817.

[6] Kristina R Rivera et al. "Measuring and regulating oxygen levels in microphysiological systems: Design, material, and sensor considerations". In: *Analyst* 144.10 (2019), pp. 3190–3215.

[7] WRITING COMMITTEE MEMBERS et al. "Heart failure epidemiology and outcomes statistics: a report of the Heart Failure Society of America". In: *Journal of cardiac failure* 29.10 (2023), p. 1412.

[8] Cleveland Clinic. *Heart Failure: Understanding Heart Failure*. Accessed: 2025-07-16. 2024. URL: https://my.clevelandclinic.org/health/diseases/17069-heart-failure-understanding-heart-failure.

[9] American Heart Association. *Causes and Risks for Heart Failure*. Accessed: 2025-07-16. 2024. URL: https://www.heart.org/en/health-topics/heart-failure/causes-and-risks-for-heart-failure.

[10] Theresa A McDonagh et al. "2023 focused update of the 2021 ESC guidelines for the diagnosis and treatment of acute and chronic heart failure: developed by the task force for the diagnosis and treatment of acute and chronic heart failure of the European Society of Cardiology (ESC) with the special contribution of the Heart Failure Association (HFA) of the ESC". In: *European heart journal* 44.37 (2023), pp. 3627–3639.

[11] Alba Luengo et al. "Increased demand for NAD+ relative to ATP drives aerobic glycolysis". In: *Molecular cell* 81.4 (2021), pp. 691–707.

[12] Chi Fung Lee et al. "Normalization of NAD+ redox balance as a therapy for heart failure". In: *Circulation* 134.12 (2016), pp. 883–894.

[13] Anuj Dalal et al. "Luminous lanthanide diketonates: Review on synthesis and optoelectronic characterizations". In: *Inorganica Chimica Acta* 550 (2023), p. 121406.

[14] Simin Cao et al. "Femtosecond fluorescence spectra of NADH in solution: ultrafast solvation dynamics". In: *The Journal of Physical Chemistry B* 124.5 (2020), pp. 771–776.

[15] Jianghui Guo et al. “Non-invasive optical monitoring of human lungs: Monte Carlo modeling of photon migration in Visible Chinese Human and an experimental test on a human”. In: *Biomedical Optics Express* 13.12 (2022), pp. 6389–6403.

[16] JB Dawson et al. “A theoretical and experimental study of light absorption and scattering by in vivo skin”. In: *Physics in Medicine & Biology* 25.4 (1980), p. 695.

[17] José Lifante et al. “The role of tissue fluorescence in in vivo optical bioimaging”. In: *Journal of Applied Physics* 128.17 (2020).

[18] Lingyan Shi et al. “Transmission in near-infrared optical windows for deep brain imaging”. In: *Journal of biophotonics* 9.1-2 (2016), pp. 38–43.

[19] Inês S Martins et al. “Measurement of tissue optical properties in a wide spectral range: a review”. In: *Biomedical Optics Express* 14.1 (2022), pp. 249–298.

[20] Baptiste Jayet. “Acousto-optic and photoacoustic imaging of scattering media using wavefront adaptive holography techniques in NdYO4”. PhD thesis. Université Pierre et Marie Curie-Paris VI, 2015.

[21] Caerwyn Ash et al. “Effect of wavelength and beam width on penetration in light-tissue interaction using computational methods”. In: *Lasers in medical science* 32.8 (2017), pp. 1909–1918.

[22] C Rebecca Simpson et al. “Near-infrared optical properties of ex vivo human skin and subcutaneous tissues measured using the Monte Carlo inversion technique”. In: *Physics in Medicine & Biology* 43.9 (1998), p. 2465.

[23] Alexey N Bashkatov et al. “Optical properties of human cranial bone in the spectral range from 800 to 2000 nm”. In: *Saratov Fall Meeting 2005: Optical Technologies in Biophysics and Medicine VII*. Vol. 6163. SPIE. 2006, pp. 306–316.

[24] JE Moffatt et al. “A practical review of shorter than excitation wavelength light emission processes”. In: *Applied Spectroscopy Reviews* 55.4 (2020), pp. 327–349.

[25] Hanna C McGregor et al. “Clinical utility of Raman spectroscopy: current applications and ongoing developments”. In: *Advanced Health Care Technologies* (2016), pp. 13–29.

[26] Leipeng Li et al. “Pr3+-Based Visible-to-Ultraviolet Upconversion. A minireview”. In: *Advanced Physics Research* 4.2 (2025), p. 2400097.

[27] Feng Wang and Xiaogang Liu. “Recent advances in the chemistry of lanthanide-doped upconversion nanocrystals”. In: *Chemical Society Reviews* 38.4 (2009), pp. 976–989.

[28] Xian Chen et al. “Photon upconversion in core–shell nanoparticles”. In: *Chemical Society Reviews* 44.6 (2015), pp. 1318–1330.

[29] Han-Lin Wei et al. “Tuning Near-Infrared-to-Ultraviolet Upconversion in Lanthanide-Doped Nanoparticles for Biomedical Applications”. In: *Advanced Optical Materials* 11.11 (2023), p. 2201716.

[30] Palak Jethva et al. “Lanthanide-doped upconversion luminescent nanoparticles—Evolving role in bioimaging, biosensing, and drug delivery”. In: *Materials* 15.7 (2022), p. 2374.

[31] Sara Pimenta et al. “High-selectivity neural probe based on a Fabry–Perot optical filter and a CMOS silicon photodiodes array at visible wavelengths”. In: *Journal of Biomedical Optics* 23.10 (2018), pp. 105004–105004.

[32] Ton Koonen. “Fabry-Perot interferometer filters”. In: *Wavelength filters in fibre optics*. Springer, 2006, pp. 271–287.

[33] Sanyang Han et al. “Enhancing luminescence in lanthanide-doped upconversion nanoparticles”. In: *Angewandte Chemie International Edition* 53.44 (2014), pp. 11702–11715.

[34] Omid Veiseh and Arturo J Vegas. “Domesticating the foreign body response: Recent advances and applications”. In: *Advanced drug delivery reviews* 144 (2019), pp. 148–161.

[35] James M Anderson, Analiz Rodriguez, and David T Chang. “Foreign body reaction to biomaterials”. In: *Seminars in immunology*. Vol. 20. 2. Elsevier. 2008, pp. 86–100.

[36] Pengfei Peng et al. “Biodegradable inorganic upconversion nanocrystals for in vivo applications”. In: *ACS nano* 14.12 (2020), pp. 16672–16680.

[37] Muthu Kumara Gnanasammandhan Jayakumar, Niagara Muhammad Idris, and Yong Zhang. “Remote activation of biomolecules in deep tissues using near-infrared-to-UV upconversion nanotransducers”. In: *Proceedings of the National Academy of Sciences* 109.22 (2012), pp. 8483–8488.

[38] Hao Wan et al. “A bright organic NIR-II nanofluorophore for three-dimensional imaging into biological tissues”. In: *Nature communications* 9.1 (2018), p. 1171.

[39] Tianying Sun et al. “Integrating temporal and spatial control of electronic transitions for bright multiphoton upconversion”. In: *Nature communications* 10.1 (2019), p. 1811.

[40] Ralph Weissleder. “A clearer vision for in vivo imaging”. In: *Nature biotechnology* 19.4 (2001), pp. 316–317.

[41] Qiuqiang Zhan et al. “Using 915 nm laser excited Tm3+/Er3+/Ho3+-doped NaYbF4 upconversion nanoparticles for in vitro and deeper in vivo bioimaging without overheating irradiation”. In: *ACS nano* 5.5 (2011), pp. 3744–3757.

[42] Ye-Fu Wang et al. “Nd3+-sensitized upconversion nanophosphors: efficient in vivo bioimaging probes with minimized heating effect”. In: *ACS nano* 7.8 (2013), pp. 7200–7206.

[43] Markus Haase and Helmut Schäfer. “Upconverting nanoparticles”. In: *Angewandte Chemie International Edition* 50.26 (2011), pp. 5808–5829.

[44] DiagNano™. *Water-Dispersible Upconverting Nanoparticles (Absorbance Max 808 nm, Core-Shell, 365 nm/475 nm)*. Accessed: July 20, 2025. 2025. URL: https://www.cd-bioparticles.com/product/diagnano-water-dispersible-upconverting-nanoparticles-absorbance-max-808-nm-core-shell-365-nm-475-nm-item-dnl-c073-14325.html.

[45] Zhengquan Li, Yong Zhang, and Shan Jiang. “Multicolor core/shell-structured upconversion fluorescent nanoparticles”. In: *Advanced Materials* 20.24 (2008), pp. 4765–4769.

[46] Verena Muhr et al. “Upconversion nanoparticles: from hydrophobic to hydrophilic surfaces”. In: *Accounts of chemical research* 47.12 (2014), pp. 3481–3493.

[47] Reinoud F Wolffenbuttel et al. “Optical properties of nitride-rich SiNx and its use in CMOS-compatible near-UV Bragg filter fabrication”. In: *Optical Materials: X* 24 (2024), p. 100348.

[48] Ocean Insight. *Deuterium Tungsten Halogen Light Sources*. https://www.oceanoptics.com/accessories/light-sources/uv-vis-nir-light-sources/deuterium-tungsten-halogen-light-sources/. Accessed: 2025-07-25. n.d.

Appendix A

Optical coefficients of different tissues

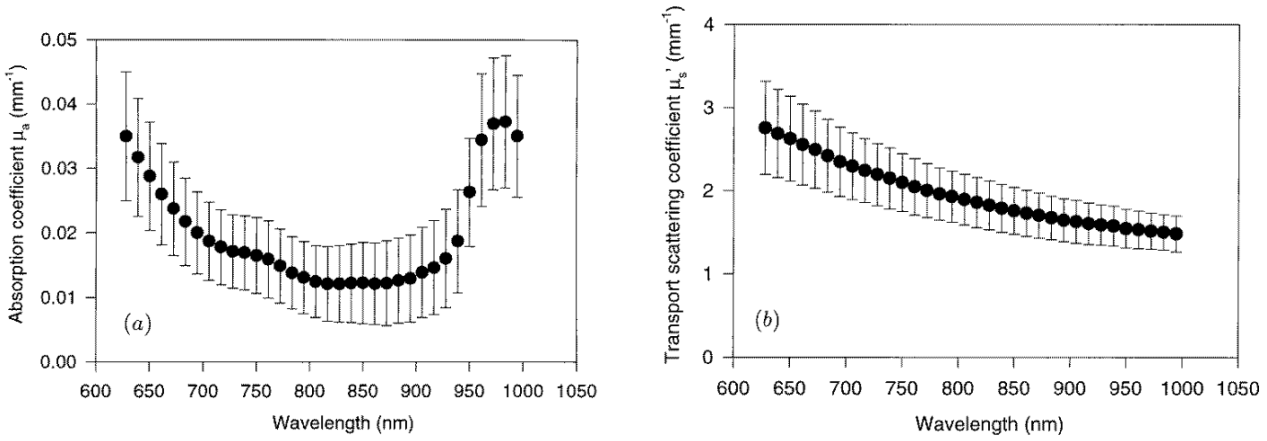

Figure A.1: Optical coefficients of human caucasian dermis: (a) absorption coefficient and (b) transport scattering coefficient.

[22]

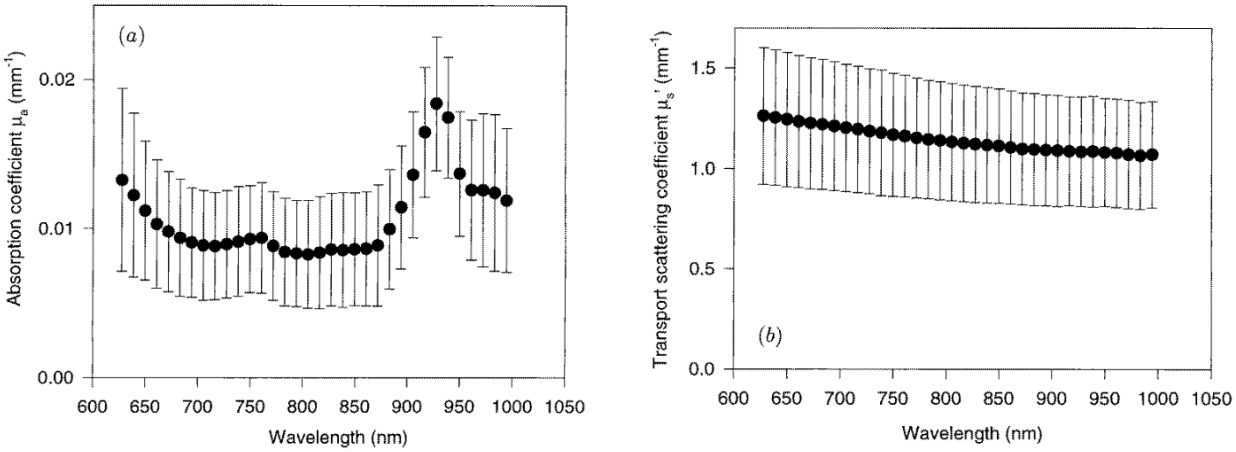

Figure A.2: Optical coefficients of human caucasian subdermis: (a) absorption coefficient and (b) transport scattering coefficient.

[22]

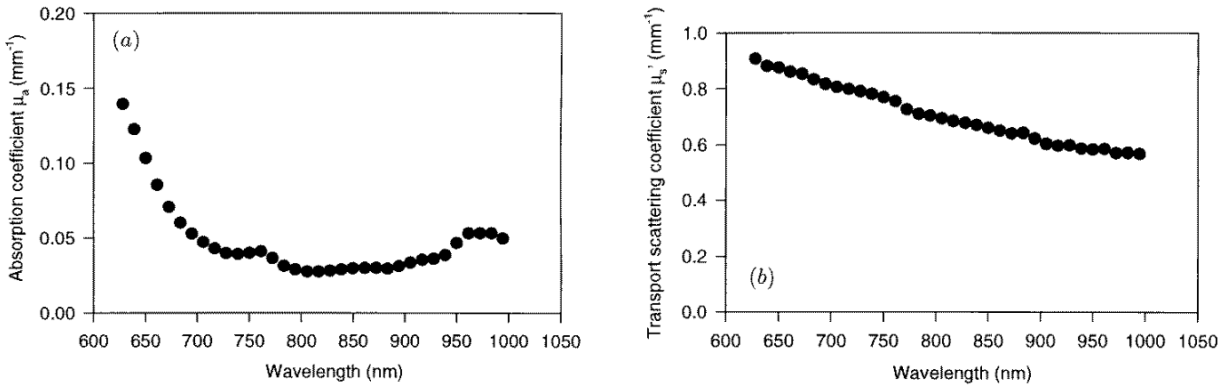

Figure A.3: Optical coefficients of human abdominal muscle (a) absorption coefficient and (b) transport scattering coefficient.

[22]

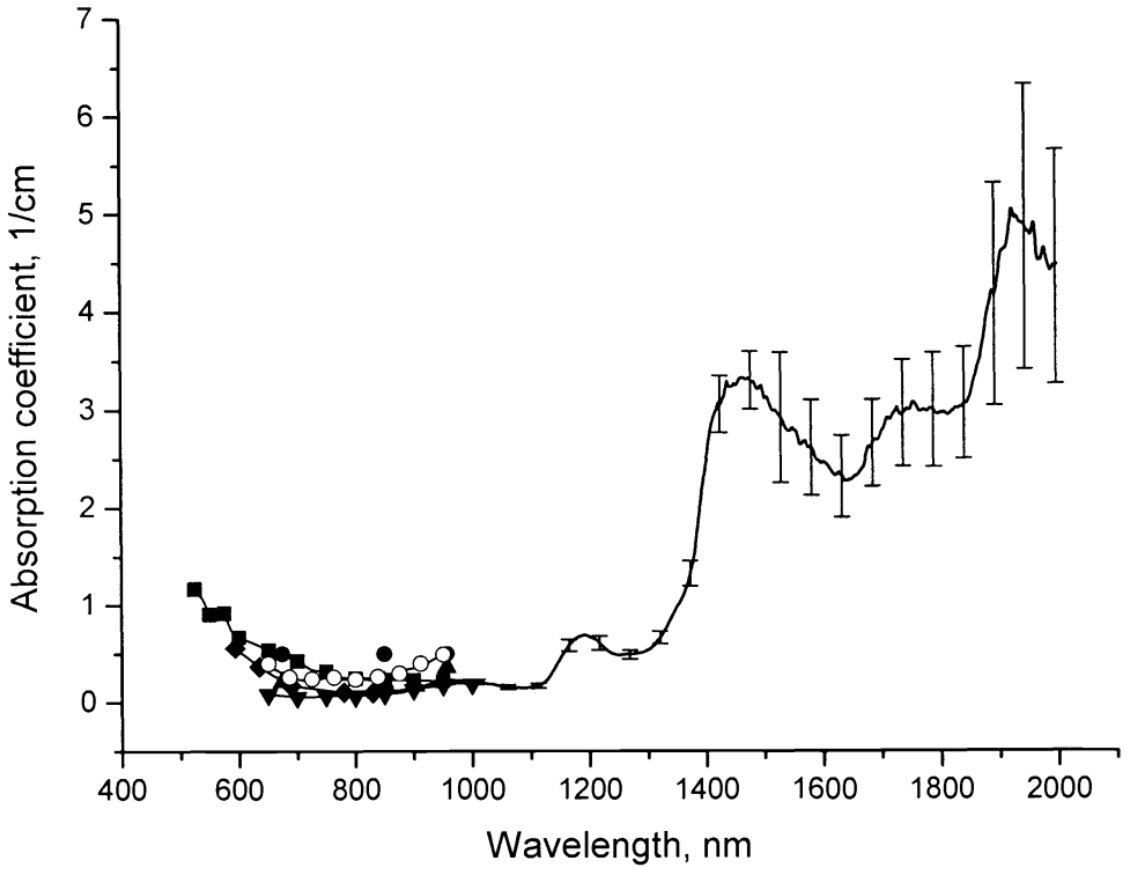

Figure A.4: The wavelength dependence of the absorption coefficient of human cranial bone in vitro.

[23]

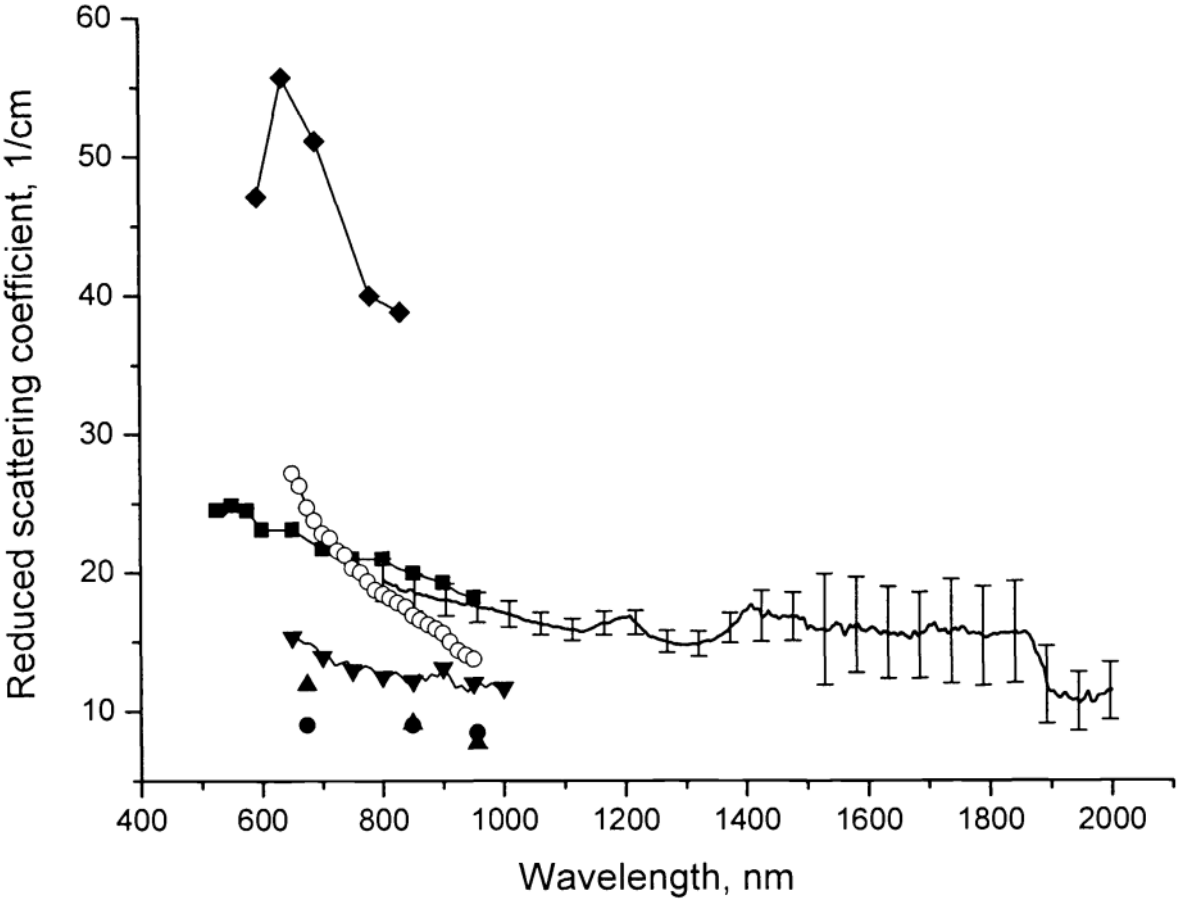

Figure A.5: The spectral dependence of reduced scattering coefficient of human cranial bone in vitro. [23]

Appendix B

Fabry-Perot Simulation by Comsol

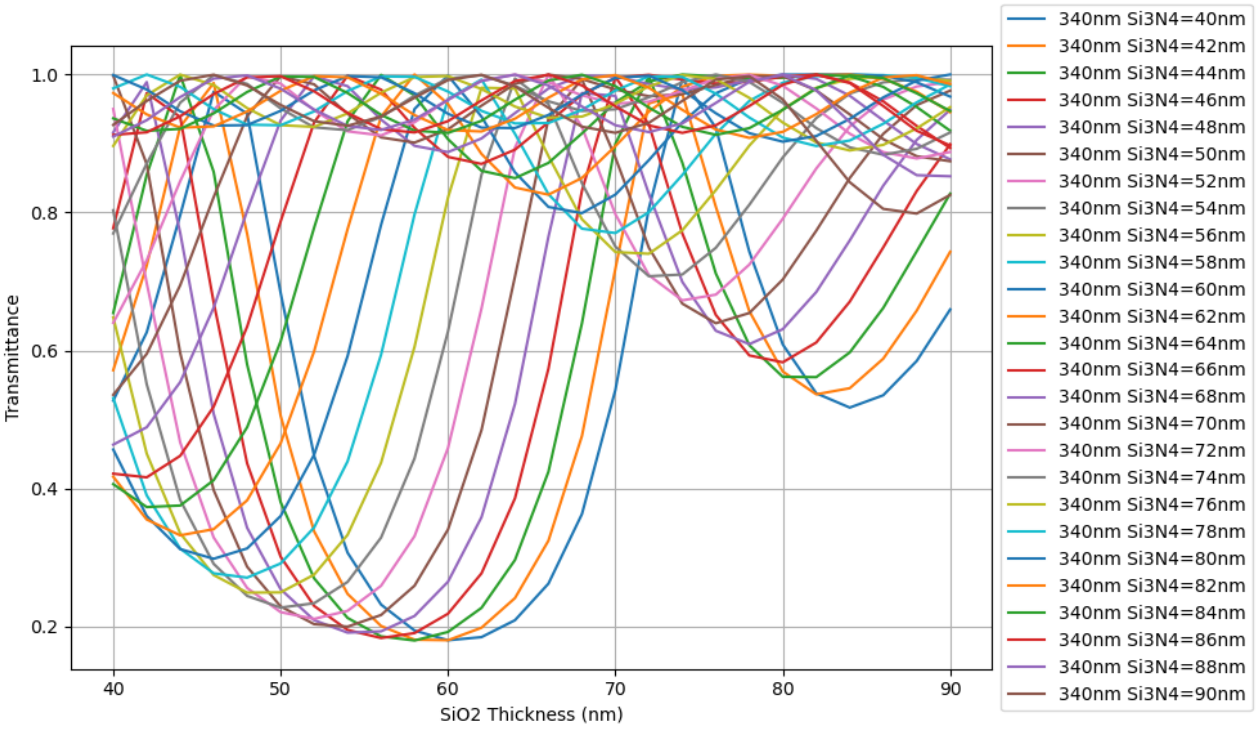

Figure B.1: The transmission curve under 360nm of different combinations.

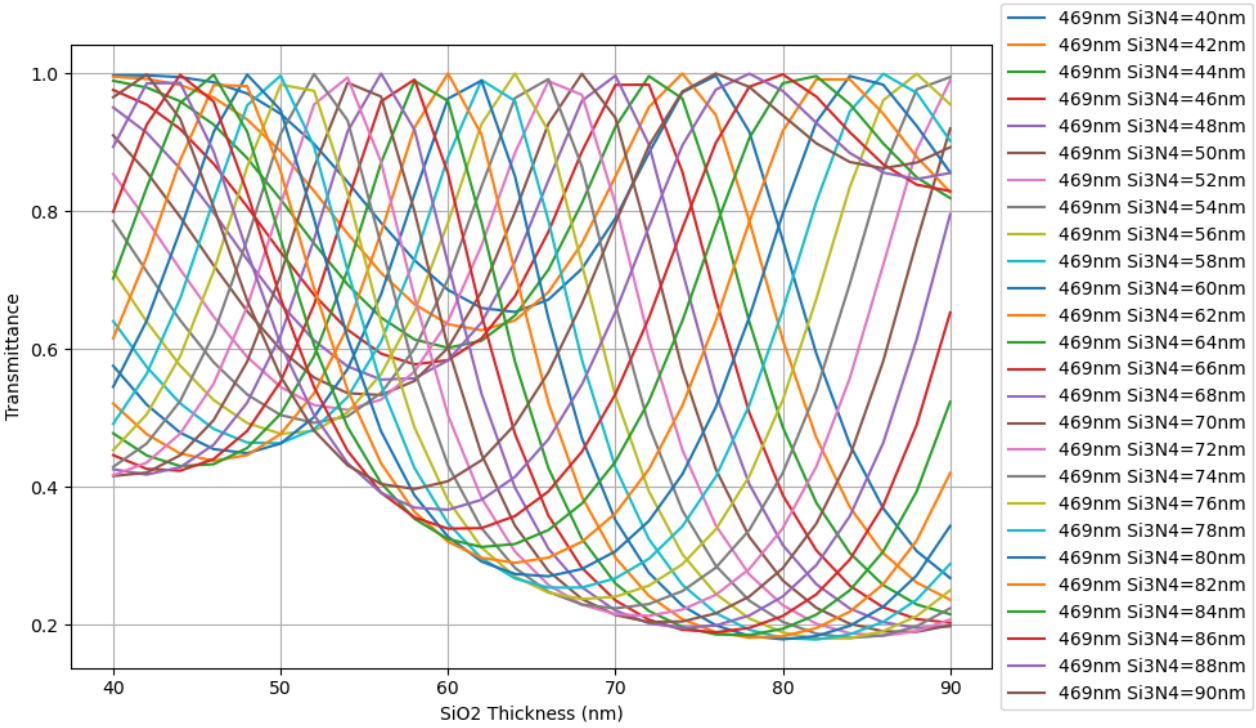

Figure B.2: The transmission curve under 469nm of different combinations.

Appendix C

Curve shifting of the Fabry-Perot Filter

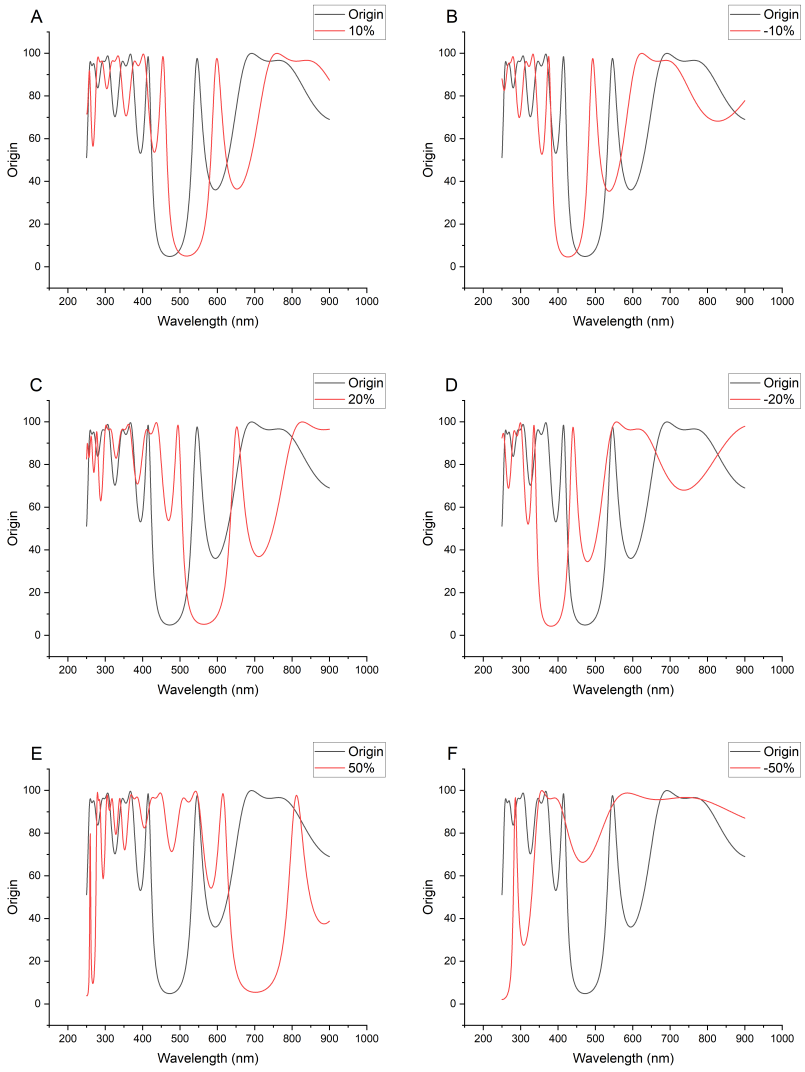

Figure C.1: The shifting curve under the structure change of ±10%, ±20%, and ±50%.